Origin, location and transport of excess electrons in titanium dioxide

Jingfeng Li

THÈSE DE DOCTORAT
DE L'UNIVERSITÉ PIEERE ET MAIRE CURIE

Spécialité : Physique
Ecole Doctorale Physique et Chimie des Matériaux

réalisée
L'Institut des NanoSciences de Paris

Presentée par
Jingfeng LI

pour obtenir le grade de :
DOCTEUR DE L'UNIVERSITÉ PIERRE ET MARIE CURIE

Sujet de la thèse :

Origin, location and transport of excess electrons in titanium dioxide

Soutenue le 20 Octobre 2016:

devant le jury composé de:

Paul Dumas	Directeur de Recherche (SOLEIL)	Rapporteur
Jean-Marc Layet	Professeur (PIIM, Marseille)	Rapporteur
Abhay Shukla	Professeur (IMPMC, Paris)	Examinateur
Geoff Thornton	Professeur (UCL, Londres)	Examinateur
Jacques Jupille	Directeur de Recherche (INSP, Paris)	Directeur de thèse
Rémi Lazzari	Chargé de Recherche	Co-directeur de thèse(Invité)

October 27, 2016

CONTENTS

Contents

CHAPTER 1

INTRODUCTION

Titanium dioxide (TiO_2) is attracting an increasing scientific interest both for its existing or potential applications. To cite a few, it is already used in self-cleaning coatings and dye-sensitized solar cells and it offers promising solutions to water/air purification and hydrogen production through water splitting thanks to its (photon)catalytic properties [1,2]. Titanium dioxide is foreseen to play a key role in environmental issues and alternative energy sources. The number of hints in the Web of Science database (> 150.000) with the keyword TiO_2 demonstrates the incredible interest aroused by this material.

Since the stoichiometric oxide is chemically inactive, applications mostly rely on reduced forms TiO_{2-x} of the oxide which points to properties of defects through which stoichiometry changes occur. Reduction formally transforms Ti^{4+} in Ti^{3+} which goes with the formation of the most common defects, oxygen vacancies and titanium interstitials. The excess electrons that result from the process populate Ti 3d states that are observed by electron spectroscopies to be located at 0.8-1 eV below the Fermi level. These are commonly referred to as band gap state(s) (BGS). Excess charges are active in TiO_2-based (photo)chemistry and are at the origin of the n-type electron conductivity of the reduced oxide with a puzzling polymorh dependence.

Despite the strong research effort devoted to the topic, in particular through a "surface science" approach (see reviews [1–9]), the three following central questions are still pending or strongly debated: (i) the respective role of oxygen vacancies and titanium interstitials in the formation of band gap states; (ii) the position of the energy levels of the gap features which can be questioned in the extent in which the n-type conductivity of the oxide contradicts the deep donor character of the BGS; (iii) the nature of the electronic transport in the oxide. The present work will focus on those issues in the case of the model $TiO_2(110)$ rutile surface.

1.1 The origin of the bang gap states

Recent data support the ancient idea [10] that surface oxygen vacancies (O_b-vac) on $TiO_2(110)$ are at the origin of the BGS observed on the defective surface. On the basis of oxygen

chemisorption experiments on TiO_2 surfaces involving different types of defects, N. Petrik *et al.* [11] concluded that the surface activity of the oxide mostly stems from O_b-vac. C. M. Yim *et al.* [12] and X. Mao et al [13] have shown that the BGS intensity, as measured by ultraviolet photoemission spectroscopy (UPS), linearly correlates with O_b-vac density which leads those authors to conclude that O_b-vac are the dominant source of BGS.

Now, this view is challenged by different groups. Aside filling of the surface vacancy, extra-oxygen atoms (O_{ad}) adsorbed at five coordinated Ti (Ti_{5c}) sites result from reaction of molecular oxygen with the reduced TiO_2 surface. The counting of these O_{ad} atoms in Scanning Tunneling Microscopy (STM) images revealed that they are in excess with respect to what is expected by assuming O_b-vac as the only adsorption site [14–18]. It was inferred that bulk defects provide extra charges to stabilise these extra O_{ad}. Combining STM observations with UPS experiments and Density Functional Theory (DFT) calculations, S. Wendt and coworkers [14] proposed that BGS mostly come from Ti interstitials (Ti_{int}). Consequently, they assigned the excess O_{ad} to a non-O_b-vac-related dissociation channel on Ti_{5c} sites [16–18]. A. C. Papageorgiou *et al.* [15] proposed a different mechanism. With the support of a numerical simulation, they suggested that the charges needed to produce the excess O_{ad} were first transferred from bulk defects to the lattice, prior to being trapped by O_b-vac on which molecular oxygen could dissociate to give rise to O_{ad}.

Finally, all spectroscopic studies of BGS show that a residual fraction of these resists any healing process in standard surface science conditions. Indeed, the existence of this feature also contributes to the debate which opposes the supporters of O_b-vac origin and Ti_{int} origin. Regarding the former suggestion, Du *et al.* [19] argued that oxygen can dissociate on Ti_{5c} sites via partially delocalized charges from O_{vac} but that the delocalisation becomes less effective when the O_{ad} increases, thus leaving unreacted O_b-vac at the surface of the oxide. Conversely, if the dominant source of BGS is Ti_{int}, the residual BGS peak should be associated to deep Ti_{int}.

1.2 The location of the energy levels of the band gap states

Experimentally, the electronic levels of BGS are found as a feature at 0.8-1 eV below the Fermi level in photoemission [10, 12, 14, 20], electron energy loss [21], occupied density of states in scanning tunneling spectroscopy [15, 22], near-infrared optical absorption [23] and electron spin-resonance [24]. These values suggest that BGS behave as trapped deep donors which apparently conflicts with the n-type conductivity of reduced TiO_2 since activation ionization energies as low as a few tens of meV were derived by temperature-dependent transport measurements [25].

On the theoretical side, while standard DFT predicts a delocalized behaviour for excess electrons, more advanced simulations (DFT+U, hybrid functionals, etc.…) are able to re-

produce the experimental spectroscopic findings. But some authors attracted the attention on the problem of vertical transitions and thermodynamic transitions related to the polaron character of the defect states [22, 26, 27]. Indeed, the large static dielectric constant of TiO_2 favours local distorsions around charges leading to the formation of polarons. As probed by photoemission [28], instantaneous vertical transitions retain the starting state of the strained polaron geometry; defects appear as "deep donors" located at 0.8-1eV. Thermodynamic transition states involved in electron transport imply the relaxation of polarization, in which case the defects appear as much "shallower donors" that are close to conduction band as in classical semiconductors.

1.3 The nature and transport property of excess electrons

While there is a consensus on the spectroscopic fingerprints of the apparent deep trapped electrons, the nature of conductivity raises the unresolved question of the spatial extension of the polaronic distorsion. The small polaron follows an hopping conduction mechanism with an electronic mobility that increases with temperature. A larger polaron behaves more like a free-carrier but with an enhanced effective mass; its mobility decreases with temperature. The landscape of the existing literature on electronic transport in TiO_2 is far from being transparent even for single crystals; it seems that free carriers and polaronic configurations compete to account for conduction electrons. Theory faces the problems of electronic localisation, entropic or temperature effects and small of energy differences.

A free-like carrier behaviour was postulated by J.-F. Baumard and F. Gervais who have introduced a plasmon contribution to fit their infrared reflectivity data of reduced rutile TiO_{2-x} [29]. This contribution, absent in the case of the stoichiometric substrate, allowed the description of the energy shifts and screening effects that they observed in the optical phonon spectra. They found effective masses quite similar to those deduced from transport measurements [30, 31]. More recently, E. Hendry *et al.* [32] showed that, in the THz range, the dielectric function for photoexcited carriers follow a Drude behavior.

In their theoretical study, N. A. Deskins and M. Dupuis [33] reported that the conductivity may result from hopping of small polarons with an activation energy that, unfortunatly, is not able to explain the very large mobility coefficient and its temperature dependence [25]. Similar conclusion was reached by other groups [26, 27]. But *ab initio* molecular dynamics simulations of excess electrons produced by O_b-vac on $TiO_2(110)$ pinpointed an fast temporal averaging over polaronic configurations close in energy [22, 34]. More recently, it was suggested that excess electrons in anatase prefer the free carrier configuration and those of rutile the polaronic one with hopping [22].

In fact, some authors suggest that TiO_2 rutile lies typically in a regime of intermediate coupling in terms of polaron [25, 32]. Clearly, hoping from defect to defect sites dominates at low temperature [30]. However, above 250 K [25], transport properties are well explained by

donor centres completely exhausted with an activation energy of around 10 meV.

1.4 Outline

In this thesis, the above issues were systematically addressed by means of (High Resolution) Electron Energy Loss Spectroscopy -(HR)EELS- measurements and dielectric theory simulations. The outline is as follows.

After the present introduction, the experimental set-up and techniques used are introduced in Chap. 2. The structure and properties of the studied surface, *i.e.* $TiO_2(110)$-(1×1) are also recalled as well as the surface preparation methods.

In Chap. 3, dielectric simulations are used to predict and explain the different excitations found in (HR)EELS spectra. After a reminder of the dielectric theory of EELS and a discussion of key points used in data fitting (Chap. 5), a parametrization of the dielectric function of TiO_2 from far-infrared to ultraviolet is proposed from data of the literature. Afterwards, the interplay and screening between excitations that are either induced (BGS, plasmons) or perturbed (phonons) by the reduction of the oxide are intensively modelled. While BGS appear in EELS as an isolated feature, expected signatures of electronic conduction are pointed out. The emphasis is put on the broadening of the quasi-elastic peak and on the phonon screening. A discussion on sampling depth is then developed to understand experiments performed in the next chapter. Finally, the chapter ends with the description of resolution enhancement of HREELS spectra by the iterative semi-blind Lucy-Richardson algorithm [35]. The latter helps revealing the existence of a mixed plasmon/phonon excitations.

The understanding of the origin and properties of the band gap states is hindered by the inability to experimentally distinguish the respective contributions of Ti_{int} and O_b-vac to the formation of those states. Chap. 4 is dealing with this issue by using EELS through experimental procedures often unexplored due to the scarcity of the method. Designed samples were prepared, with different types of defects that were probed by EELS upon annealing, cooling, exposure to electron beams and exposure to either oxygen or water. Off-specular geometry was used to go from bulk-sensitive to surface-sensitive conditions. Direct observations of BGS associated either to Ti_{int} or O_b-vac were achieved. The chapter ends with a schematic representation of the excess electron profile through the surface region.

Relying on the conclusions gained in Chaps. 3-4, dielectric theory is used in Chap. 5 to fit (HR)EELS spectra as a function of oxygen exposure and temperature. More arguments are given to support the schematic representation of the excess charge profile. The obtained characteristics of "bulk" and "surface" electrons are discussed in the light of the existing literature. It is demonstrated that both have a dual behaviour, appearing as deep level in EELS or as carriers in HREELS. The present findings favour a picture of quite delocalised or free-like carriers.

CHAPTER 2

ELECTRON ENERGY LOSS SPECTROSCOPY: EXPERIMENTAL SET-UP AND METHODS

The development of ultra-high vacuum (UHV) techniques [36, 37] is essential to surface science. It is common sense that it is essential to keep clean the surface under study, since even a small amount of adsorbate may produce drastic modifications of its intrinsic properties. For this reason, the changes that are undergone by the surface during measurements have to be perfectly controlled. Within the framework of the kinetic theory of gases, the impinging rate r_a of a gas on a surface (defined as the number of atomic or molecular collisions per unit area per unit of time) is given by $r_a = n\nu_{aver}/4$ where n is the number of atoms (or molecules) per unit of volume in the surrounding atmosphere and ν_{aver} is their average speed. The gas being considered as ideal [1], $n = p_{gas}/k_BT$ where p_{gas} is the pressure of the gas, k_B the Boltzmann constant and T the absolute temperature. Since the Maxwell-Boltzmann distribution of species velocity gives $\nu_{aver} = (8k_BT/\pi m_{gas})^{1/2}$ where m_{gas} is the mass of the atom (molecule) of gas, the impinging rate is just a function of gas pressure and temperature $r_a = P_{gas}/\sqrt{2\pi k_BTm_{gas}}$. Considering convenient units, the impinging rate expressed in $\mathrm{cm}^{-2} \cdot \mathrm{s}^{-1}$ is given by $r_a \approx 2.633 \times 10^{22} p_{gas}/\sqrt{TM_{gas}}$ where p_{gas} is in mbar, T in K, and M_{gas} is molecular weight of the gas in gram. To go further in the order of magnitude, let's assume that all molecules arriving at the surface stick and are incorporated into the surface of the material in the form a monolayer which consists of about $10^{15}.\mathrm{cm}^{-2}$. In the case of water, a gas which currently appears in the residual atmosphere in UHV systems, it takes less than 3 seconds at a partial pressure of 10^{-6} mbar at room temperature to cover a bare surface with a full monolayer. This notion of impinging rate is at the origin of a unit of exposure, the so-called Langmuir [36, 37], from the name of the scientist who layed the foundations of surface science and has drawn attention to the concept of surface coverage. A Langmuir corresponds to an exposure of 10^{-6} torr (1.33×10^{-6} mbar) during one second. As an order of magnitude, it is currently said that an exposure of 1 Langmuir results in the formation of a full monolayer.

[1] An hypothesis all the more true for rarefied atmosphere such as ultra-high vacuum.

Assuming a residual background of water vapour, the above formula shows that it takes at least 8 hours to fully cover the surface at 10^{-10} mbar. This time, which is sufficient to analyse the bare surface or to cover it with a controlled amount of chosen adsorbates, explains why surface science studies are currently performed in UHV conditions corresponding to residual pressures in the low 10^{-10} or even in the high 10^{-11} mbar range.

The present work focuses on the reactive properties of rutile single crystal (110) surface towards oxygen, water vapour or both. Experiments have been performed in a UHV system equipped with a High Resolution Electron Energy Loss Spectrometer (HREELS). The UHV system, the sample, its preparation and the electron energy loss technique which is at the heart of the present work are described successively in what follows.

2.1 The ultra-high vacuum system

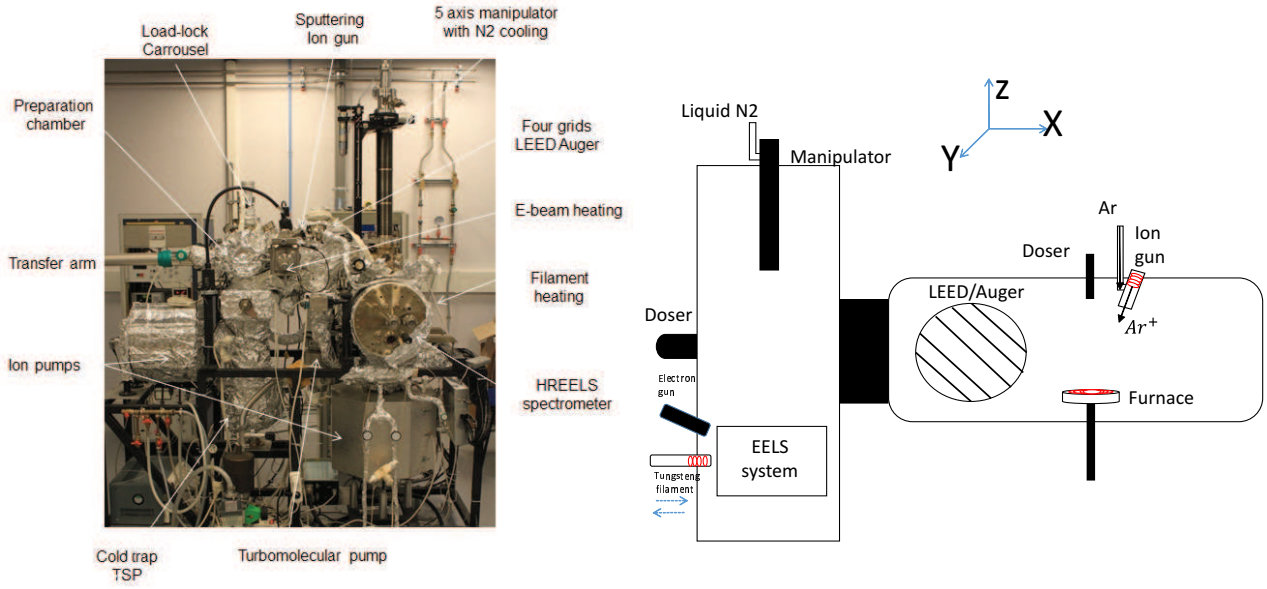

Figure 2.1: (Left) Picture of the experimental setup used in this work. (Right) Schematic drawing of its relevant components.

All experiments have been performed in an UHV system depicted in Fig 2.1. The system consists of three chambers separated by gate valves: (i) a load-lock, (ii) a preparation chamber and (iii) an analysis chamber housing the HREELS spectrometer (LK2000, LK-Technologies [38]) which will be described in Sect. 2.3.2. Pressures in all chambers are measured with hot filament Bayard-Alpert gauges (Varian type) calibrated on nitrogen sensitivity.

The preparation chamber is pumped down to a base pressure of 3×10^{-10} mbar after bake-out by a combination (i) of a molecular turbomolecular pump (Leybold, 250 l/s) evacuated by a rotary pump (Alcatel, 10 m^3/h), (ii) of a ion pump (Riber, 400 l/s) and (iii) of a titanium

sublimation pump (Varian) enclosed into a cold trap. The sample can be transferred and annealed on a compact home-made 5-axis manipulator [2]. The sample mounted on Mo-back plate can be heated up to 1500 K either radiatively by a spiral tantalum/tungsten filament or by electron bombardment by applying a negative high voltage to the filament and the wenhelt surrounding it. The sample temperature is measured by an optical pyrometer calibrated once by spotwelding a thermocouple on the sample backplate. An ion gun (Specs, 10/35) equipped with a leak valve is placed in line of sight of the sample and is used to sputter the substrate with Ar^+ ions. The preparation chamber is equipped with a four grids LEED-Auger (Low Energy Electron Diffraction/Auger spectroscopy, ErLEED from SPECS) apparatus. It allows to check the crystallinity of the sample via the quality of the diffraction pattern and also to perform Auger electron spectroscopy (AES) via electronic emission of the sample when excited by an incident electron beam. AES is used to detect surface impurities with a limit of a few percent of monolayer. The principle and theory of LEED and Auger spectroscopy and the method of using retarded field to record Auger data by means of four-grids device is explained in several references [37, 39].

The sample could be transferred by the way of mechanical arm to the main HREELS chamber where a base pressure of $< 5.10^{-11}$ mbar is maintained thanks to a combined TSP-ion pump (Meca 2000, 400l/s). The sample is hld on a manipulator with 5 degrees of freedom: 3 translations (X,Y,Z), a rotation along the Z direction, and a tilt along X direction. Its head is made out of cooper [3] to allow a fast and efficient cooling by flowing liquid nitrogen. A Au foil is inserted between the Mo support plate on which the sample is firmly clamped and the two side polished $TiO_2(110)$ crystal to ensure a good thermal contact while cooling [4]. A kapton enclosed heater sandwiched between copper plates on which the sample holder is placed allows the regulation of the sample temperature through a PID regulator between 100 and 550 K. The temperature is monitored by a K-thermocouple clamped on the sample manipulator and cross-checked from the Boltzmann ratio of the loss and gain phonon peaks of TiO_2. An ancillary electron gun (Riber) with a focus lens is mounted in line of sight of the sample at an incident angle of 45°. It is used to bombard the sample with an electron current up to $1\mu A/cm^{-2}$ to create defects at beam energies ranging from 25 to 2000 eV. Finally a tungsten filament is placed in front of the sample at an adjustable distance from 1 to 40 mm. The use of this filament to anneal the surface is discussed in Chap. 4.

Gaz dosers made of a bundle of high aspect ratio (> 40) tubes are mounted in both chambers to increase the local pressure on the sample placed at a distance of around 1 mm [40]. All exposures will be given in Langmuir (L). If not specified, low dosing is done via the back-filling of the vacuum chambers. Both chambers are connected to an ancillary gas pipes manifold. Scientific grade O_2 and Ar gases are used while H_2O is purified by several freeze-pump cycles.

[2] These degrees of freedom are used for differential reflectivity measurements during thermal evaporation.

[3] And more generally from non magnetic metals to avoid disturbances of low energy electron trajectory.

[4] Several mounting methods have been tested among which ceramic paste or indium glueing but the Au foil inserted between a polished Mo plate and a polished crystal turned out to be the most efficient for both cooling and high temperature annealing.

2.2 The TiO_2(110) surface and its preparation

2.2.1 Bulk rutile titanium dioxide

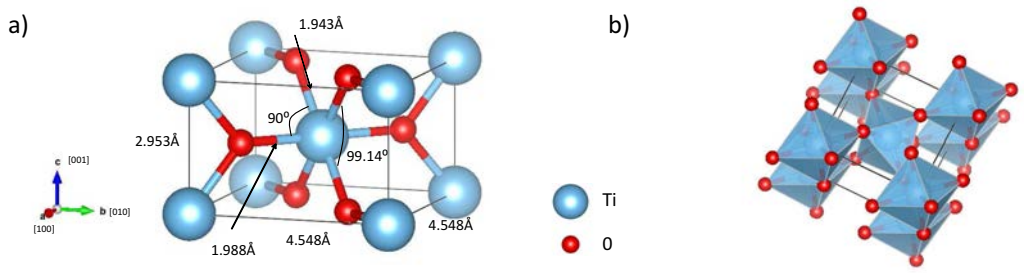

Figure 2.2: a) Ball-and-stick model of the tetragonal unit cell of rutile TiO_2; b) Coordination polyhedra around Ti atoms in rutile. Only corner sharing octahedra are present.

Titanium dioxide (TiO_2) has several crystal polymorphs among which the major three are: rutile, anatase and brookite. While both rutile and anatase are mainly involved in application and scientific research field, only the high temperature form *i.e.* rutile [5] is studied in this work. It has a tetragonal unit cell (space group $P4_2/mnm$) which consists of two titanium (Ti) and four oxygen atoms (O) with lattice parameters $a = b = 4.548$ Å and $c = 2.953$ Å. The basic building block is a slightly distorted octahedron formed by one Ti atom with its surrounding six O atoms. Octahedron are stacked with their long axis alternating by 90° to form the crystal, as shown in Fig 2.2-b. Bond lengths between Ti and O atoms are 1.943 Å and 1.988 Å for the four-fold symmetric and two-fold symmetric bonds respectively. Rutile TiO_2 has a band gap of around 3 eV (see Sect. 3.2.2). This ionocovalent material (Ti:$[Ar]3d^24s^2$ / O : $[He]2s^22p^4$) has a valence band dominated by O 2p states and its conduction band is mostly derived from Ti 3d orbitals but with some partial hybridization.

Rutile is the archetype of reducible oxide and many of its specific properties are linked to the reduced form TiO_{2-x} that formally corresponds to the reduction of Ti^{4+} ions into Ti^{3+}. This reduction can result from the formation and ionization of defects, either oxygen vacancies (V_O) or titanium interstitials (Ti_i) which reads in the KrögerVink notation:

$$\begin{aligned} 2Ti^{4+} + 4O^{2-} &\rightarrow Ti^{3+} + V_O^{\cdot} + \frac{1}{2}O_2 + 3O^{2-} \rightarrow 2Ti^{3+} + V_O + \frac{1}{2}O_2 + 3O^{2-} \\ 2Ti^{4+} + 4O^{2-} &\rightarrow Ti^{3+} + Ti_i^{\cdots} + \frac{1}{2}O_2 + 3O^{2-} \rightarrow 2Ti^{3+} + Ti_i^{\cdot\cdot} + \frac{1}{2}O_2 + 3O^{2-} \ldots . \end{aligned} \quad (2.1)$$

Reduction which is obtained most of the time through annealing under vacuum can proceed upon the precipitation of defects into crystallographic shear plane up to defined suboxides [3] [6]. The dominating types of defects in the bulk were studied experimentally by the group of J. Nowotny (see review [41] and references therein). They have determined

[5] Also available as large single crystals.

[6] Such a level of reduction was never reached in our study since the TiO_2(110) surface always stayed (1×1)

the equilibrium constants of the formation of all defects based on a combination of various measurements. The formation of bulk V_O seems more favorable in surface science conditions (UHV annealing) than Ti_i in agreement with *ab initio* electronic calculations [14, 26, 42–45]. But other authors also introduced the question of interstitial oxygens [46] or titanium vacancies [41] in the problem.

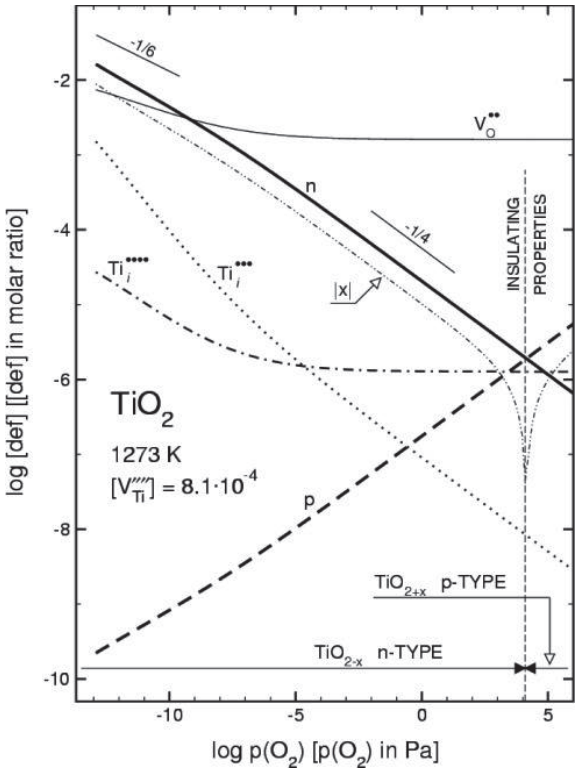

Figure 2.3: Defect disorder diagram showing the effect of oxygen activity at fixed temperature ($T = 1273$ K) on the concentration of ionic and electronic species in TiO_2 (From Ref. [47]).

The diffusion mechanism of V_O and Ti_i is very different. Oxygen vacancies diffuse in a site exchange method. While the most favorable channel for titanium interstitial was supposed to be along the open [001] direction, latest calculations found it along the [110] direction [42] with a barrier lower by 1 eV compared to oxygen vacancies through an interstitialcy mechanism (sometimes called as kick-out) mechanism, in which the diffusing atom kicks out one of bulk titanium atom and takes its lattice position. This theoretical study agrees with the experimental findings of M.A. Henderson, where the healing of the sputtered TiO_2(110) surface is found to proceed through an inward diffusion of Ti interstitials upon annealing in vacuum [48] or through an outward diffusion in oxydative conditions [49] inducing a regrowth of TiO_{2-x} pacthes on the surface [23]. The activation barrier of Ti diffusion has been estimated to 1.0 eV by Z. Zhang et.al [50] on the basis of electron stimulated desorption measurements performed during annealing in the 360-400 K temperature range. Similar values were reported by another experimental study of oxygen uptake [49] and by theoretical approaches [14].

Although reduced rutile is a n-type semiconductor, the mechanism of the electronic conduction, the localisation of the charges associated to the defects, the charge state of the defect and the major contributions to the observed band gap states are still debated and will be

discussed in depth in the forthcoming chapters.

2.2.2 The TiO_2(110) surface

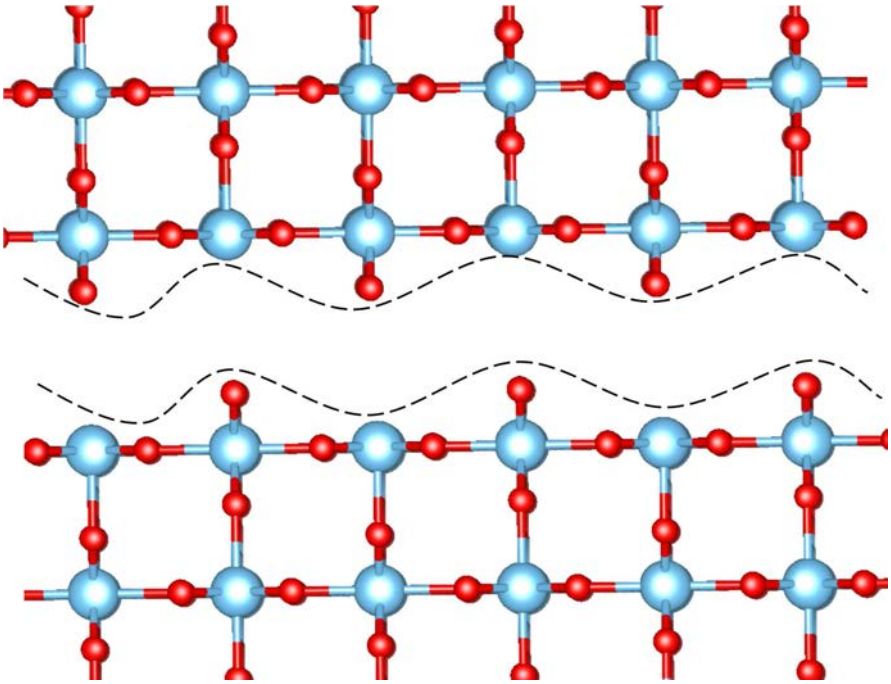

Figure 2.4: The bulk terminated rutile TiO_2(110) surface.

The TiO_2(110)(1×1) surface is the most energetically stable surface of rutile. It is an archetypal substrate which has drawn an extraordinary scientific interest in the surface science field (see for instance review papers [2–8] or book [9]) in particular in relation with the photo-catalytic activity of titanium dioxide. It is available as large single crystals, it is a relatively good conductor which allows to use charged probe species and it offers the incredible opportunity to look at the reactivity of point defects at the atomic scale with Scanning Tunnelling Microscopy (STM). The TiO_2(110) surface is nearly bulk terminated and non-polar [51]. The auto-compensation criterion requires that formal charges due to cation-derived dangling bonds compensate that from anion-derived dangling bonds in order to obtain a stable surface. Cutting along the dashed line shown in Fig 2.4 ensures that the same number of oxygen-to-titanium bonds are broken as titanium-to-oxygen bonds. As shown in Fig 2.5, the stoichiometric TiO_2(110) surface consists of alternating rows of fivefold-coordinated Ti (Ti_{5c}) atoms and protuding twofold-coordinated bridging oxygen (O_b). The Ti atom beneath O_b is sixfold-coordinated (Ti_{6c}), and a row of threefold-coordinated oxygen atoms (O_{3c}) is located between Ti_{5c} and O_b rows. The surface unit cell of TiO_2(110) is rectangular with lattice parameters of 2.96 Å along the O_b row direction and 6.49 Å normal to it. The structure mentioned above ensures that the surface containing twice as many O^{2-} as Ti^{4+} ions is charge neutral. Along the direction normal to the surface, the spacing between Ti_{6c} planes is 6.49 Å.

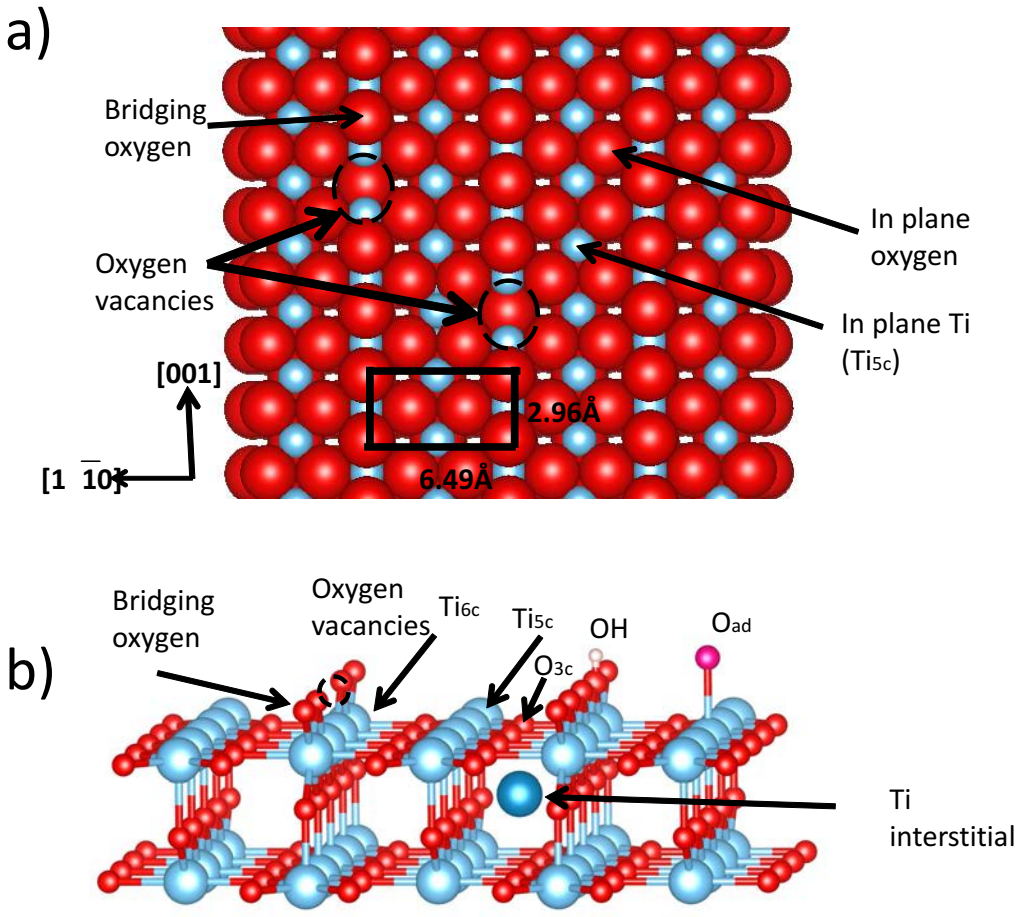

Figure 2.5: Ball model of the TiO_2(110) surface: a) top-view along the [110] direction; b)side view. Typical defects of the surface are shown in figure: oxygen vacancy O_b-vac, hydroxyl group OH_b, titanium insterstitial Ti_{int} and adsorbed oxygen O_{ad}. The notation of defects that will be used hereafter is common in the surface science field.

The most studied defects on the TiO_2(110) surface are oxygen vacancies [2–8] that are formed on the O_b row (O_b-vac) (Fig 2.5), and which readily appear in STM as a bright spot in between Ti_{5c} rows. While the exact mechanism of O_b-vac formation is not known, resonant photoemisson and DFT studies have shown that excess charges of two electrons per vacancy fill the unoccupied 3d orbitals of the Ti^{4+} ions. But the spatial location of this charge is still under investigation. More and more evidences have been reported that those charges are not on the very surface layer but on the subsurface Ti_{6c} atoms with a complex and dynamic distribution among Ti atoms [22, 34, 52–54]. There are many ways to create O_b-vac such as sputtering/annealing and electron bombardment. Sputtering/annealing, the easiest one, produces both O_b-vac and Ti_{int}. Those two defects can hardly be distinguished experimentally through their spectroscopic fingerprints. Interestingly, K. Mitsuhara *et al.* [55] have shown that O_b-vac are not created by annealing below 870 K. Electron bombardment creates O_b-vac via the Knotek-Feibelman process [56]. In this process, the incident energetic electron creates a 3p hole in Ti atoms. Since Ti atoms in TiO_2 poorly contribute to the valence band, the

two electrons that are necessary for Auger hole decay must be provided mostly by O atoms through a inter-atomic Auger decay. After losing their electrons, the surface oxygen atoms become electrically neutral (even become O^+ as a result of the double Auger process and share remaining valence electrons with Ti atom) and desorb. The threshold electron energy of 34 eV [56, 57] corresponds to the Ti 3p hole level creation. Several authors reported that electron bombardment only creates O_b-vac and does not rearrange defect distribution beneath the surface layer [11,12,58]. O_b-vac readily react with adsorbed molecules among which water which creates two bridging hydroxyl groups (OH_b) per vacancy, one filling the vacancy and the remaining hydrogen sitting on neighbouring bridging oxygen atoms. The reaction with O_2 replenishes the vacancies and releases extra-O_{ad} which remains on the Ti_{5c}. O_b-vac, O_{ad} as well as OH groups can diffuse along the bridging oxygen row through complex mechanisms. A detailed description of the reaction and diffusion mechanisms with temperature of those species on TiO_2(110) have been described in details in excellent recent reviews [2–9].

2.2.3 The surface preparation

Initially, several cycles of (i) sputtering with 1 keV Ar^+ ions during 10 mins followed (ii) by annealing at $T = 1100$ K during 20 mins are carried out to obtain a sample with a sharp LEED (1×1) pattern and free of contaminants as judged by Auger spectroscopy and also confirmed by the lack of CH stretching frequency in HREELS and a good reflectivity. During this treatment, the sample, which was initially yellow pale, becomes dark blue, reflecting a high conductivity associated to the formation of bulk defects. Those defects eliminate the charging problem when the surface is probed by the low energy electron beam of HREELS.

Several surfaces have been compared throughout this work:

- **R-TiO_2(110)** : the vacuum annealed surface (pristine surface after preparation) or reduced surface with a sizeable concentration of oxygen vacancies [7];
- **O-TiO_2(110)** : a "fully oxydized" surface prepared by annealing in oxygen (5×10^{-6} mbar) at 1100 K for 20 mins after sputtering and also cooled down in oxygen to room temperature (RT). This oxygen treatment is supposed to heal almost all the defects that contribute to the band gap states [58];
- **E-TiO_2(110)** : an electron bombarded O-TiO_2(110) during 1 hour with a beam energy of 75 eV and a current intensity of $\sim 1\mu$ A/cm^{-2}. This method described in Chap. 4 already used by several authors [11,12,57,59] is supposed to create surface vacancies by electron stimulated desorption of oxygen through the Knotek-Feibelman process [56];
- **A-TiO_2(110)** : a surface softly annealed in a controlled way by means of a filament set up in front of the sample [8] (Fig 2.1). Different surface temperatures can be achieved

[7] Despite the low vacuum of the HREELS chamber, hydroxylation by residual water is not to be excluded on the time scale of measurements but as shown afterwards and in the literature this does change the electronic structure of the surface and the excess charges.

[8] Owing to the large distance and the complete shielding of the emission filament, the electron gun used to prepare E-TiO_2(110) does not produce any thermal radiation on the sample.

as a function of the distance at which the hot filament stands from the surface and of the applied power. The pressure stayed always in the low 10^{-10} mbar during such a treatment. This method discussed in details in Chap. 4 allows to overcome the thermal equilibrium between the subsurface and the bulk of the sample in contrast to the more classical annealing from the back side. To be sure that no spurious electrons are emitted from the filament [9], some tests leading to the same results in terms of band gap state intensity were performed with a hot filament polarized at an high positive potential (100 eV) and a grounded sample. For grounded filament and sample, no sample current could be detected (below 10 pA).

2.3 (High Resolution) Electron Energy Loss Spectroscopy

2.3.1 Introduction: basics of EELS

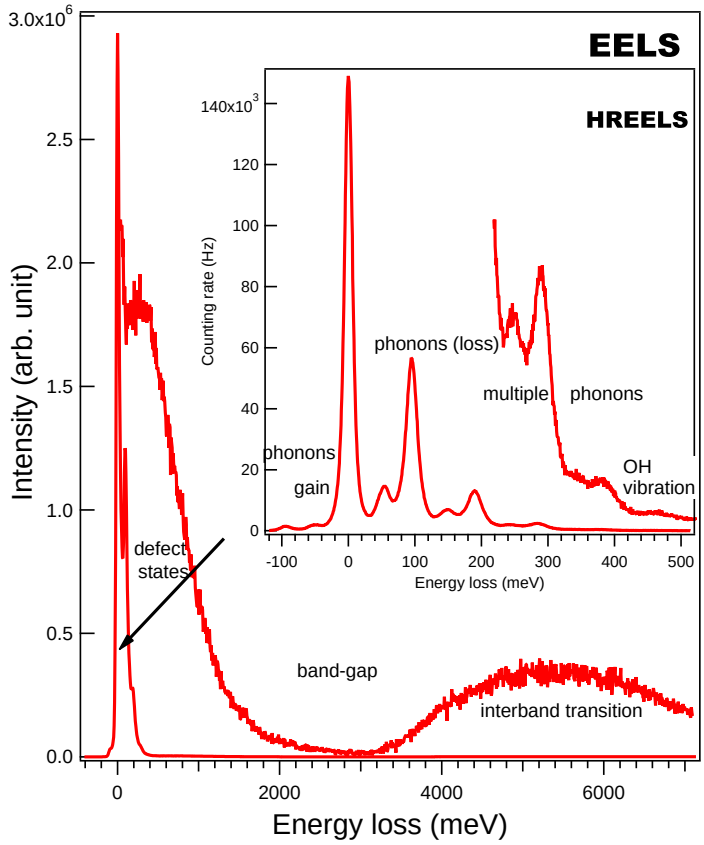

Figure 2.6: Room-temperature EELS spectrum recorded on a reduced $TiO_2(110)$ surface at an impact energy of $E_I = 38$ eV and an incident angle of $\Theta_I = 60°$ with a resolution of 50 meV given by the FWHM of the elastic peak. HREELS spectrum on the same sample ($E_I = 7.5$ eV; resolution 10 meV; $\Theta_I = 60°$) is shown in inset. Aside the quasi-elastic peak, all excitations (surface phonons, band gap states due to stoichiometry defects and interband transitions) are pinpointed in the figure.

Electron energy loss spectroscopy in reflection [10], known as EELS (see reviews [60, 61]), is a surface science technique well adapted to probe all the elementary solid-state excitations

[9] A potential drop of around 10 V is observed in the filament.

[10] EELS is also performed in transmission geometry in electron microscopes but at much high energy (several hundreds keV) which allows to probe deeper electronic levels.

(plasmon [62], phonon, vibration of adsorbed molecules, gap state, interband transition, exciton etc...) of a surface or an interface between materials having a layered structure thanks to the depth sensitivity of the electrostatic interaction. The basic principle is to shine electrons of well defined incident E_I (or impact energy) in the range between a few and a few hundreds electron-volts and to analyse in energy $E_S = E_I \pm \hbar\omega$ the fraction of the scattered electrons. The reflection coefficient is governed in a complex way by E_I and the electronic structure of the target. The lower E_I the lower the penetration depth. On their way down to the surface and also at impact, electrons exchange quanta of energy $\hbar\omega$ with the elementary excitations of the surface or the adsorbate, losing ($-$ sign) or gaining ($+$ sign) energy through mainly an electrostatic interaction. Thus, information can be gained on the electronic properties of the sample itself; also by changing the angle between the incident Θ_I and the scattering Θ_S directions (see Fig. 2.7), the dispersive behaviour parallel to the surface of those excitations can be explored. The interaction of the incoming electrons with the surface can be classified into three modes [61, 63]: (i) long-range dipole scattering, (ii) impact scattering, and (iii) resonance scattering. They are briefly discussed aftewards. High resolution electron energy loss spectroscopy (HREELS) works with the same principle as EELS but (i) with enhanced resolution (down to 0.5-1 meV for the latest generation of apparatuses) to be able to probe low energy excitations and (ii) with low energy electrons (a few eV) to increase surface sensitivity. In particular, the technique was initially developed to look at vibrational properties of surfaces (phonons in ZnO in the seminal paper of H. Ibach [64]) or adsorbed molecules, being in this respect the equivalent of infrared spectroscopy but with an intrinsic surface sensitivity due to the low penetration depth at such impact energies.

Fig 2.6 shows typical EELS and HREELS spectra acquired on a reduced $TiO_2(110)$ surface in the specular direction ($\Theta_I = \Theta_S$), in which the various losses in energy are indicated. Those spectra, that are at the heart of this work, will be discussed in depth in the next chapters. Briefly speaking, aside the intense elastic peak close to $\hbar\omega = 0$, three intense surface phonons appear [11], as well as the harmonics and their combinations, *i.e.* the excitation of several phonon quanta. At higher energy, before the onset of band-to-band transitions, stoichiometry defects give rise to a band gap state (BGS) peak. On the negative axis, less intense gain peaks are allowed by the Bose-Einstein population of phonons at finite temperature.

2.3.2 The spectrometer

The scheme of the electrostatic spectrometer that is employed in this work [65] (LK2000 from LK-Technologies [38]), is presented in Fig 2.7. The electron optics technology behind is described in depth in the two books of H. Ibach [61,66] and in the review of Roy and Kimbaly [67].

Electrons which are emitted by a hot LaB_6 [12] filament are first focused by a set of lenses onto the entrance slit of the first monochromator, which consist of a 127° cylindrical deflection analyser [13]. A potential drop of ΔV is applied between the inner and outer parts of the

[11] Nearly longitudinal ones, see Chap. 3

[12] To reduce the work function compared to tungsten hairpin and therefore the thermal spread of the beam.

[13] This angle corresponds to the condition of focussing between the entrance and exit slit [61, 66].

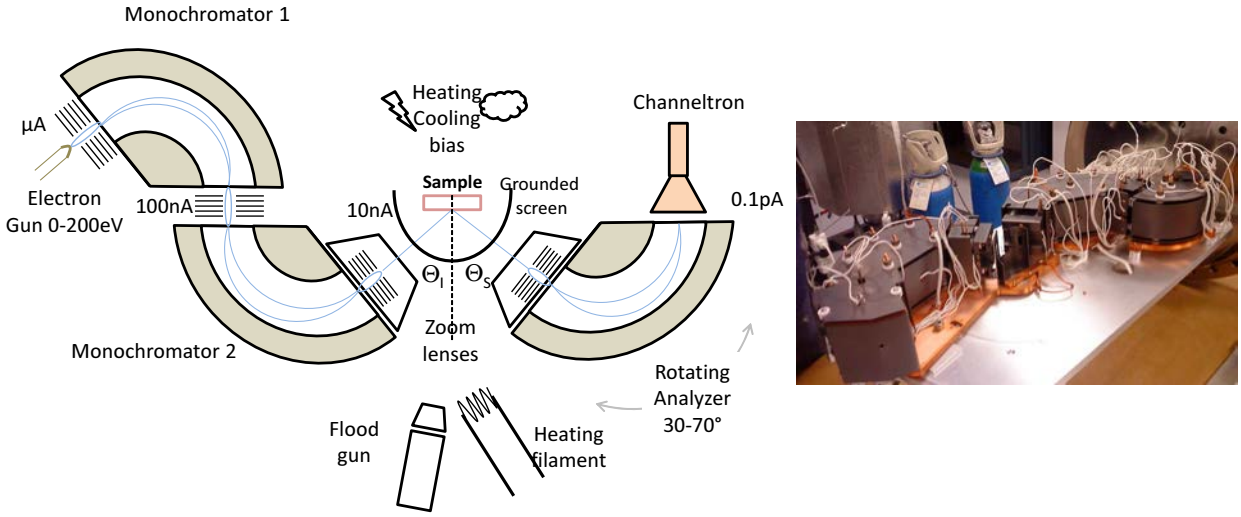

Figure 2.7: The HREELS spectrometer. Electrons emitted by a LaB_6 filament are monochromated by two 127° cylindrical electrostatic sectors. Focussed particles are reflected by the sample prior to being analysed. The signal is finally amplified by a channeltron. The incident angle Θ_I is fixed at 60° (with respect to the direction normal to the surface) and the analyser can be rotated to change the scattering angle Θ_S from 20° to 70°. The sample is mounted on 5-axis manipulator copper head of which can be heated and cooled down. The set-up also involves the above mentioned (Sect 2.2.3) tungsten filament placed in front on the sample to radiatively anneal the surface and the additional electron gun that can be used to irradiate the sample with electrons.

metallic cylindrical sector in such a way that only electrons having the right pass energy E_p (and therefore the right nearly central trajectory for which centrifugal force is compensated by the electric field) can go through the whole assembly. The energy selection [66, 67] reads:

$$\frac{mv^2}{R_0} = \frac{2E_p}{R_0} = e\mathcal{E}_r = \frac{e\Delta V}{\ln(R_o/R_i)R_0}, \tag{2.2}$$

where R_0, R_o, R_i are the central, outer and inner radii of the sector and $\mathcal{E}_r$ is the radial electrical field between outer and inner part. In our instrument, cylindrical monochromators are used, but various others structures could be employed, such as the 42° cylindrical mirror [68] or the 180° spherical one [69]. The resolution of these different electrostatic filters has been discussed by D. Roy and J.-D. Carette [70] and also H. Ibach [66]. For the 127° deflection analyser [61, 65, 66, 70], the resolving power ΔE_b can calculated as the maximum energy deviation ΔE_p on the basis of the electron trajectories in the monochromator and is proportional to the pass energy E_p:

$$\frac{\Delta E_p}{E_p} = \frac{s}{R_0} + \frac{\alpha^2}{3} + \frac{\beta^2}{4}, \tag{2.3}$$

where s is the slit width at the entrance and α and β represent semi-angular apertures parallel and perpendicular to the plane of deflection. Eq 2.3 shows that resolution is mainly controlled by the pass energy of monochromators and the beam divergence. But, at high

resolution, other effects impact ΔE_p, such the space-charge effect induced by the electrostatic interaction between particles [61, 65, 66]. To overcome this limitation and reduce the current load, the design strategy is to feed, still at high current (100 nA) but moderate resolution, a second monochromator similar to the first one [65] with a set of electrostatic lenses in between since the two sectors may work at different pass energies ($R_{0,1} = 35$ mm, $s_1 = 0.5$ mm and $R_{0,2} = 60$ mm, $s_2 = 0.13$ mm; E_p is of a few eV). Focusing or zoom lenses are set symmetrically [71] before and after the sample, they are used to (de)accelerate the monochromated electrons up to impact energy, focus and drive them onto to sample or from the sample onto the entrance slit of the analyser which works similarly to the second monochromator. At its output slit, the signal is amplified by a single electron multiplier. At each stage, the lost current on each optics can be measured with a pico-ammeter; it is reduced from around 1 μA down to 0.1 pA at the channeltron (see Fig. 2.7). The whole set-up is enclosed in three μ-metal shields and all elements are made out of non-magnetic materials to avoid stray magnetic field that would impact on the low energy electron trajectories. A grounded screen is placed in between lenses and the sample in the flight path of the electrons. The sample, most of the time grounded, can be polarized for setting up the instrument; it is mounted on a five axis manipulator which allows to position the surface normal precisely. The incident angle Θ_I [14] is fixed at 60° (from the direction normal to the surface) but the analyser can be rotated to change scattering angle Θ_S from 20 to 70°, to perform out-of-specular measurements.

The ultimate energy resolution can be estimated by Eq. 2.3 but it is usually given by the Full-Width at Half Maximum (FWHM) of the elastic peak. In HREELS, most of our measurements were performed at an energy resolution of around 8 meV FWHM [15] as determined on a metallic substrate (Ag(111) or Pt(111)) at a beam energy around $E_I = 8$ eV. A counting rate on TiO_2(110) between 10^5 and a few 10^6 cps was routinely achieved. In the low EELS resolution mode ($E_I = 38$ eV; 50 meV FWHM), the electron amplifier is close to saturation. Of course, as shown in Chap. 3, the sample itself can cause a broadening of the elastic peak, in particular through the carrier excitations [61] or potential inhomogeneities. A flood gun (useless in the case of conductive TiO_2) can be used to stabilise the surface potential and perform EELS measurements on insulators [72]. All potentials (up to 50!) are computer-controlled and stabilized with special low noise (< 0.5 mV) and low drift (< 1 meV/day) electronic circuitry.

2.3.3 Electron-surface interaction modes and their cross-section

Three scattering modes in EELS (Fig. 2.8) are distinguished on the basis of their mode of interaction [61, 63], each of them has specific selection rules:

- **Dipole scattering** is a long distance electrostatic interaction between electrons and surface through the Coulomb dipole field which is created by the elementary excitations of the surface or the adsorbate. The scattering actually happens far from the surface (several nm; see Sect. 3.2.5). Information from deeper layers can be collected since the electric field created by excitations below surface can "leak" out the sample and "be

[14] It could be changed by rotating the sample.

[15] The best achievable resolution with our apparatus is around 4 meV.

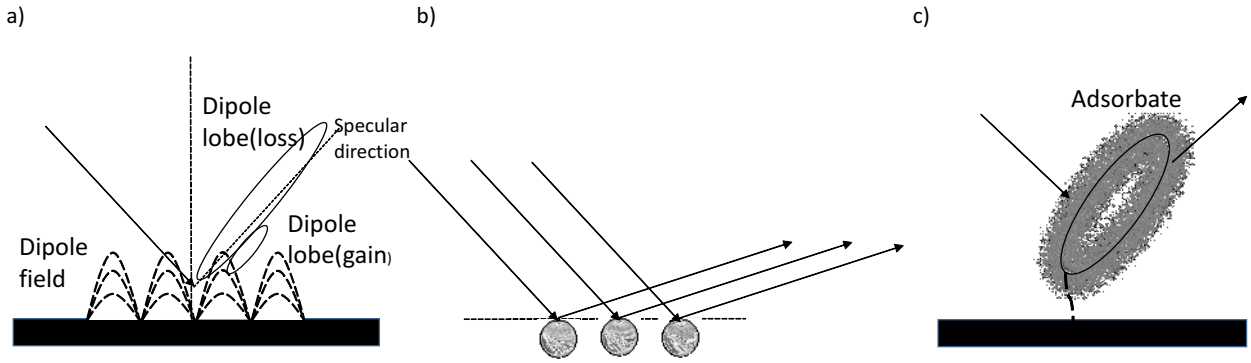

Figure 2.8: Schematic view of the three scattering regimes in EELS: a) dipole scattering where the large and small lobe represent loss and gain events, b) short range impact scattering, c) resonance scattering for which a short-life excited molecule reemits the electron.

seen" by the electrons. Dipole scattering dominates in the specular direction and is concentrated into the well known "dipole lobe" close to the specular direction.

- **Impact scattering** becomes dominant at large deflection angle due to the fast decay of dipole scattering. It is a short range interaction for which electrons are scattered at positions that are very close to the atoms or molecules at the surface, although they interact without being captured [73]. In contrast to dipole scattering for which matter can be treated in a continuous way through its dielectric function, a microscopic theory is required to calculate the cross section of the impact scattering regime which can provide detailed informations on the atomic and electronic structure of the surface.

- **Resonance scattering** is an interaction between electrons and the orbitals of molecules at the surface [73]. Electrons are captured into orbitals and then reemitted. The corresponding energy loss and emission angle are strongly dependent on the nature of the orbitals and on the geometry of the surface molecules [74]. It usually happens in gas phase; in case of adsorbed molecules the life-time of such resonances is expected to be very short [61]. For instance, J.W. Gadzuk [75] found that the life-time of gas phase N_2^- of the order of 10^{-15} s is reduced by 60 % when adsorbed on a surface.

Actually, the different scattering regimes all occur in any given scattering event, but a detailed and accurate global description is untractable. Fortunately, depending on the scattering geometry, appropriate theories of the different regimes have been developed and will be reviewed hereafter.

2.3.3.1 Dipole scattering

While for impact and resonance scattering a microscopic analysis is required, the dipole scattering can be described in a semi-classical way. The two following arguments extracted from Ref. [61] illustrate that, in small-angle inelastic scattering conditions, the scattering field has the character of a dipole field. The specificities of the interaction *i.e.* (i) long range and (ii)

narrow angular distribution (dipole lobe) then become straightforward.

Let's start with a simple case, where an electron is scattered by a small molecule. Suppose that the electron interact with it through a superposition of two body potentials V_l:

$$V(\mathbf{r}) = \sum_l V_l(\mathbf{r} - \mathbf{R}_l), \tag{2.4}$$

where $\mathbf{r}$ is the position of the electron, $\mathbf{R}_l$ that of the nucleus l of the molecule which can be decomposed through $\mathbf{R}_l = \mathbf{R}_l^0 + \mathbf{u}_l$ into an equilibrium position $\mathbf{R}_l^0$ and a vibrational displacement around equilibrium $\mathbf{u}_l$. If the electron is scattered from a wave vector $\mathbf{k}_I$ to $\mathbf{k}_S$, the matrix element involved in the Born approximation or Fermi-golden rule reads:

$$V(\mathbf{k}_I - \mathbf{k}_S) = \frac{1}{V} \int e^{i(\mathbf{k}_I - \mathbf{k}_S)\cdot\mathbf{r}} V(\mathbf{r}) d\mathbf{r}. \tag{2.5}$$

Using $\Delta\mathbf{k} = \mathbf{k}_I - \mathbf{k}_S$, to first order in the atomic displacement field, Eq. 2.4 yields:

$$V^1(\Delta\mathbf{k}) \simeq i \sum_l \left(e^{i\Delta\mathbf{k}\cdot\mathbf{R}_l^0} \int d\mathbf{r} V_l(\mathbf{r}) e^{i\Delta\mathbf{k}\cdot\mathbf{r}} \right) \Delta\mathbf{k} \cdot \mathbf{u}_l. \tag{2.6}$$

In the very small-angle scattering *i.e.* $|\Delta\mathbf{k}| \to 0$, the exponential factors $e^{i\Delta\mathbf{k}\cdot\mathbf{R}_l^0}$ can be set to unity in the previous equation. Using the fact that the Fourier transform of the potential at small wave vector reads:

$$\lim_{|\Delta\mathbf{k}|\to 0} \int d\mathbf{r} V_l(\mathbf{x}) e^{i\Delta\mathbf{k}\cdot\mathbf{r}} = \frac{Z_l e^2}{\epsilon_0 \Delta k^2}, \tag{2.7}$$

where Z_l is the net charge surrounding nucleus at $\mathbf{R}_l^0$ and ϵ_0 the vacuum permittivity, Eq. 2.6 can be recasted in the form:

$$\lim_{|\Delta\mathbf{k}|\to 0} V^1(\Delta\mathbf{k}) = \frac{i\Delta\mathbf{k}}{\epsilon_0 \Delta k^2} \sum_l e Z_l \mathbf{u}_l. \tag{2.8}$$

This equation shows that the final cross section is proportional to $\sum_l e Z_l \mathbf{u}_l$ which is indeed the oscillating portion of the electric dipole moment of the molecule.

Worth to be mentioned again, the dipolar scattering is not of course limited to the vibrations within molecules. In the dipolar regime, incident electrons interact with any change of density of charges that occurs at the surface that may originate from surface phonons, surface plasmon, interband transitions, and even defects states in band gap. To demonstrate this without addressing a specific elementary excitation, let's consider a semi-infinite crystal, with a charge density at ground state $\rho_0(\mathbf{r})$ superimposed with a time-dependent charge perturbation $\rho_1(\mathbf{r}, t)$ which fulfills electrical neutrality $\int d\mathbf{r} \rho_1(\mathbf{r}, t) = 0$. Since the electric field due to $\rho_1(\mathbf{r}, t)$ "leaks" into vacuum above the surface, an electron which is approaching the surface feels a potential:

$$V(\mathbf{r}, t) = \frac{e}{4\pi\epsilon_0} \int_{z'<0} \frac{d\mathbf{r}' \rho_1(\mathbf{r}', t)}{|\mathbf{r} - \mathbf{r}'|}. \tag{2.9}$$

To satisfy the electrical neutrality condition, at large distance from the surface, the leading contribution to $V(\mathbf{r}, t)$ is of dipolar character, as in the simple case of the molecular vibration. But now, no detail is given about the property of the excitation that is treated only as a fluctuation of the charge density. Therefore, no matter what the excitation is, its electric field at large distance from the surface is dipolar in character.

To conclude, long-range interaction and narrow-angle distribution are the main characteristics of dipolar scattering. Several theoretical formulations [61, 63] have been worked out to describe the interaction between a moving electron and a surface excitation in this framework:

- in the **full-classical theory** [76], the electron is treated as a particle moving on a classical trajectory and interacting with a dielectric medium through its image charge; surfaces and adsorbates are represented by their complex dielectric function and their complex dynamic polarizabilities.
- **the semi-classical version** considers the electron as a classical source of perturbation for the quantized boson field of surface excitations [77–79]. The final expression for the single loss cross section is similar to that which is determined by the full-classical dielectric theory which handles more simply issues of relevance such as material anisotropy and layered structures [80, 81].
- the alternative method is to treat the scattering **quantum-mechanically**, either in the first order (Born) approximation or in a more complicated way including multiple scattering [78].

2.3.3.1.1 Classical single loss cross section in the dielectric approach Historically, the first theoretical formulation of EELS is the so-called dielectric theory, originally proposed to analyse inelastic scattering of high energy electrons [82] and extended by A.A. Lucas and M. Sunjić [76] to the low energy case. The calculation (i) assumes a small loss ($\hbar\omega \ll E_I$) and (ii) neglects retardation effects since the electron velocity is much smaller than the speed of light. It also (iii) assumes that electron penetration into the substrate and the effects of image charge on electron trajectory [83] are negligible, and (iv) ignores multiple scattering events and temperature effects by treating only single loss. In classical electrodynamics, the total energy loss W suffered by the electron due to its interaction with the surface is given by the work done by the polarization electric field in the target $\mathbf{E}_b$ all along the electron trajectory:

$$W = -e \int_{-\infty}^{+\infty} \mathbf{v}_e(t) \cdot \mathbf{E}_b[\mathbf{r}_e(t), t] dt, \tag{2.10}$$

where $\mathbf{v}_e(t)$ is the velocity of the electron at time t. In this picture, one can envision the phenomenon as dielectric losses due to the movement of the image charge into the material. W can also be expressed in terms of the loss probability $P_{cl}(\omega)$ per unit of frequency ω:

$$W = \int_{0}^{+\infty} \hbar\omega P_{cl}(\omega) d\omega. \tag{2.11}$$

$P_{cl}(\omega)$ which is the actual quantity measured in an EELS experiment can be calculated by expanding the electric field $\mathbf{E}_b(\mathbf{r},t)$ into the so-called surface waves through Fourier transform both in time and space domains parallel to the surface:

$$\mathbf{E}(\mathbf{r},t) = \int d\omega d^2\mathbf{k}_\parallel e^{-i\omega t} e^{i\mathbf{k}_\parallel \cdot \mathbf{r}} e^{-|z|k_\parallel} \mathcal{E}(\mathbf{k}_\parallel, \omega, z), \tag{2.12}$$

where $\mathbf{k}_\parallel$ represents the wave vector parallel to the surface and z stands for the vertical position from substrate/vacuum interface $z = 0$. This formula shows that the Fourier components of the field associated with $\mathbf{k}_\parallel$ decays exponentially as a function of z over a distance of the order of $1/k_\parallel$ on both sides of the interface. Therefore, the field from excitations located at an inward distance $1/k_\parallel$ from the surface extends out of the sample and can be felt by the incoming electrons. This is why a reasonable probing depth of the dipolar interaction is given by $d = 1/k_\parallel$.
Using the classical description of the incident electron trajectory $\mathbf{r}_e(t) = t\mathbf{v}_\parallel + |tv_\perp|\,\mathbf{n}$ ($\mathbf{v}_\parallel$ is the electron velocity component parallel to surface and $v_\perp$ the normal component, $\mathbf{n}$ being an normal unit vector directed from surface to vacuum) and understanding that $\mathbf{E}_b$ is linked to the bare electron field in vacuum $\mathbf{E}_e$ through the dielectric properties of the material, one can derive the classical loss probability $P_{cl}(\omega)$. The full calculation can be found in many references [60, 61, 76–81] and will not be repeated here. In case of scattering close to the specular direction, it is given by:

$$P_{cl}(\omega) = \frac{e^2}{\pi^3 \epsilon_0 \hbar} \int_D d^2\mathbf{k}_\parallel \frac{k_\parallel v_\perp^2}{[(\omega - \mathbf{k}_\parallel.\mathbf{v}_\parallel)^2 + (k_\parallel v_\perp)^2]^2} \mathrm{Im}\left[-\frac{1}{1+\xi(\mathbf{k}_\parallel,\omega)}\right], \tag{2.13}$$

where $\xi(\mathbf{k}_\parallel,\omega)$ is the so-called loss function. It will be discussed in depth in the forthcoming chapter in particular for anisotropic media [80] and layered materials [81]. For a semi-infinite homogeneous non-dipersive medium, $\xi(\mathbf{k}_\parallel,\omega)$ is simply the relative dielectric function of the material $\epsilon(\omega)$. The structure of Eq. 2.13 will be detailed in Chap. 3, in particular the integration domain D and the prefactor, which is related to Fourier transform of the field of the bare electron in vacuum:

$$\mathcal{E}_e(\mathbf{k}_\parallel,\omega) = \frac{e}{4\pi^3\epsilon_0} \frac{k_\parallel v_\perp}{(\omega - \mathbf{k}_\parallel \cdot \mathbf{v}_\perp)^2 - (k_\parallel v_\perp)^2}. \tag{2.14}$$

2.3.3.1.2 Semi-classical treatment of multiple losses Eq. 2.13 describes only single loss at 0 K. But when the coupling between the incident electrons and the medium is relatively strong or at finite temperature, the EELS spectrum involves a complex combination of intense multiple energy losses and gains due to the creation and annihilation of quanta of excitations. In a semi-classical description, the electron can be considered as a classical source of perturbation for the quantized boson field of surface excitations [61, 77–79, 84] to describe the multiple absorptions and emissions. In this framework, the total probability loss is expressed as follows:

$$P(\omega) = \frac{1}{2\pi} \int \mathrm{d}t e^{i\omega t} e^{\mathcal{P}(t)} \tag{2.15}$$

$$\mathcal{P}(t) = \int_0^\infty \mathrm{d}\omega' p_{cl}(\omega')[(n'_\omega + 1)(e^{i\omega' t} + 1) + n'_\omega(e^{-i\omega' t} - 1)], \tag{2.16}$$

where $n_\omega = 1/[\exp(\hbar\omega/k_BT) - 1]$ is the Bose-Einstein distribution. The Taylor expansion of the exponential term in Eq. 2.15 shows that the multiple losses follow a Poisson distribution [61, 78] as demonstrated experimentally [64].

2.3.3.2 Impact scattering

Unlike dipolar scattering which happens far from surface, electrons during impact scattering interact with the surface over atomic distances. The process is therefore sensitive to the geometry of the impact site which requires a microscopic analysis. In this respect, the treatment of the interaction is similar to that which is performed in Low Energy Electron Diffraction (LEED).

S. Tong used quantum-mechanical scattering theory and a "muffin tins" model [85–87] to calculate the scattered wave amplitude and to estimate the cross section of impact scattering. Let's consider the scattering by phonons. The scattering amplitude $f(\mathbf{k}_I, \mathbf{k}_S, \{\mathbf{R}\})$ depends on the incident wave vector $\mathbf{k}_I$, on the scattered one $\mathbf{k}_S$ but also on the position vectors of the various nuclear sites represented by $\{\mathbf{R}\}$. When nuclei are at their equilibrium position, there is only elastic Bragg scattering, but when the nuclei are moved away from equilibrium by excitations, here by phonons, inelastic scattering occurs. Since the amplitude of the vibration is small, an expansion in power of the displacement $\mathbf{u}_i$ from equilibrium $\mathbf{R}_i^0$ can be performed. At first order, it reads:

$$f(\mathbf{k}_I, \mathbf{k}_S, \{\mathbf{R}\}) = f(\mathbf{k}_I, \mathbf{k}_S, \{\mathbf{R}^0\}) + \sum_{i\alpha} \left(\frac{\partial f}{\partial R_{i\alpha}}\right)_0 u_{i\alpha}. \tag{2.17}$$

The index α refers to the α^{th} Cartesian component. The displacement $u_{i\alpha}$ operator can be decomposed into a sum of eigenvectors $\xi^s_{i\alpha}$ corresponding to the normal modes s of frequencies ω_s and expressed as functions of the corresponding annihilation and creation operators a^- and a^+ of the vibrational quanta $\xi^s_{i\alpha}$. For normalized $\xi^s_{i\alpha}$ ($\sum_{i\alpha} |\xi^s_{i\alpha}|^2 = 1$), one finds:

$$u_{i\alpha} = \sum_s \sqrt{\frac{\hbar}{2\omega_s m_i}} \xi^s_{i\alpha}(a^- + a^+). \tag{2.18}$$

m_i is the ith nucleus' mass. If only a single vibrational quantum is absorbed, then the matrix element of the transition is given by:

$$\mathbf{M}(\mathbf{k}_I, \mathbf{k}_S; +s) = \langle n_s + 1 \,|f(\mathbf{k}_i, \mathbf{k}_s, \{\mathbf{R}\})|\, n_s\rangle = \sqrt{n_s + 1}\sqrt{\frac{\hbar}{2N\omega_s}} \sum_{i\alpha} \left(\frac{\partial f}{\partial R_{i\alpha}}\right)_0 \frac{\xi^s_{i\alpha}}{\sqrt{m_i}}, \tag{2.19}$$

where N is the number of unit cells, and n_s is the Bose-Einstein statistics. Since the translational symmetry of the lattice only allows given wave vector transfers $\mathbf{q}_\parallel$, modes can be labeled accordingly with the j index that represents all other parameters. Finally, the probability that an electron is scattered by mode $\mathbf{q}_{\parallel,j}$ into solid angle $d\Omega$ reads:

$$\frac{dP}{d\Omega} = \frac{mE_I}{2\pi^2\hbar^2} \frac{\cos^2\Theta_s}{\cos\Theta_I} S\sqrt{n_s + 1}\sqrt{\frac{\hbar}{2N\omega_j}} \sum_{i\alpha} \left(\frac{\partial f}{\partial R_{i\alpha}}\right)_0 \frac{\xi^{\mathbf{q}_{\parallel},j}_{i\alpha}}{\sqrt{m_i}}. \tag{2.20}$$

To calculate this cross section, a theory of lattice vibrations of the surface region is needed to get the frequency and eigenvectors of the normal modes ω_j and $\xi^{\mathbf{q}_{\parallel},j}$. Then, a proper method is required to calculate $(\partial f/\partial R_{i\alpha})_0$. In Tong's approach [86] of the electron scattering process, electron is deflected away from the LEED electron path and follows a subsequent path which can be predicted by photoemisson theory [88] that is to say:

$$\left(\frac{\partial f}{\partial R_{i\alpha}}\right)_0 = \left\langle \mathbf{k}_S \left| g_{PE} \frac{\partial V(\{\mathbf{R}\})}{\partial R_{i\alpha}} \right| \psi_{LEED} \right\rangle, \tag{2.21}$$

where ψ_{LEED} is wave function from LEED theory [85] and g_{PE} describes the out-going wave calculated from photoemisson theory [88]. At last, a reasonable model is required to calculate the potential term $\partial V(\{\mathbf{R}\})/\partial R_{i\alpha}$ which is the "muffin tins" approach in Tong's model.

The derivation of impact scattering cross sections is far from being an easy task and really requires a quantum mechanical treatment of the studied system.

CHAPTER 3

DIELECTRIC MODELLING OF ELECTRON ENERGY LOSS FROM TIO_2

3.1 Introduction

The first HREELS experiments that were performed in the eighties by G. Rocker [89], S. Eriksen [21,90] on rutile and L. Kesmodel [91] on anatase addressed the question of phonon spectra of TiO_2 and pinpointed the existence of a feature in the band gap related to defects. Since that period, only a few groups have used the technique to tackle the question of defect reactivity with probe molecules (H_2O [92], O_2 [93–95], CO [96], CH_2O [97] etc...) by looking at (i) either the evolution of the corresponding stretching frequencies (ii) or the variation of the band gap state intensity. The vibrational analysis on this surface is hindered by the overlap of intense multiple phonon excitations which requires the use of numerical deconvolution technique [92, 98] to reveal the interesting features.
While the n-type conductivity of reduced TiO_{2-x} is used to perform measurements, the existence of collective excitations due to carriers in EELS has never been proved. But, since a sizeable carrier concentration is obtained by reduction [25], their EELS signature is to be expected as in the case of more classical semiconductors [61]. Indeed numerous studies have shown the sensititvity of the technique to surface plasmon, in particular in space-charge layers at the surface of semi-conductors, and the coupling of those excitations to phonons as in ZnO(0001) [97, 99–101], GaAs [102], Si(111) [103–105], InSb(110) [106, 107], InAs(110) [108], GaAs(100) [109, 110], etc.... In most of those works, the dielectric theory was applied to derive physical parameters related to the profile of carrier concentration. Through simulations, this chapter is aimed at pinpointing the expected signatures and the interplay between the various excitations in TiO_2, both on the quasi-elastic peak and on the phonon spectrum. This was partially adressed in the infrared study of J.F. Baumard and F. Gervais [29, 111] or in the first HREELS experiments [21, 89, 90]. But none of the authors accounted simultaneously for the defect related band gap states, the conductivity and their correlation, not speaking about

the gradient of composition and the probing depth. The first HREELS study of G. Rocker *et al.* [89] suspected that "the modification in intensity and frequency of Fuchs-Kliewer phonons may be correlated with concentration of free electrons near the surface"; but they "could not resolve plasmon excitations at low energies due to the linewidth of the instrument and the background of phonons near the elastic peak". Later on, S. Eriksen and R.G. Edgell [21, 90] focussed only the "downward shift and attenuation of the highest energy phonon loss that was attributed to modification of the effective background dielectric constant by defect excitations (BGS)". With P.A. Cox and W.R. Flavell [90], they even tried to simulate the phonon spectra within the dielectric theory; but they were "unable to reproduce the observed changes of intensity without introducing an unduly large downward shift in phonon energy". In the light of this work, this will be assigned to a signature of a carrier excitation. Since that time, despite the burst of publications on TiO_2 (see reviews [2–8]) and on the question of charge localisation (see Chaps. 5 and cited references), this question was not addressed any more.

To better understand and fit experimental data, in particular the results of Fig. 5.3, the idea of this chapter is to pinpoint the main EELS signatures of stoichiometry defects in TiO_2, in particular that of carriers. The chapter starts with an in depth reminder on the EELS dielectric modelling (Sect. 3.2.1) with an emphasis on all theoretical aspects required to fit data (slit integration, anisotropy, layered material). Then follows the build-up of a suitable dielectric function from tabulated data including all the solid-state excitations in reduced TiO_2 from far infrared to ultraviolet (Sect. 3.2.2). In a third step, the impact of carrier absorptions and band gap states on the quasi-elastic peak (Sect. 3.2.4.2) and the phonon excitation (Sects. 3.2.4.3-3.2.4.4) is examined theoretically to determine the sougth signatures of all excitations. Finally, a discussion on the question of probing depth (Sect. 3.2.5) as a function of energy loss and scattering angles is developed to prepare the interpretations in the next chapter. This part concludes with the description of an algorithm, published in Ref. [35], that aimed at improving HREELS resolution and recovering data and point-spread function in semi-blind way using the Lucy-Richardson approach. This algorithm helps unravelling mixed phonon-plasmon excitations. All this input will be used to understand the behaviour of excess charges in Chap. 5.

3.2 Dielectric modelling of EELS from TiO_2 : the interplay between carrier excitations, phonons, band gap states and interband transitions

3.2.1 Theoretical reminder about dielectric theory of EELS

In the present manuscript, all simulations of EELS in reflection have been performed within the semi-classical dielectric theory [60, 61, 76–81] that treats the electron as a classical point particle and the substrate excitations on a quantum point of view. Its relevance in the modelling of EELS spectra in reflection has been proven since the early beginning of the technique [64] and in depth over the years (see reviews [63, 112]). The main required concepts applied to the particular case of anisotropic TiO_2 will be reminded.

3.2.1.1 The single loss probability

Let's consider an electron of incident energy E_I, velocity $\mathbf{v}_I$ and wave vector $\mathbf{k}_I$ ($E_I = \hbar^2 k_I^2/2m = \frac{1}{2}mv_I^2$; m electron mass and $\hbar$ the Planck constant) which impinges on the sample surface at an angle Θ_I before being detected along the direction $\mathbf{k}_S$ (Fig. 3.1). The standard dipole scattering theory considers the electron as a classical particle which follows a nearly unperturbed specular trajectory with a negligible speed variation (*i.e.* $k_\parallel = |\mathbf{k}_{\parallel,I} - \mathbf{k}_{\parallel,S}| \ll k_I$) and bounces off the surface giving rise all along its path to a transient electrostatic field that can exchange quanta of excitations with the substrate.

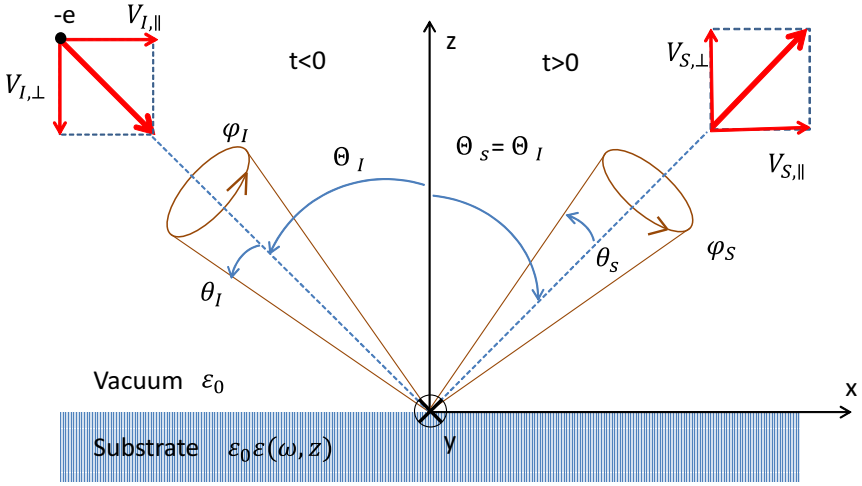

Figure 3.1: Definition of the scattering geometry. The electron travels in vacuum ($z > 0$)-half space (dielectric permitivity ϵ_0) along an unperturbed specular trajectory defined by the average directions Θ_I for the incident beam and $\Theta_S = \Theta_I$ for the reflected or scattered one. The electron velocity before $\mathbf{v}_I = (\mathbf{v}_{\parallel,I}, v_{\perp,I})$ and after $\mathbf{v}_S = (\mathbf{v}_{\parallel,S}, v_{\perp,s})$ reflection are related by energy conservation modulo the energy loss $\hbar\omega$ ($v_I^2 = v_S^2 + 2\hbar\omega/m$). Off-axis trajectories due to finite beam divergence and detector acceptance defines the integration domain $\mathcal{D}$ of the parallel wave vector $k_\parallel$ (see text); they are spotted by their polar and azimuthal angles θ_I, θ_S and ϕ_I, ϕ_S.

The single loss probability P_{cl} for an electron inelastically scattered in an energy window $\hbar d\omega$ around $\hbar\omega \ll E_I$ and close to the specular direction reads [60, 61, 76–81]:

$$P_{cl}(\mathbf{k}_I,\omega) = \frac{e^2}{\pi^3\epsilon_0\hbar}\int_D \frac{k_\parallel v_\perp^2}{[(\omega - \mathbf{k}_\parallel.\mathbf{v}_\parallel)^2 + (k_\parallel v_\perp)^2]^2}\mathrm{Im}\left[-\frac{1}{1+\xi(\mathbf{k}_\parallel,\omega)}\right] d^2\mathbf{k}_\parallel = \int_D F(\mathbf{k}_\parallel,\omega)G(\mathbf{k}_\parallel,\omega)d^2\mathbf{k}_\parallel, \tag{3.1}$$

where $(\mathbf{v}_\parallel, v_\perp)$ are the components of the electron velocity parallel and perpendicular to the sample surface, $\mathbf{k}_\parallel$ is the small parallel wave vector transfer and $e, \hbar, \epsilon_0$ have their standard meanings. Within the full quantum dynamical treatment of the scattering in the Born's approximation, $P_{cl}(\mathbf{k}_I,\omega)$ is modulated by an overall E_I-dependent reflectivity prefactor [61,

78, 79] that accounts for the potential barrier felt by the electron at the sample surface. It is useless in the dielectric analysis but can strongly modulate the absolute experimental intensity through resonances at given energies. The integration in Eq. 3.1 should be performed over a $\mathbf{k}_\parallel$-domain $\mathcal{D}$ (the so-called "slit integration"; Sect. 3.2.1.2) defined by the incoming beam divergence and the detector aperture under the conditions of energy conservation modulo the measured loss $\hbar\omega$.
$P_{cl}(\mathbf{k}_I, \omega)$ involves two terms. On the one hand, the kinematical prefactor or sensitivity function $F(\mathbf{k}_\parallel, \omega)$ depends only on the scattering geometry and gives rise to the angular behavior of the EELS cross section *i.e.* the so-called dipole lobe. On the other hand, the loss function $G(k_\parallel, \omega)$ depends on the effective dielectric function $\xi(\mathbf{k}_\parallel, \omega)$ and therefore on the probed interface. For a homogeneous isotropic non dispersive semi-infinite substrate, $\xi(\mathbf{k}_\parallel, \omega)$ is equal to $\epsilon(\omega)$, the frequency dependent dielectric function of the medium that informs about the solid-state excitations. Since most of the analysis of this work have been performed in the specular direction, no intrinsic $\mathbf{k}_\parallel$-dependence of the material response (*i.e.* dispersive behaviour of the dielectric function) is accounted; but the EELS measurement can be sensitive to such dispersive behaviour along the sample surface [84].

3.2.1.2 The sensitivity function and the slit integration

In the angular coordinates system defined in Fig. 3.1, where θ_I, θ_S measure the angles from the average propagation direction $\Theta_I = \Theta_S$ and ϕ_I, ϕ_S stand for the azimuthal angle looking downwards the origin, the wave vector transfer reads:

$$\mathbf{k} = k_I \begin{cases} -(\theta_I \cos\phi_I + \theta_S \cos\phi_S)\cos\Theta_I + \theta_E \sin\Theta_I \\ -\theta_I \sin\phi_I - \theta_S \sin\phi_S \\ -\theta_I \cos\phi_I \sin\Theta_I - \theta_S \cos\phi_S \sin\Theta_I - 2\cos\Theta_I + \theta_E \cos\Theta_I \end{cases}, \tag{3.2}$$

where $k_I = \sqrt{2mE_I}/\hbar$ is the modulus of the incoming beam wave vector and $\theta_E = \hbar\omega/2E_I$. The previous expression is valid only for small scattering angles close to the average propagation direction, *i.e.* to first order in θ_I, θ_S and for small energy losses $\theta_E \ll 1$.

As demonstrated by Fig. 3.2 in the absence of incident divergence through the comparison to a set of contour lines corresponding to circular slits of half-apertures θ_c (as given by the ellipse equation $[k_x/(k_I\theta_c\cos\Theta_I) - \theta_E \sin\Theta_I]^2 + [k_y/k_I\theta_c]^2 = 1$), the sensitivity function $F(\mathbf{k}_\parallel, \omega)$ displays an intense lobe along the specular direction of half-aperture $\theta_E = \hbar\omega/2E_I$ [61]; its peaks at a value $k_x = k_I\theta_E \sin\Theta_I$.

The fourth order integral of Eq. 3.1 over the incoming/scattering angles for a convergent/divergent beam due to focusing optics is easily doable for any beam shape with the angular variables $(\theta_I, \phi_I, \theta_S, \phi_S)$; for a given direction of the incident beam (θ_I, ϕ_I), the integration volume of Eq. 3.1 is deduced from the Jacobian of the change of variables: $d^2\mathbf{k}_\parallel = k_I^2 \theta_S \cos\Theta_I d\theta_S d\phi_S$. But, in practice, the integration is quite cumbersome and numerically demanding for actual fitting. Therefore, most of the analysis of this thesis have been performed with an equivalent circular detector of half aperture θ_c and a perfectly parallel incoming beam. Moreover, for a circular aperture, if the loss function $G(k_\parallel, \omega)$ depends only on the modulus of the wave vector transfer $k_\parallel$ and not on its direction, the two-dimensional integral can be treated in polar coordinates in the $\mathbf{k}_\parallel$-plane. Since the angular part related

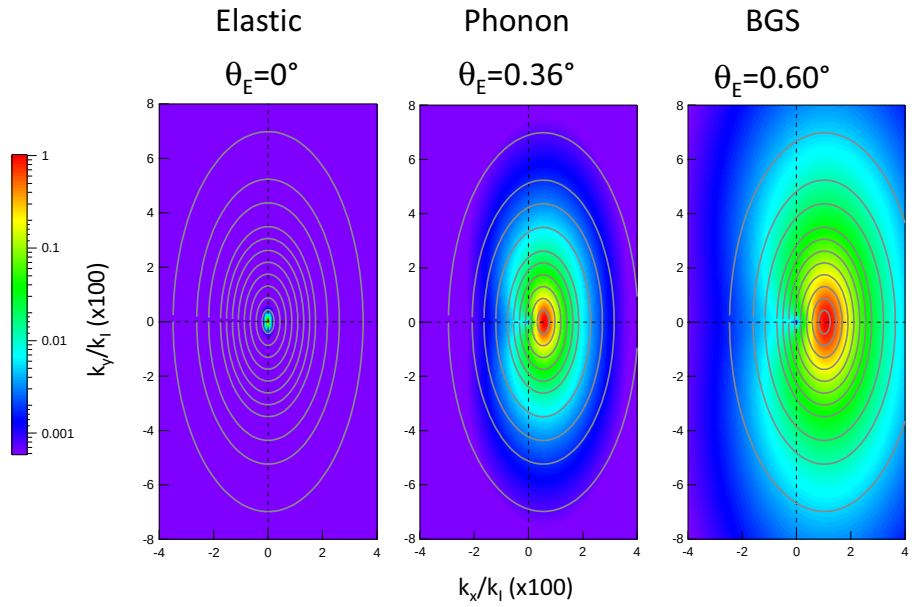

Figure 3.2: $\mathbf{k}_\parallel/k_I$ mapping of the sensitivity function $F(\mathbf{k}_\parallel, \omega)$ at various energy losses (given by θ_E) typical for elastic peak, phonon and band gap states (see Sect. 3.2.2). Contour lines correspond to the domain of integration given by a circular detection slit of half-aperture $\theta_c = 0.25, 0.5, 0.75, 1, 1.25, 1.5, 1.75, 2, 2.5, 3, 3.5, 4°$. $F(\mathbf{k}_\parallel, \omega)$ has been calculated for a perfect incoming beam and has been normalized to its maximum. Its is strongly peaked into a cone of half-aperture close to θ_E.

to the term $F(\mathbf{k}_\parallel, \omega)$ is complex but analytic, the work reduces to a one-dimensional radial integral (see Appendix of Ref. [81] for further details) which speeds up the calculations.
To assess such an hypothesis of an equivalent slit, the exact integrated sensitivity function defined by $\mathcal{F}(\omega) = \int_D F(\mathbf{k}_\parallel, \omega) d^2\mathbf{k}_\parallel$ has been compared to that of circular apertures with no incoming beam divergence. In the case of a material with a $\mathbf{k}_\parallel$-independent loss function $G(\omega)$ (such as for a semi-infinite substrate characterized only by its dielectric function $\epsilon(\omega)$), the classical loss function is simply given by the product of $\mathcal{F}(\omega)$ and $G(\omega)$: $P_{cl}(\omega) = \mathcal{F}(\omega)G(\omega)$. As shown in the abacus of drawn in Fig. 3.3 for various θ_c values, $\mathcal{F}(\omega)$ decreases quickly with the energy loss ($\mathcal{F}(\omega) \sim 1/\omega^3$ when $\omega \to 0$) but the more opened the slit the more intense $\mathcal{F}(\omega)$. Of course, the divergence in detection is limited by the angular acceptance of the analyser. For an elliptic slit of half apertures $(\theta_{c,1}, \theta_{c,2})$ in the directions parallel and perpendicular to the incident plane [1], the comparison made in Fig. 3.3-a demonstrates that it is still possible to find an equivalent circular aperture for $\mathcal{F}(\omega)$ over an energy range which covers the excitations of interest in the present study (phonon, band gap states); as soon as the slit integrates well the sensitivity function $F(\mathbf{k}_\parallel, \omega)$ (see Fig. 3.4), differences are minor. To a certain extent, this conclusion is still valid for a convergent/divergent beam (Fig. 3.3-b). Owing to the quite peaked shape of $F(\mathbf{k}_\parallel, \omega)$, the same finding is to be expected for a $\mathbf{k}_\parallel$-dependent sensitivity function $G(\mathbf{k}_\parallel, \omega)$ that is not dramatically varying with $\mathbf{k}_\parallel$. The simulations of the

[1] To mimic a rectangular slit.

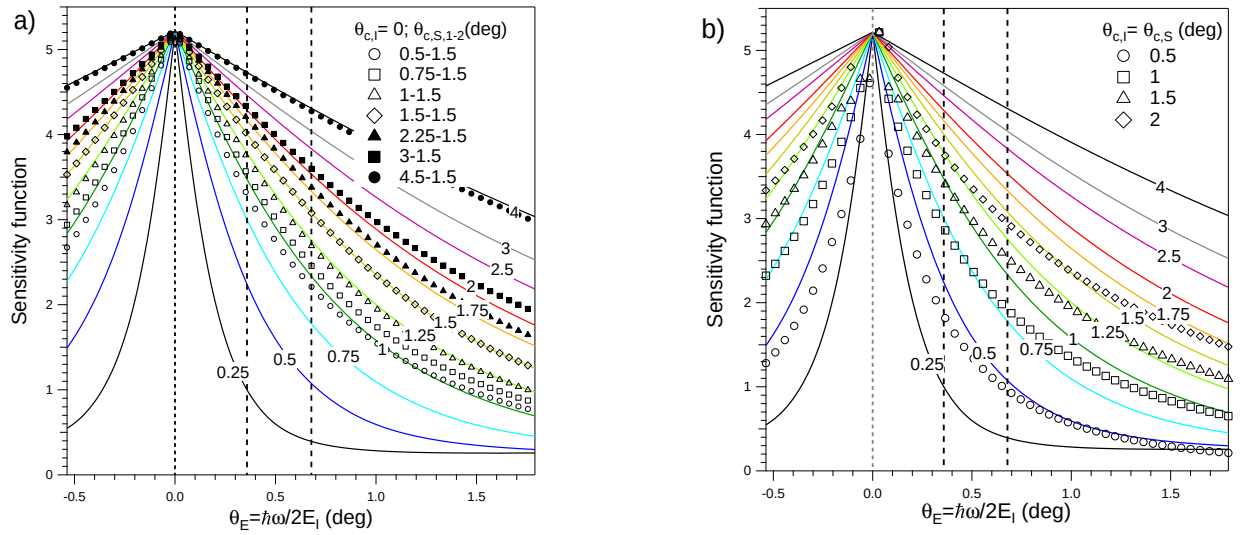

Figure 3.3: Comparison between the integrated sensitivity function $\mathcal{F}(\theta_E = \hbar\omega/2E_I)$ of circular apertures of variable width $\theta_{c,S} = 0.25, 0.5, 0.75, 1, 1.25, 1.5, 1.75, 2, 2.5, 3, 4°$ (full color lines; no incident divergence $\theta_{c,I} = 0°$) with a) the case of an elliptic slit of aperture larger along the incident plane ($\theta_{c,S,1-2} = 0.5-1.5, 0.75-1.5, 1-1.5, 1.5-1.5, 2.25-1.5, 3-1.5, 4.5-1.5°$; $\theta_{c,I} = 0$; symbols) and b) the case of a symmetric convergent-divergent beam with circular apertures of $\theta_{c,I} = \theta_{c,S} = 0.5, 1, 1.5, 2°$ (symbols). The dotted vertical lines correspond to the θ_E-position of the phonon and band gap state that are at the heart of this study.

experimental spectra performed in Chap. 5 use intensively a stratified dielectric function (see Sect. 3.2.1.4) to describe the existence of surface excess electrons for which the loss function depends only on the modulus of $k_\parallel$. As shown in Fig. 3.5 for a typical profile of dielectric function obtained from fitting of actual data, whatever the loss and the beam energy, $G(\mathbf{k}_\parallel, \omega)$ varies much more smoothly compared to the sensitivity function (Figs. 3.2 and 3.4). This finding validates *a posteriori* the use of an equivalent circular slit to describe the integration domain D of Eq. 3.1 even for $G(\mathbf{k}_\parallel, \omega)$ [2]

In the measurements of this thesis, symmetric sets of lenses are used for (de)accelerating and focusing the electron beam from the exit slit of the monochromator to the sample and from this latter to the entrance slit of the analyser [65] (see Sect. 2.3.2). Proper focusing is achieved with a three elements zoom lens for which the electron trajectories have never been really calculated through ray-tracing [3]. However, an estimate of the beam divergence along the dispersive direction of the cylindrical sector analysers (*i.e.* along the incident plane) can be obtained by scanning the integrated elastic beam intensity in out-of-specular direction. The results shown in Fig. 3.6 have been obtained by moving the analyser by an angle $\Delta\Theta$ at fixed monochromator and sample positions. The solid angle overlap $\mathcal{P}(\Delta\Theta)$ (Fig. 3.6) between the acceptances of the perfectly reflected beam $\mathcal{S}_I$ and the analysed one $\mathcal{S}_S$ is given

[2] Notice that this would be not the case for very large thickness. In Fig. 3.5, it amounts to 26 Å.

[3] Private communication from L. Kesmodel of LK-Technologies company, the supplier of our machine.

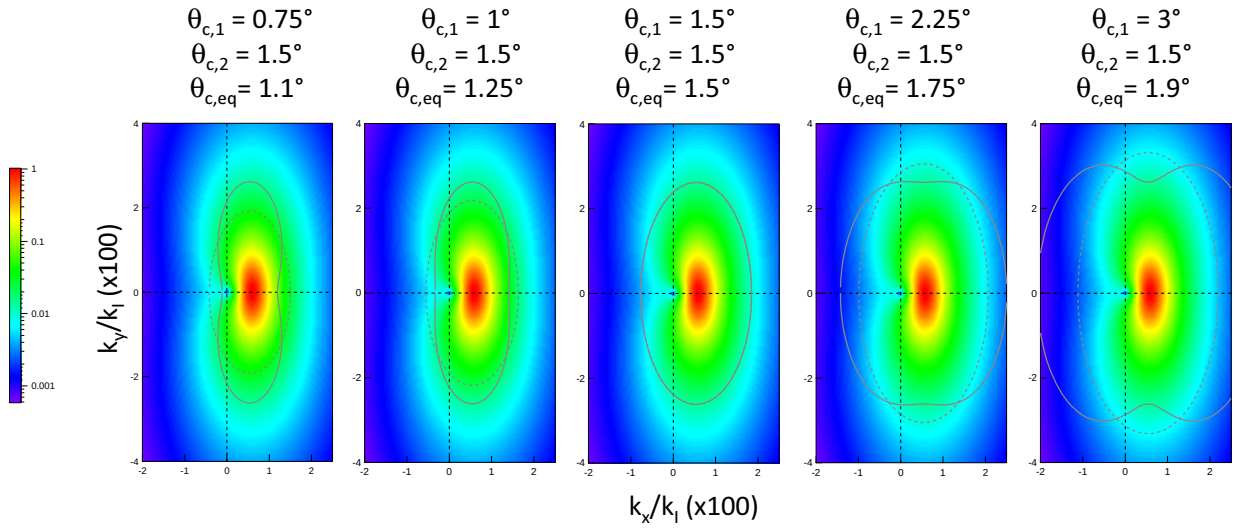

Figure 3.4: In-plane domain of integration D (full curve) (see Eqs. 3.1 and 3.2) for an elliptic slit of half-aperture $(\theta_{c,S,1}, \theta_{c,S,2})$ parallel/perpendicular to the incident plane. No incident divergence is accounted for *i.e.* $\theta_{c,I} = 0$. The plot is done at a $\theta_E = 0.36°$ value typical for phonon and $\Theta_I = 60°$. The comparison (dotted line) is made with the circular slit that best matches the corresponding integrated sensitivity function at this energy accordingly to Fig. 3.3-a. Axes are normalized by the incident wave vector k_I. The sensitivity function $F(\mathbf{k}_\parallel, \omega)$ is superimposed in a logarithmic color scale.

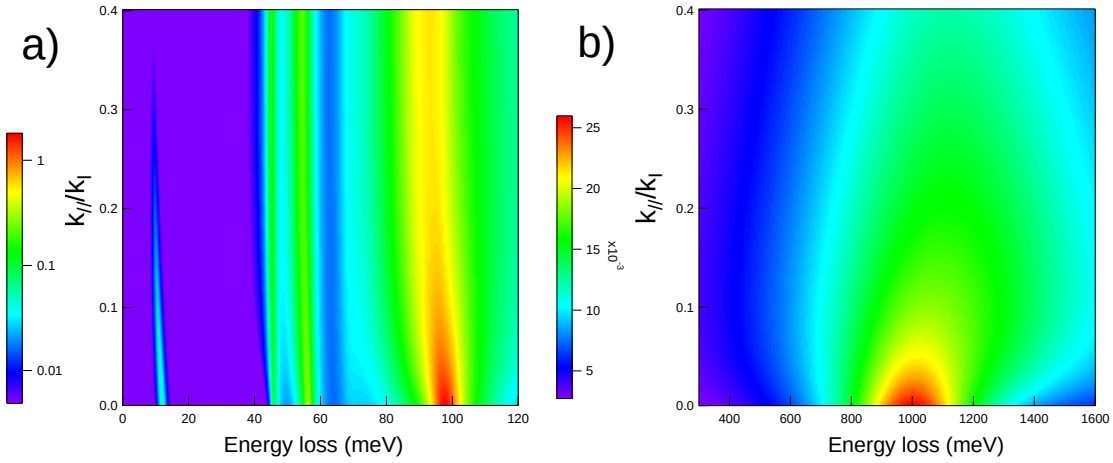

Figure 3.5: Loss function $G(k_\parallel, \omega)$ corresponding to the modelling of experimental spectra of a reduced TiO_2(110) with a stratified dielectric function as performed in Chap. 5 (see Fig. 5.7). The thickness of the layer corresponding to the surface excess electron is $t_{BGS} = 26$ Å. Figures correspond to measurements around a) the phonon range at $E_I = 7.5$ eV and b) the band gap state range at $E_I = 38$ eV.

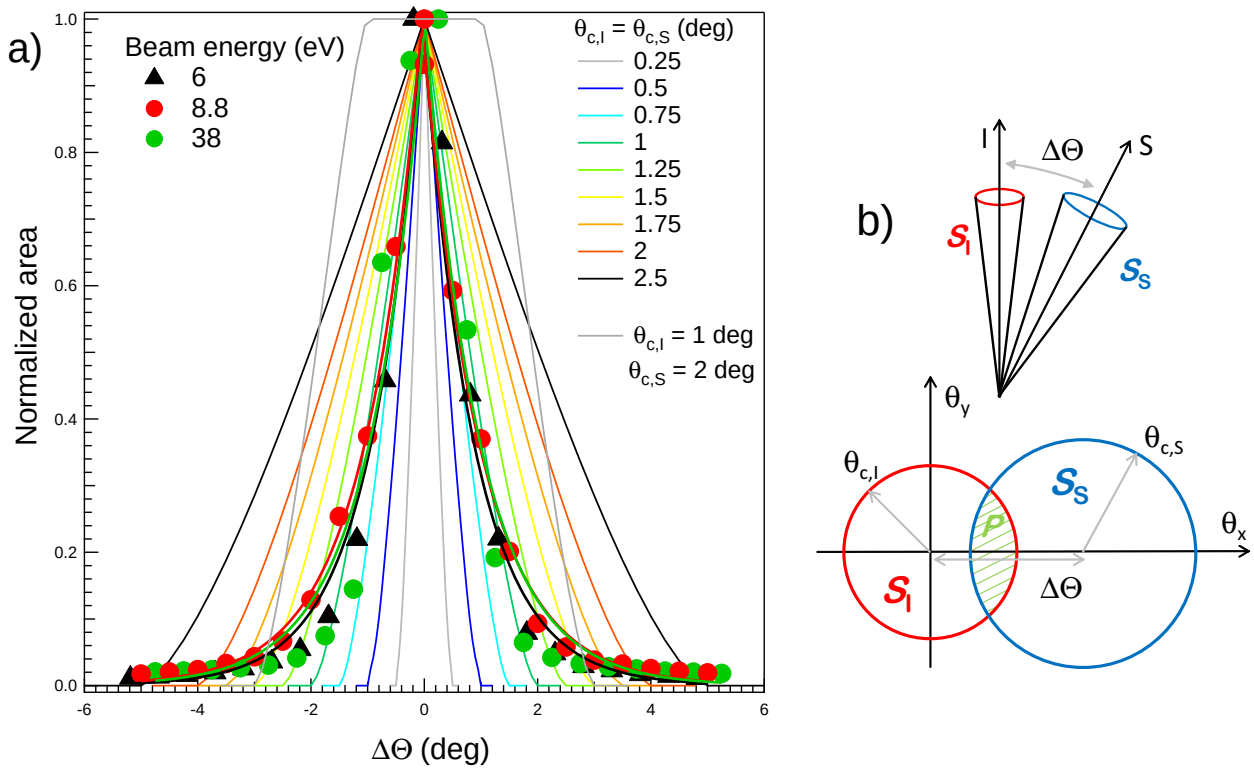

Figure 3.6: a) Integrated elastic beam intensity normalized by the specular value ($\Theta_I = \Theta_S, \Delta\Theta = 0$) as a function of the out-of-specular angle $\Delta\Theta = \Theta_S - \Theta_I$ (see Fig. 3.1). Measurements have been performed at several beam energies $E_I = 6, 8.8, 38$ eV on a reduced $TiO_2(110)$ surface at fixed monochromator position ($\Theta_I = 60°$) by moving the analyser. Data fitted by an exponential decay to guide the eyes are compared to simulations of solid angle overlap $\mathcal{P}(\Delta\Theta)$ between the reflected and detected beams (see text and Eq. 3.4). b) Scheme of calculation of the overlap between the solid angle functions $\mathcal{S}_{I,S}(\Omega)$ corresponding to the reflected I and detected S beams.

by the following convolution along the dispersive direction θ_1 (θ_2 being the direction normal to it):

$$\mathcal{P}(\Delta\Theta) = \frac{1}{\Omega_I} \iint d\theta_1 d\theta_2 \mathcal{S}_S(\theta_1 + \Delta\Theta, \theta_2).\mathcal{S}_I(\theta_1, \theta_2). \tag{3.3}$$

The solid angle function $\mathcal{S}_I(\Omega)$, $\mathcal{S}_S(\Omega)$ are equal to one if the beam is inside or zero outside; the function is normalized to the solid angle of the incident beam Ω_I. For small divergences, $\mathcal{P}(\Delta\Theta)$ is simply given the convolution product of the beam cross section along the dispersive direction. For circular beam of half-apertures $\theta_{c,I}$ and $\theta_{c,s}$, this convolution of disks of radii $\theta_{c,I}, \theta_{c,S}$ is easily calculated by Fourier transform and reads (Fig. 3.6):

$$\mathcal{P}(\Delta\Theta, \theta_{c,I}, \theta_{c,S}) = \frac{4\theta_{c,S}}{\pi\theta_{c,I}} \int_0^{+\infty} dq_1 \cos(q_1\Delta\Theta) \int_0^{+\infty} dq_2 \frac{J_1(\sqrt{q_1^2+q_2^2}\theta_{c,I}) J_1(\sqrt{q_1^2+q_2^2}\theta_{c,S})}{q_1^2+q_2^2}, \tag{3.4}$$

where J_1 the Bessel function of first order. The corresponding set of curves have been calculated for increasing divergences and compared to experimental findings (Fig. 3.6). Firstly, they show that the lenses are set up in a symmetric way since the measurements do not have a plateau around $\Delta\Theta = 0°$ (see grey curve of Fig. 3.6 at $\theta_{c,I} = 1°; \theta_{c,S} = 2°$). Secondly, the experimental angular aperture is very close to $\theta_{c,1} = 0.9 - 1°$ whatever the beam energy. Along the non dispersive direction, the focussing is moderate [4] and a beam divergence $\theta_{c,2} = 1.8°$ can be estimated from (i) geometric slit size $h = 4$ mm at the entrance of the analyser and (ii) the distance to the sample $L_{sa} = 63$ mm. This value is in fact limited by the divergence that can be accepted by the cylindrical analyser. It theoretically amounts to $\theta_{c,2} = h/\sqrt{2}\pi R = 0.85°$ [61, 66] ($R = 60$ mm for our apparatus).

Therefore, all the above analysis show that an equivalent circular detector aperture (with a value around one degree) without incident divergence is a safe and tractable approximation to fit data.

3.2.1.3 Losses from an anisotropic material

For an uniaxial material like tetragonal TiO_2 rutile, the tensor of dielectric constants is anisotropic and diagonal in the main crystallographic axis with two principal components, one normal $\epsilon_\perp(\omega)$ and one parallel $\epsilon_\parallel(\omega)$ to the c-axis. In this case, as demonstrated in Ref. [80], the generalized loss function depends on the scattering geometry and becomes $\mathbf{k}_\parallel$-dependent. Assuming that the c-axis lies in the (x, z)-plane at an angle θ from the surface normal z (see (Fig. 3.7-a)), $\xi(\mathbf{k}_\parallel, \omega)$ is given by:

$$\xi(\mathbf{k}_\parallel, \omega) = \frac{\epsilon_{zz}(\omega)}{k_\parallel}\sqrt{\frac{\epsilon_\parallel(\omega)\epsilon_\perp(\omega)}{\epsilon_{zz}^2(\omega)}k_x^2 + \frac{\epsilon_\perp(\omega)}{\epsilon_{zz}(\omega)}k_y^2}, \tag{3.5}$$

where $\epsilon_{zz}(\omega) = \epsilon_\parallel(\omega)\cos^2(\theta) + \epsilon_\perp(\omega)\sin^2(\theta)$ is the component of the dielectric tensor normal to the sample surface and (k_x, k_y) are the components of the wave vector transfer parallel to the surface. In the case of the $TiO_2(110)$ surface, the c-axis lies in the surface plane along the x-axis ($\theta = 90°$) and $\xi(\mathbf{k}_\parallel, \omega) = 1/k_\parallel\sqrt{\epsilon_\parallel(\omega)\epsilon_\perp(\omega)k_x^2 + \epsilon_\perp(\omega)^2 k_y^2}$. The cumbersome integration in Eq. 3.1 over the detector acceptance and incident beam divergence can be avoided in two extreme cases where $\xi(\mathbf{k}_\parallel)$ becomes poorly $\mathbf{k}_\parallel$-independent. Either the dominant scattering is in the (y, z)-plane *i.e.* $k_x \simeq 0$ and $\xi(\mathbf{k}_\parallel, \omega) \simeq \epsilon_\perp(\omega)$; this is the case of the experiments of this thesis during which the incident plane was normal to the bridging oxygen rows. Or scattering is in the (x, z)-plane *i.e.* $k_y \simeq 0$ and $\xi(\mathbf{k}_\parallel, \omega) \simeq \sqrt{\epsilon_\perp(\omega)\epsilon_\parallel(\omega)}$; in this case, the interpretation is less straightforward as losses result from a geometric mean of parallel and perpendicular dielectric behaviours. Finally, when the c-axis is perpendicular to the surface ($\theta = 0°$) as in the case of $Al_2O_3(0001)$ [113] or ZnO(0001), $\xi(\mathbf{k}_\parallel, \omega) = \sqrt{\epsilon_\perp(\omega)\epsilon_\parallel(\omega)}$ is really $\mathbf{k}_\parallel$-independent.

[4] Private communication from L. Kesmodel of LK-Technologies company, the supplier of our machine.

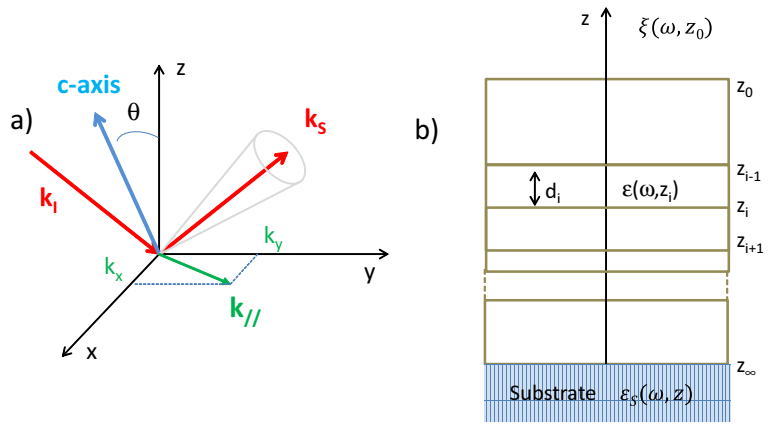

Figure 3.7: a) Geometry of scattering from an uniaxial anisotropic medium. Its main axis lies in the (x, z)-plane at angle θ from the normal to the surface. The wave vector transfer parallel to the surface has two in-plane components $\mathbf{k}_\parallel = \mathbf{k}_I - \mathbf{k}_S = (k_x, k_y)$. b) Stack of layers used in the calculation of the effective loss function of stratified medium.

3.2.1.4 Losses from a stratified medium

Ph. Lambin and coworkers [81] derived also the loss function for a stratified medium with a given profile of in-plane isotropic dielectric function $\epsilon(\omega, z)$. They demonstrated that this quantity is a continuous function of z and found a recursive formula which relates the value of the effective dielectric function $\xi(\omega, z_i)$ at the lower end of a layer of thickness d_i and its dielectric constant $\epsilon(\omega, z_i)$ to the value of the function at the upper end of the layer $\xi(\omega, z_{i-1})$:

$$\xi(k_\parallel, \omega, z_{i-1}) = a_i(k_\parallel, \omega) - \frac{b_i^2}{a_i(k_\parallel, \omega) + \xi(k_\parallel, \omega, z_i)},$$
$$a_i(k_\parallel, \omega) = \epsilon(\omega, z_i)\coth[k_\parallel d_i]; \quad b_i(k_\parallel, \omega) = \epsilon(\omega, z_i)/\sinh[k_\parallel d_i]. \tag{3.6}$$

The starting point of this recursive approach is $\xi(\omega, z_\infty) = \epsilon_S(\omega)$, where $\epsilon_S(\omega)$ is the substrate dielectric function (Fig. 3.7-b). The classical loss probability $P_{cl}(\mathbf{k}_I, \omega)$ is calculated from the surface effective dielectric function, *i.e.* $\xi(\omega, z_0)$, which can be recasted into a continued fraction expansion [81] from Eq. 3.6:

$$\xi(\omega, z_0) = a_1 - \cfrac{b_1^2}{a_1 + a_2 - \cfrac{b_2^2}{a_2 + a_3 - \cfrac{b_3^2}{a_3 + a_4 - \ldots}}}. \tag{3.7}$$

For instance, the loss function for one layer of thickness d of dielectric function $\epsilon_l(\omega)$ over a semi-infinite substrate of dielectric function $\epsilon_s(\omega)$ is analytic:

$$\xi(k_\parallel, \omega) = \epsilon_s(\omega)\frac{\epsilon_s(\omega)\tanh[k_\parallel d)] + \epsilon_l(\omega)}{\epsilon_l(\omega)\tanh[k_\parallel d] + \epsilon_s(\omega)}. \tag{3.8}$$

For actual multilayers, the problem is easily handled recursively on a computer. The generalization to a stack of anisotropic media is slightly more complex [112]. The coefficients a_i, b_i

of Eq. 3.6 become orientation-dependent:

$$\begin{aligned} a_i(\mathbf{k}_\parallel,\omega) &= \alpha_i(\mathbf{k}_\parallel,\omega)\epsilon_{zz}(\omega,z_i)\coth\left[\alpha_i(\mathbf{k}_\parallel,\omega)k_\parallel d_i\right] \\ b_i(\mathbf{k}_\parallel,\omega) &= \alpha_i(\mathbf{k}_\parallel,\omega)\epsilon_{zz}(\omega,z_i)/\sinh\left[\alpha_i(\mathbf{k}_\parallel,\omega)k_\parallel d_i\right] \\ \alpha_i(\mathbf{k}_\parallel,\omega) &= \frac{1}{k_\parallel}\sqrt{\frac{\mathbf{k}_\parallel.\boldsymbol{\epsilon}_{\rho\rho}(\omega,z_i).\mathbf{k}_\parallel}{\epsilon_{zz}(\omega,z_i)} - \left[\frac{\boldsymbol{\epsilon}_{\rho z}(\omega,z_i)\mathbf{k}_\parallel}{\epsilon_{zz}(\omega,z_i)}\right]^2}. \end{aligned} \tag{3.9}$$

In the previous equation, the dielectric tensor has been conveniently decomposed in each layer into the block form:

$$\epsilon(\omega) = \left[\begin{array}{cc} \begin{pmatrix} \epsilon_{xx} & \epsilon_{xy} \\ \epsilon_{yx} & \epsilon_{yy} \end{pmatrix} & \begin{pmatrix} \epsilon_{xz} \\ \epsilon_{yz} \end{pmatrix} \\ \begin{pmatrix} \epsilon_{zx} & \epsilon_{zy} \end{pmatrix} & \epsilon_{zz} \end{array}\right] = \begin{bmatrix} \boldsymbol{\epsilon}_{\rho\rho} & \boldsymbol{\epsilon}_{\rho z} \\ \boldsymbol{\epsilon}_{z\rho} & \epsilon_{zz} \end{bmatrix} \tag{3.10}$$

But fortunately, for an uniaxial material with its c-axis lying in the layer plane as in the case of $TiO_2(110)$, $\epsilon_{zz}(\omega) = \epsilon_\perp(\omega)$ and for a dominant scattering normal to the c-axis, $\alpha(\mathbf{k}_\parallel,\omega) = 1$ while for an incident plane parallel to the c-axis, $\alpha(\mathbf{k}_\parallel\omega) = \sqrt{\epsilon_\parallel(\omega)/\epsilon_\perp(\omega)}$. For completeness, when the c-axis is normal to the layer, $\epsilon_{zz}(\omega) = \epsilon_\parallel(\omega)$ and $\alpha(\mathbf{k}_\parallel\omega) = \sqrt{\epsilon_\perp(\omega)/\epsilon_\parallel(\omega)}$.

3.2.1.5 Mulitple losses

Up to now, the so-called classical description of the dielectric theory by which single loss probability can be calculated [76] has been introduced. When the coupling between the incident electrons and the medium is relatively strong or when the energy loss is of the order of magnitude of k_BT as in the case of surface plasmons, the spectrum involves a complex combination of intense multiple energy losses and gains due to the creation and annihilation of quanta of excitations [64]. The problem at hand can be treated completely quantum-mechanically either in the first Born approximation or in a more complex way including multiple scattering [77,78]. It can also be treated through in a semi-classical way by considering the electron as a classical source of perturbation for the quantized boson field of surface excitations [61,76,84]. Within this more tractable approach, the EELS spectrum $P(\omega)$ at finite temperature T including multiple excitations is obtained from the classical loss function $P_{cl}(\omega)$ through:

$$P(\omega) = \frac{1}{2\pi}\int_{-\infty}^{+\infty} dt e^{-i\omega t}\mathcal{R}(t)e^{[\mathcal{P}(t)-\mathcal{P}(0)]} = e^{-\mathcal{P}(0)}R(\omega)\otimes\left\{\delta(\omega) + \sum_{n=1}^{\infty}\frac{1}{n!}\left[\mathcal{P}(\omega)\right]^{n\otimes}\right\}, \tag{3.11}$$

where:

$$\mathcal{P}(t) = \int_0^{+\infty} d\omega' P_{cl}(\omega')\left[(n_{\omega'}+1)e^{i\omega' t} + n_{\omega'}e^{-i\omega' t}\right]. \tag{3.12}$$

$\mathcal{P}(\omega),\mathcal{R}(\omega)$ and $\mathcal{P}(t),\mathcal{R}(t)$ are linked by Fourier transform in time/energy:

$$\mathcal{P}(\omega) = \frac{1}{2\pi}\int_{-\infty}^{+\infty} dt e^{-i\omega t}\mathcal{P}(t); \quad \mathcal{R}(\omega) = \frac{1}{2\pi}\int_{-\infty}^{+\infty} dt e^{-i\omega t}\mathcal{R}(t). \tag{3.13}$$

$n_\omega = \left[e^{\hbar\omega/k_BT} - 1\right]^{-1}$ is the Bose-Einstein distribution and $\otimes$ stands for the convolution product. In order to account for the finite energy resolution $R(\omega)$ of the spectrometer by a convolution, an instrumental transfer function can be easily introduced before the back Fourier transform in Eq. 3.11 ($\mathcal{R}(t)$-term). A gaussian energy point spread function was systematically used for simulations.
The EELS spectrum $P(\omega)$ appears as the multiple convolution of the single gain-loss function $\mathcal{P}(\omega)$ which generates not only multiple losses from a given transition but also combination features between different transitions and also gain peaks at finite temperature. The series of multiple losses follows a Poisson statistics (Eq. 3.11) as checked experimentally in the early work of H. Ibach [64]. In Fourier space (time space here), the summation appears as a simple exponential term. Therefore, to clarify the readings of experimental spectra, Eq. 3.11 has inspired a multiple losses removal algorithm [98] to recover only the single loss term $\mathcal{P}(\omega)$ from $P(\omega)$. The method is based on the logarithm of the Fourier transform of the experimental spectrum and of an estimate of $\mathcal{R}(t)$ from the elastic peak. It turned out to be very convenient in the identification of vibrational modes hidden by intense multiple phonon losses in the case of oxides (see for example Ref. [92] for hydroxyls group on TiO_2(110)). Since the ratio between losses and gains (or Stokes and anti-Stokes transitions) is given simply by the Boltzmann factor [61], the surface temperature over the EELS probing depth (see Sect. 3.2.5) can be easily determined experimentally. Finally, the $\mathbf{k}_\parallel$ integration over the domain D of the scattering cross section is restricted herein to one-quantum loss process as usually done *i.e.* to $P_{cl}(\mathbf{k}_I, \omega)$ in Eq. 3.12 (see Sect. 3.2.1.2) and not to the multiple excitation cross section $P(\omega)$ (Eq. 3.11) as it should be [84]. But, beyond the obvious heaviness of the calculations, the underlying approximation is usually hidden by the experimental uncertainties as shown in Ref. [84].

3.2.2 The dielectric function of TiO_2 from far-infrared to ultraviolet

The modelling of the energy loss spectrum of TiO_2 over a large spectral range (up to 6 eV herein) requires a dielectric function which reproduces accurately the involved elementary solid-state excitations. Since the crystallographic structure of TiO_2 rutile is tetragonal, the dielectric tensor is diagonal with two main components $\epsilon_\parallel(\omega)$ and $\epsilon_\perp(\omega)$ along the direction parallel or perpendicular to the [001] c-axis. These quantities have been decomposed into a phonon $\epsilon_{Ph}(\omega)$, a band-to-band transition $\epsilon_{Ib}(\omega)$, a band gap state $\epsilon_{gs}(\omega)$ and a Drude-like $\epsilon_{Pl}(\omega)$ contributions:

$$\epsilon_{TiO_2}(\omega) = \epsilon_{Ph}(\omega) + \epsilon_{Ib}(\omega) + \epsilon_{gs}(\omega) + \epsilon_{Pl}(\omega). \tag{3.14}$$

$\epsilon_{gs}(\omega)$ and $\epsilon_{Pl}(\omega)$ are defect-related and appear only in reduced TiO_2. If not stated specifically, the labels $\parallel, \perp$ are assumed to be implicit hereafter. All theses quantities are presented in Fig. 3.8 and are discussed one after the others in what follows. Only dipolar EELS simulations are carried out herein and non local effects that is to say any $k_\parallel$-dependence of $\epsilon_{TiO_2}(\omega)$ are discarded hereafter.

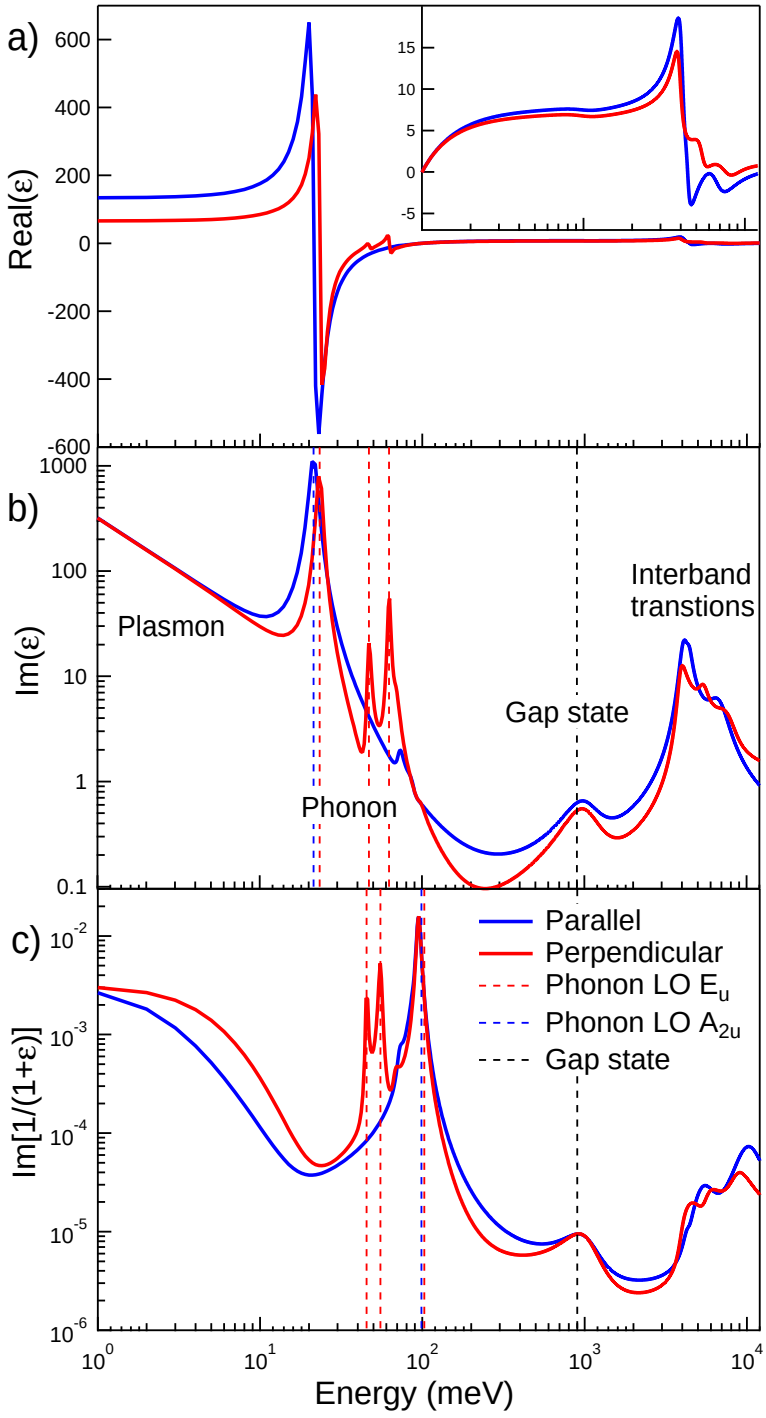

Figure 3.8: a) Real and b) imaginary part of the TiO_2 dielectric functions $\epsilon_{\parallel}(\omega)$ (blue line), $\epsilon_{\perp}(\omega)$ (red line) (Eq. 3.14). c) Corresponding loss function $\mathrm{Im}[1/1+\epsilon(\omega)]$. The inset in figure-a shows a zoom of $\mathrm{Re}[\epsilon(\omega)]$ over the $0.1-12$ eV range. Vertical dotted lines pinpoint the frequencies of transverse ω_{TO} and longitudinal ω_{LO} phonons of bulk TiO_2 used in $\epsilon_{Ph}(\omega)$ (Eq. 3.15). ($\hbar\omega_p = 80$ meV; $\hbar\Gamma_P = 20$ meV), ($\hbar\omega_{gs} = 1000$ meV; $\hbar\Gamma_{gs} = 600$ meV; $\hbar\Omega_{gs} = 500$ meV) have been used to describe respectively the Drude (Eq. 3.19) and band gap state (Eq. 3.18) contributions while the phonon and interband transition counterparts are extracted from Ref. [114] and Ref. [115].

3.2.2.1 Phonons

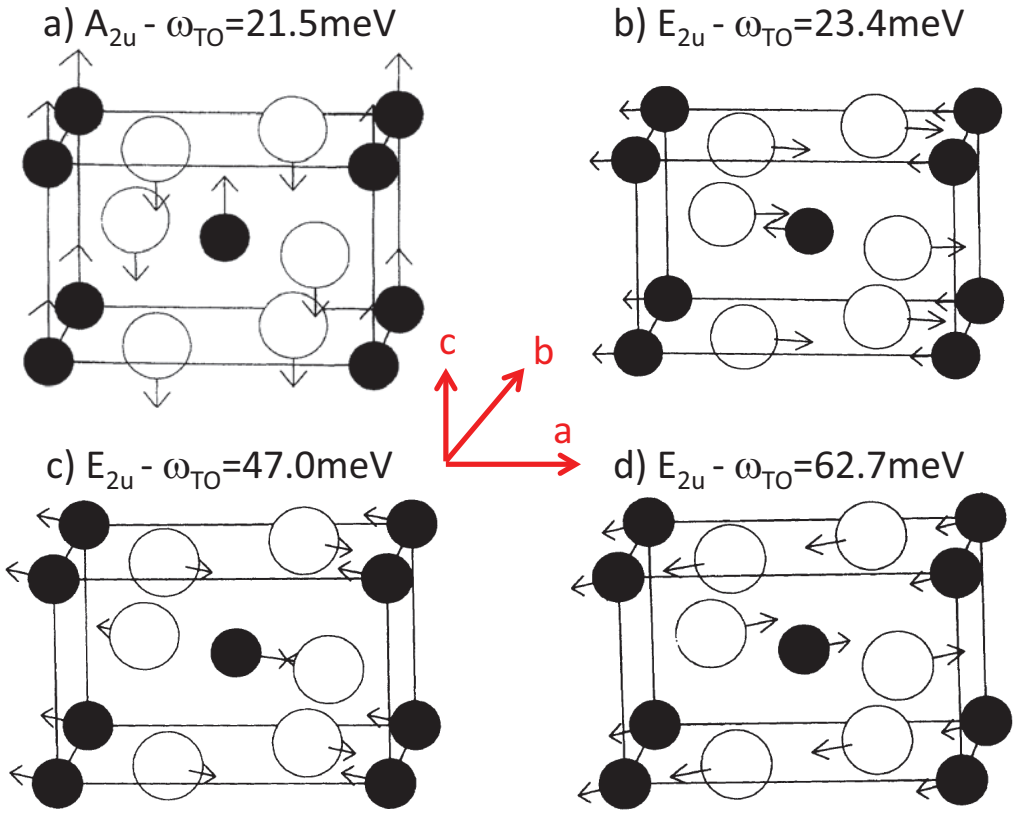

Figure 3.9: Atomic displacements associated to the infrared active mode in TiO_2 rutile. Black and white balls denote Ti and O atoms respectively. Adapted from Ref. [116].

As suggested in the initial infrared reflectivity analysis of F. Gervais and B. Piriou [29, 117, 118] and as renewed in depth in the accurate and detailed mid-infrared and far-infrared ellipsometric measurements of D. Schöche *et al.* [114], the contribution of infrared active optical phonons is described through a factorized model:

$$\epsilon_{Ph}(\omega) = \epsilon_{Ph,\infty} \prod_n \frac{\omega_{LO,n}^2 - \omega^2 - i\Gamma_{LO,n}\omega}{\omega_{TO,n}^2 - \omega^2 - i\Gamma_{TO,n}\omega}. \tag{3.15}$$

ω_{LO}, ω_{TO} and Γ_{LO}, Γ_{TO} stand for the frequencies and dampings of the longitudinal and transverse phonon modes at the center of the Brillouin zone. $\epsilon_{Ph,\infty}$ is the dielectric function at frequencies much higher than the phonon ones that is to say *i.e.* in the optical domain. Parameters extracted from Ref [114] can be found in Tab. 3.1; the work of Ref. [114] matches perfectly with all the previous determinations of the phonon modes in rutile, in particular the optical ones [117, 119], neutron scattering [120] and *ab initio* modelling [116, 121, 122]. It is worth noticing that this infrared ellipsometry analysis was performed on stoichiometric non reduced TiO_2 samples [5] of various orientations (001) (110) and (111). The group

[5] Private communication from the authors.

theory decomposition in irreducible representation of TiO_2 rutile phonons [21, 116, 120, 123] (point group D^1_{4h} or $P4/mmm$) : $\Gamma = A_{1g} + A_{2g} + A_{2u} + B_{1g} + B_{2g} + 2B_{1u} + E_g + 3E_u$ shows that only four modes ($A_{2u} + 3E_u$) have infrared (and therefore an EELS) dipole activity with longitudinal/transverse splitting. E_u modes are doubly degenerated. Therefore, the summation in Eq. 3.15 extends over $n_\perp = 3\,E_u$ and $n_\parallel = 1\,A_{2u}$ modes along the direction parallel and perpendicular to the c-axis. Their vibrational patterns are illustrated in Fig. 3.9. The factorized form of $\epsilon(\omega)$ was preferred over the classical summation of

a) Direction	phonon	$\hbar\omega_{TO}$ (meV)	$\hbar\Gamma_{TO}$ (meV)	$\hbar\omega_{LO}$ (meV)	$\hbar\Gamma_{LO}$ (meV)	$\hbar\Omega_{ph}$ (meV)	$\epsilon_{\infty,Ph}$
$\perp$	E_u	23.38	1.82	45.34	1.09	204.90	5.96
$\perp$	E_u	47.03	2.39	55.16	2.28	49.98	
$\perp$	E_u	62.67	2.77	102.86	5.44	87.68	
$\parallel$	A_{2u}	21.47	2.48	98.75	5.75	265.90	7.16
$\perp$	n.a.	68.93	8.02	68.07	7.17		
$\perp$	n.a.	96.83	9.56	96.71	8.73		
$\parallel$	n.a.	72.78	6.97	72.41	6.45		
$\parallel$	n.a.	88.03	8.52	87.90	9.29		

b) Direction	$\hbar C$ (meV$^\mu$) $\times 10^{-3}$	Φ (deg)	$\hbar\omega$ (meV)	$\hbar\Gamma$ (meV)	μ	$\epsilon_{\infty,Ib}$
$\parallel$	2.5	0	4.09	0.28	0.8	-5.26
$\parallel$	0.37	0	4.41	0.18	0.7	
$\parallel$	5.2	0	6.63	1.15	1.0	
$\perp$	0.28	0	3.92	0.21	0.5	-6.86
$\perp$	1.4	0	5.41	0.44	1.0	
$\perp$	19.3	0	7.52	1.46	1.3	

c) Direction	$\omega_{sph,1}$ (meV)	$\omega_{sph,2}$ (meV)	$\omega_{sph,3}$ (meV)
$\mathrm{Im}\,[1/(1+\epsilon_\perp]$	45.3	54.6	95.4
$\mathrm{Im}\left[1/(1+\sqrt{\epsilon_\parallel\epsilon_\perp}\right]$	45.6	55.4	93.8

Table 3.1: a) Parameters of the factorized dielectric function $\epsilon_{Ph}(\omega)$ of the infrared active optical phonons $3E_u + A_{2u}$ (from Ref. [114]). Values of symmetry forbidden minor modes found in Ref. [114] are given below. Error bars on the frequencies and damping are below 0.1 meV and 0.6 meV on average for the symmetry allowed modes and below 1.6 meV and 0.6 meV for the additional ones. The corresponding oscillator strenghts Ω_{ph} (see Eq. 3.22) of Ref. [119] are also given as well as the prefactor $\epsilon_{\infty,Ph}$. The static values are: $\epsilon_\parallel(0) = 152.97$ and $\epsilon_\perp(0) = 84.69$. b) Critial point transition parameters used in the fit of the UV-visible part of the dielectric function $\epsilon_{Ib}(\omega)$ of Ref. [115]. Negative values for $\epsilon_{\infty,Ib}$ are counterbalanced by $\epsilon_{\infty,Ph}$ at $\omega \to +\infty$. c) Positions of the surface phonon modes as given by the maxima of the loss function (Fig. 3.10).

damped oscillators [21, 119] which does not allow independent broadenings of transverse and longitudinal phonons and asymmetric shapes as observed in ionic crystal with several modes having large TO-LO splitting [114, 117, 118]. Furthermore, it explicitly shows the value of the longitudinal phonon frequencies probed in transmission EELS as the poles of $1/\epsilon_{Ph}(\omega)$ (see Sect. 3.2.1 and Fig. 3.10). In reflection EELS, the resonances appear as the maxima of (i) $\mathrm{Im}\,[1/(1+\epsilon_{\perp,Ph}(\omega)]$ at $\hbar\omega_{sph,1} = 45.3$ meV, $\hbar\omega_{sph,2} = 54.6$ meV, $\hbar\omega_{sph,3} = 95.4$ meV for

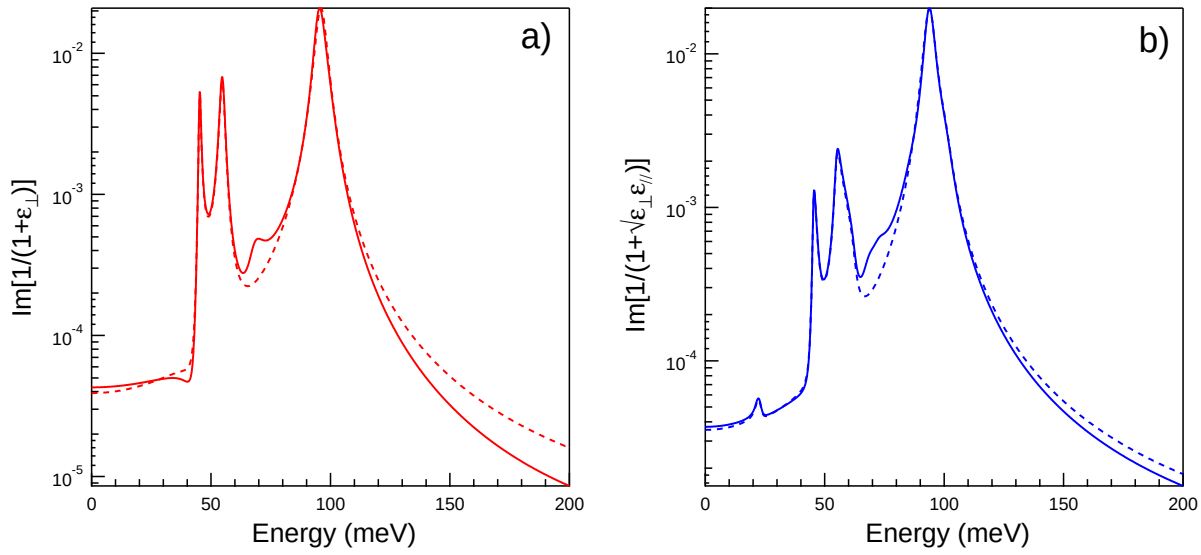

Figure 3.10: Phonon loss functions perpendicular a) $\mathrm{Im}\left[\frac{1}{1+\epsilon_\perp(\omega)}\right]$ and parallel b) $\mathrm{Im}\left[\frac{1}{1+\sqrt{\epsilon_\parallel(\omega)\epsilon_\perp(\omega)}}\right]$ to the c-axis with (full lines) and without (dotted lines) additional symmetry forbidden modes.

an incident plane perpendicular to the c-axis and (ii) of $\mathrm{Im}\left[1/(1+\sqrt{\epsilon_{\parallel,Ph}(\omega)\epsilon_{\perp,Ph}(\omega)}\right]$ at $\hbar\omega_{sph,1} = 45.6$ meV, $\hbar\omega_{sph,2} = 55.4$ meV, $\hbar\omega_{sph,3} = 93.8$ meV for an incident plane parallel to the c-axis (see Sect. 3.2.4.1 for a discussion on anisotropy). These excitations are known as the Fuchs-Kliewer modes [61] and were detected in HREELS for the first time on ZnO by H. Ibach [64]. As noticed in the initial HREELS study of $TiO_2(110)$ [21, 90], the accidental degeneracy of $A_{2u,\parallel}$ and $E_{u,\perp}$ leads to similar surface phonon frequencies for the two main beam orientations. D. Schöche *et al.* as well as F. Gervais and B. Piriou [117] found also four symmetry forbidden additional modes of lower oscillator strengths, two along each direction. They correspond to maxima in the phonon density of states and are probably activated by bulk defects through folding of Brillouin zone. For completeness, they were accounted for in the present study as they lead to slight shits of the main phonon frequencies (Fig. 3.10).

3.2.2.2 Interband transitions

The valence band of TiO_2 rutile is dominated by $O-sp$ states while the conduction band is derived from strongly localized $Ti-3d$ states. The material displays a direct $\Gamma-$point band gap of around 3.1-3.2 eV [122, 124, 125]. The UV-visible contribution to the dielectric function $\epsilon_{Ib}(\omega)$, in particular the part of interband transitions, was extracted from the well-known compilation of E. D. Palik [115]. For the sake of EELS spectra simulation, it was parametrized and fitted using the critical point transition approach [126] with the formula:

$$\epsilon_{Ib}(\omega) = \epsilon_{Ib,\infty} + \sum_m \left\{ \frac{C_m e^{i\Phi_m}}{(\omega_m - \omega - i\Gamma_m)^{\mu_m}} + \frac{C_m e^{-i\Phi_m}}{(\omega_m + \omega + i\Gamma_m)^{\mu_m}} \right\}. \tag{3.16}$$

$C_m, \Phi_m, \mu_m, \omega_m, \Gamma_m$ are respectively the amplitude, the phase, the pole order, the frequency and the damping of the m^{th} critical point while $\epsilon_{Ib,\infty}$ is the remaining high frequency dielectric function. Compared to the standard oscillator description [127], the above representation allows to account for (i) transition between band pairs with a substantial integration over k-space and therefore apparent broadening larger than intrinsic linewidth and (ii) functional dependence other than simple poles. A satisfactorily fit in the $0.6 - 12$ eV range of data of Ref. [115] (Fig. 3.11) was achieved with only three transition points along the parallel and perpendicular direction and zero phases (Fig. 3.8). Data were carefully matched to the $\epsilon_{Ph}(\omega)$ value extracted from Ref. [114].

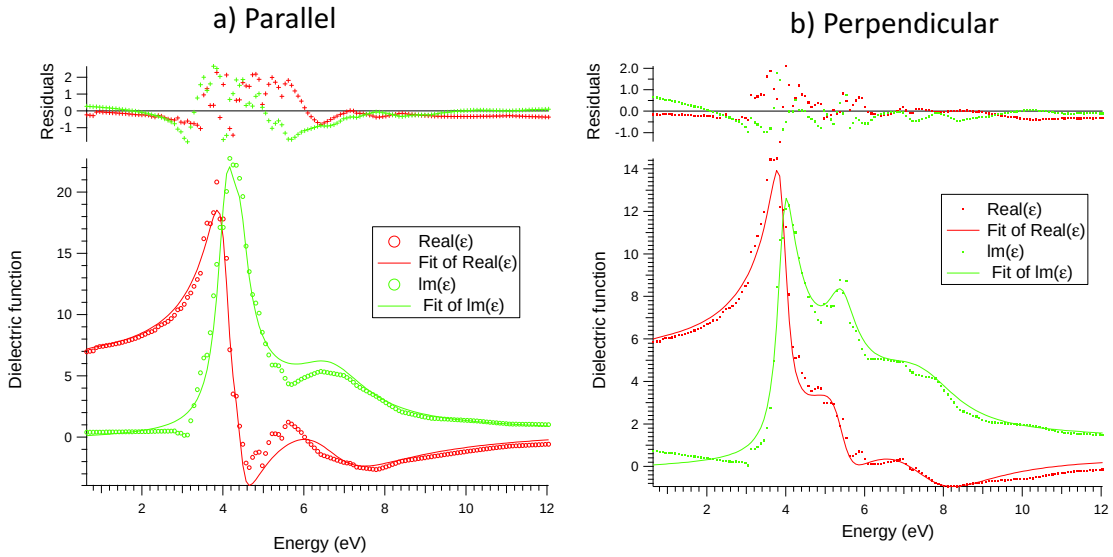

Figure 3.11: Fit with Eq. 3.16 of the UV-visible dielectric functions of TiO_2-rutile from database of Ref. [115]: a) $\epsilon_{\parallel,Ib}(\omega)$ b) $\epsilon_{\perp,Ib}(\omega)$. The analysis was performed with three critical transition points (Eq. 3.16) (see text).

3.2.2.3 The static dielectric function: electron-phonon coupling and polaronic distorsion

All phonon modes in rutile exhibit a large longitudinal/transverse splitting (Tab. 3.1) which induces a large value of the static dielectric constant through the Lyddanne-Sachs-Teller relation [128]:

$$\epsilon(0) = \epsilon_{Ph,\infty} \prod_n \frac{\omega_{LO,n}^2}{\omega_{TO,n}^2}. \tag{3.17}$$

The found values $\epsilon_{\parallel}(0) = 152.97$ and $\epsilon_{\perp}(0) = 84.69$ [114,117] matches with the determination from capacitance measurements [129]. Those high values demonstrate the importance of the electron-phonon coupling that is at the origin of polaronic behaviour of excess electrons.

As a matter of comparison, that of ZnO wurtzite or Si is one order of magnitude lower ($\epsilon_{ZnO}(0) = 8.7$, $\epsilon_{Si}(0) = 11.7$).

3.2.2.4 Defects induced band gap states and optical absorption

In bulk reduced TiO_2, fingerprints of the so-called band gap states (BGS) due to defects (mainly oxygen vacancies and Ti-interstitials) have been detected with various spectroscopies [2–9]. It appears at an energy around 0.8-1 eV below the Fermi level in photoemission spectroscopy [10, 12, 130] or in Auger transition involving the valence band [20], as an electron energy loss of c.a. 1 eV [21, 131], as a peak of density of states in scanning tunneling spectroscopy [15, 22] or as near infrared optical absorption peak [132, 133]. Its bulk versus surface nature is still highly debated [12–14, 55, 58] when probed with surface sensitive techniques as well as the degree of localisation of the associated charges [22, 34, 52, 53] *i.e.* the radius of the polaron (small versus large polaron or even free-electron like behaviour). These two points will be the topics of the next chapters.

The BGS is simply the signature of the optical absorption from a polaronic state due defect-related excess electrons. With the absorption of a photon of appropriate energy, a self-trapped carrier can be freed from the potential well that traps it. Since the motions of the atoms that produce the trapping potential well are slower than the photoionization process, the self-trapping potential well is treated as fixed during the photoionization process. This is particularly true in the case of photoemission as shown in Ref. [28] and explains the sizeable difference between thermal activation energy and optical transition energy for excess electrons (see discussion Sect. 5.1). The line shape of the absorption is the topic of intense theoretical modelling depending on the degree of electron-phonon coupling, the temperature or even the dimensionality of space (see reviews. [134,135] and cited references). Two extreme cases can be distinguished [136]. In the case of a large polaron, the photo-ionization occurs from the hydrogenoic ground state of the potential well to a continuum unbound states of free carrier type. The absorption coefficient scales as $\alpha \sim (kR)^3/\omega[1 + (kR)^2]^4$ where $\hbar k = \sqrt{2m(\hbar\omega - 3E_p)}$ is the free-carrier wave vector and R the radius of the polaron; it is a peaked asymmetric function that starts above three times the polaron binding energy E_p (Fig. 3.12-a). At variance, for a small polaron, the self-trapped carrier is excited from its localized state to an adjacent site; the transition is strongly driven by thermal broadening of levels. The absorption coefficient $\alpha \sim \exp[-(2E_b - \hbar\omega)^2/\Delta^2]/\omega$ depends on the small polaron binding energy E_b and the thermal broadening Δ of levels. It shows a gaussian line shape with an asymmetry on the high energy side (Fig. 3.12-b) and a strong temperature dependence in contrast to the large polaron model. Although the published work about optical absorption in rutile seems to favour the small polaron model [132, 137], the situation is far from being settled. An accurate description of the BGS lineshape is far beyond the scope of the present study since the question overlaps with the problems of relative surface/bulk contributions and of defect disorder induced broadening. Therefore, for the sake of simplicity, BGS optical absorption are described herein with a simple oscillator model:

$$\epsilon_{gs}(\omega) = \frac{\Omega_{gs}^2}{\omega_{gs}^2 - \omega^2 - i\Gamma_{gs}\omega}, \tag{3.18}$$

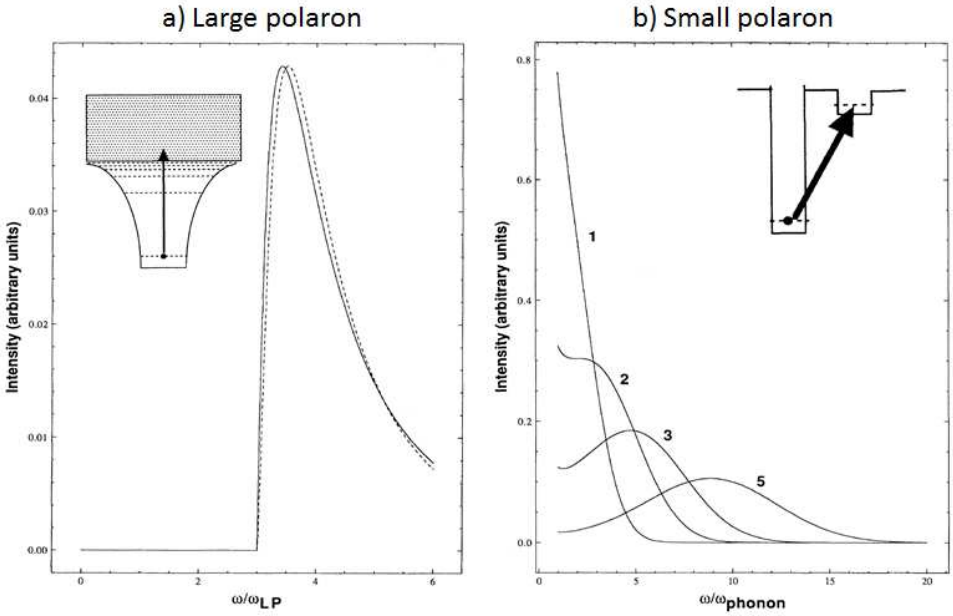

Figure 3.12: Optical absorption profile per polaron in the case of: a) a large polaron where the peak starts at $3E_p$, and b) a small polaron as a function of its binding energy normalized by the phonon frequency E_b/ω_{ph}. At large electron-lattice coupling, the curve peaks at $2E_b$ (see text). The insets schematically illustrate the transitions for both cases. Adapted from Ref. [136]

where ω_{gs}, Γ_{gs}, Ω_{gs} are respectively its frequency, damping and oscillator strength. It is supposed to grasp most of the physics of screening discussed hereafter.

3.2.2.5 Excitation due to itinerant motion of carriers: the Drude model

Reduced rutile is indubitably a $n-$type semiconductor which transport properties have been the topics of numerous studies [25,30,31]. But the precise nature of the transport is not clearly settled, in particular the puzzling question of the large mobility [22, 27] at low temperature, not speaking about the nature of dominating defects (oxygen vacancies and/or titanium interstitials) at its origin. Is it due to a dual behavior of excess electrons or to the coexistence of trapped and free states giving rise to BGS and conductivity [22, 27] ?
Because of the strong electron-phonon coupling in this material, transport is often described in terms of polarons, a quasiparticle made of an electron and the accompanying phonon cloud due to lattice distortions. But the polaronic spatial extension which impacts the type of conductivity is still under debate [22, 27, 29]. In the strong coupling case, electrons self trap in the form of small polarons and the transport of these highly localized charges occurs through thermally activated hopping from one site to the other. Large polarons with spatially extended wavefunctions are formed if the coupling is weaker and exhibit a band-type transport behavior but with an enhanced effective mass compared to the rigid lattice. Whatever its type, the ability of a polaron to move coherently in an alternative field is always restricted as it can only move in response to the atomic motion. But, a polaron can have a Drude-like

carrier absorption [134–136] at low frequency if its moves itinerantly with a mean free path greater than the inter-site separation. For a large polaron, the Drude-like behaviour occurs only at frequencies below the characteristic phonon frequency involved in the trapping. For a small polaron, the condition is even more stringent. The extremely narrow bands that characterize small polaronic carriers may preclude itinerant(coherent)small-polaron motion in all but the most idealized conditions [136].

The carrier excitations and therefore the conductivity at low frequency are described in this work through a classical Drude formula:

$$\epsilon_{Pl}(\omega) = -\frac{\omega_P^2}{\omega^2 + i\omega\Gamma_P} \quad \text{with} \quad \omega_P^2 = \frac{ne^2}{m_e m^* \epsilon_0}, \tag{3.19}$$

where the plasma frequency ω_P is given in terms of the carrier density n and their effective polaronic mass m^*, (e, m_e, ϵ_0) being respectively the elementary electric charge, the electron rest mass and the vacuum permittivity. The damping Γ_P is related to the carrier mobility μ through $\Gamma_P = e/(m_e m^* \mu)$. The Drude model is the first level description of the frequency dependent (or optical) conductivity $\sigma(\omega)$ through a collision relaxation time [128]. It will be shown, in particular in Chap. 5, that this description of conductivity is able to describe satisfactorily our EELS results. J. F. Baumard and F. Gervais [29, 111] demonstrated that this Drude term correctly fits the infrared reflectivity behaviour in heavily reduced samples TiO_{2-x} ($x \simeq 0.001 - 0.05$) over a large frequency range (25-375 meV) well above the transverse optical frequency of phonon (see Tab. 3.1). They found that plasmons couple to longitudinal phonon modes and that ω_P^2 depends linearly on reduction level x. Through temperature dependent measurements, they concluded that the activation of carriers to the conduction band constitutes the essential feature of the electrical conductivity. Frequency-dependent conductivity below the THz (4 meV) were also successfully interpreted with the Drude approach for optically created carriers [32, 138] as well as for hydrogen doping [139] at low temperature. E. Hendry *et al.* [32, 138] concluded that transport occurs through a polaron in the intermediate regime, neither large nor small with a strong anisotropy of effective mass and electron mobility.

3.2.3 Numerical implementation: the *HREELS* program

All the above mentioned theoretical framework of the semi-classical dielectric theory has been implemented in a dedicated program called *HREELS* written in Fortran 90 by R. Lazzari; it has enhanced potentialities compared to Ref. [140]. As described in Sect. 3.2.2 in the case of TiO_2, the dielectric function of the material is parametrized as a sum of various excitations (phonon, plasmon, interband transitions; see Eq. 3.14). Phonon dielectric function can be described in the factorized form (Eq. 3.15) or as a sum of oscillators. Losses from a uniaxial material with its main axis parallel/perpendicular to the incident plane or normal to the surface (Eq. 3.5) can be handled in the form of a multilayer (up to 8 layers). Calculations can be performed up to n^{th} losses by using the expansion of Eq. 3.11. Fast-Fourier transform is therefore employed with a careful data oversampling. The apparatus point spread function is described as the convolution of various functions (gaussian, lorentzian, etc.. . .). The integration over the beam divergence (Eqs. 3.1-3.2) can performed (i) either fully numerically

over circular, ellipsoidal or rectangular slits or (ii) in polar coordinates only for circular slits through one-dimensional radial integral [81]. Particle trajectory and therefore loss function can be corrected from the interaction of the incoming charge with its image [83], a minor effect for the incident angle of this study. Beyond simulations, data fitting can be performed through Levenberg-Marquardt χ^2-minimization either in linear or logarithmic scale by including or not the quasi-elastic.
Alongside basic data treatments (temperature determination from Boltzman statistics applied to gain/loss peaks, plot of sensitivity and dielectric functions, estimate of probing depth, smoothing, filtering, etc...), multiple excitation removal accordinlgy to Ref. [98] is available; the apparatus function is estimated in this case through an asymmetric Voigt fit of the quasi-elastic accounting (or not) for the existence of lorentzian excitations (typically plasmon). The tool is complemented by the resolution enhancement option based on the semi-blind Lucy-Richardson algorithm as described in depth in Sect. 3.3; the starting apparatus function is either gaussian, lorentzian or given the quasi-elastic peak itself; constraints and smoothing can be applied with a full control of the loop flow in the process.

3.2.4 The interplay and screening between reduced TiO_2 excitations

If not stated afterwards, the following simulation parameters have been used throughout this theoretical study: beam energy $E_I = 8$ eV ($E_I = 38$ eV for EELS), incident angle $\Theta_I = 60°$, circular detection slit $\theta_C = 1°$, gaussian shape for the apparatus resolution function with a Full-Width at Half-Maximum (FWHM) of $\Delta_a = 8$ meV ($\Delta_a = 50$ meV for EELS), temperature $T = 300$ K. For most simulations, no gradient of dielectric function has been accounted for and the beam was assumed to be perpendicular to the c-axis *i.e.* the effective dielectric function is $\xi(\mathbf{k}_\parallel, \omega) = \epsilon_\perp(\omega)$. In passing, a great care has been taken in the sampling of the numerical integration of Eq. 3.11 [140] which may be screwed for low plasmon energies or damping by numerical issues. Fast Fourier transform was used with an energy step down to $\Delta\hbar\omega = 10^{-4}$ meV.

3.2.4.1 Effect of dielectric anisotropy

Figure 3.13 shows simulated spectra in high-resolution (Fig. 3.13-a) and low-resolution modes (Fig. 3.13-b) for (i) the two main orientations of the c-axis, perpendicular $\xi(\omega) = \epsilon_\perp(\omega)$ or parallel $\xi(\omega) = \sqrt{\epsilon_\parallel(\omega)\epsilon_\perp(\omega)})$ to the incident plane or (ii) for a fictitious material having a effective dielectric function equal to $\xi(\omega) = \epsilon_\parallel(\omega)$.

When the c-axis is perpendicular to the incident plane, the loss spectrum contains only contributions from the E_u-modes and the high energy surface phonon $\omega_{sph,3} = 95.6$ meV falls just below the longitudinal E_u phonon at $\omega_{LO} = 102.9$ meV. The fictitious spectra with $\epsilon_\parallel(\omega)$ is dominated by the A_{2u} mode with a surface peak at $\omega_{sph,\parallel} = 92.4$ meV. When the c-axis is parallel to the incident beam, the symmetry assignment is less rigorous since $\xi(\omega) = \sqrt{\epsilon_\parallel(\omega)\epsilon_\perp(\omega)}$, but the low energy peaks are clearly of E_u-type while the high energy one at $\omega_{sph,3} = 93.9$ meV is of composite character between the high energy E_u and A_{2u} longitudinal modes. The introduction of this latter results also in a screening of the low energy E_u surface modes which are much weaker in intensity than along the other orientation.

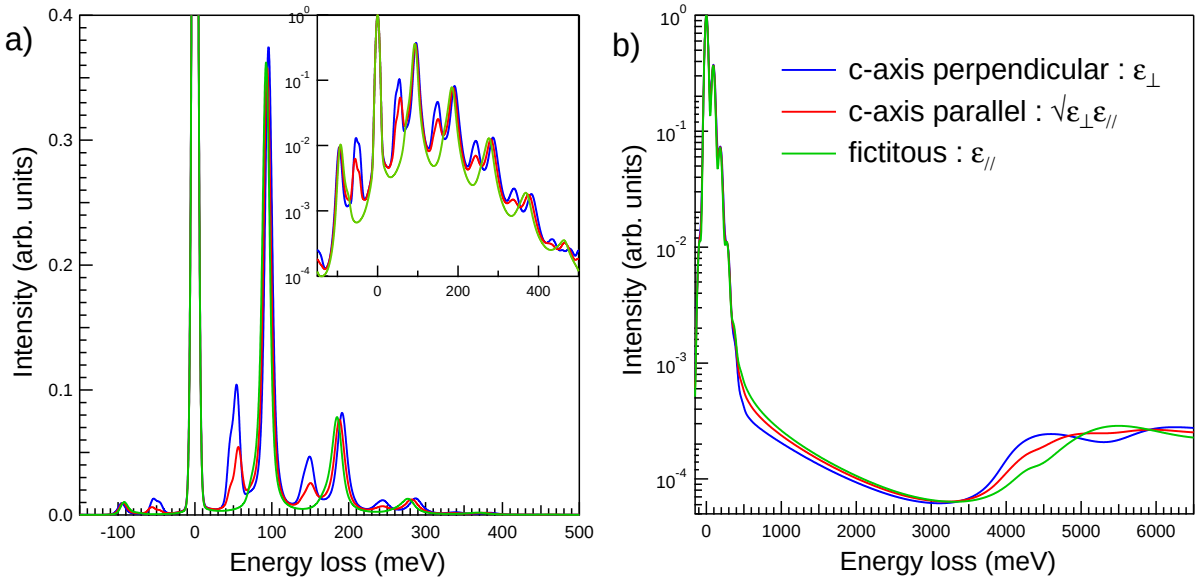

Figure 3.13: Effect of the uniaxial anisotropy of TiO_2 on simulated a) HREELS ($E_I = 8$ eV; $\Delta_a = 8$ meV) phonon spectrum, and b) EELS ($E_I = 38$ eV; $\Delta_a = 50$ meV) interband transitions. Blue line: c-axis perpendicular to beam; red line: c-axis perpendicular to beam; green line: fictitious material having an $\epsilon_{||}$ dielectric function. Spectra have been normalized to the elastic peak intensity and no defect related feature has been accounted for. The inset of Fig. a shows the spectrum on a logarithmic scale.

However, as already noticed in Ref. [21,90], due to the fortuitous degeneracy of the high energy A_{2u} and E_u longitudinal modes, the differences between the two main c-axis orientations are minor for the high energy surface phonon $\omega_{sph,3}$. Therefore, all the following discussion and data analysis on phonon shift will be restricted to $\xi(\omega) = \epsilon_\perp(\omega)$ situation. However, since spectra are structured by complex multiple and combination losses [35, 89], tiny shifts and differences are amplified in the high order excitations making them easier to detect despite a modest experimental resolution (inset of Fig. 3.13-a). Regarding the EELS spectra (Fig. 3.13-b), the various orientations distinguish mainly through the shape of the interband transitions; the $\epsilon_\perp(\omega)$-orientation offers the lowest background at the location of the BGS.

3.2.4.2 Quasi-elastic peak broadening due to carriers

When low frequency conductivity is described through a Drude term $\epsilon(\omega) = \epsilon(0) - \omega_P^2/(\omega^2 + i\omega\Gamma_P)$ (Eq. 3.19), the classical loss function which reads:

$$G(\omega) = \mathrm{Im}\left[-\frac{1}{1+\epsilon_{Pl}(\omega)}\right] = \frac{1}{1+\epsilon(0)}\frac{\Gamma_P\omega_{sp}^2\omega}{\left[\omega_{sp}^2-\omega^2\right]^2+\Gamma_P^2\omega^2} \tag{3.20}$$

has a nearly lorentzian shape close to the so-called surface plasmon frequency $\omega_{sp} = \omega_P/\sqrt{1+\epsilon(0)}$. These excitations are coherent delocalized electron oscillations that exist at the interface between materials (vacuum/solid here) and are the electronic equivalent of surface phonons [61,

141]. In the case of doped semiconductors, depending on the carrier concentration, the signature of conductivity in EELS appears either as a isolated peak or as a broadening of the elastic peak due to multiple $\omega_{sp}-$excitations [61, 103]. The coupling to the incident electrons may so intense that the peak is better named "quasi-elastic" as nearly all reflected electrons suffer from energy loss. As an incipient ferroelectric compound, TiO_2 possesses a very high static dielectric function $\epsilon(0)$ ($\epsilon_{\|}(0) = 153, \epsilon_{\perp}(0) = 84.7$, see Sect. 3.2.2) at variance to others doped semiconductors ($\epsilon_{ZnO}(0) = 8.7$, $\epsilon_{Si}(0) = 11.7$) which surface plasmon excitation and accumulation/depletion layers have been quite studied by EELS [97,100–110]. In addition, the polaronic nature of the electronic transport leads to an effective mass of $m^* = 8 - 10$ [25, 29, 32], much higher than that estimated by *ab initio* band-structure calculations for rigid-lattice ($m^*_{\perp} = 1.1, m^*_{\perp} = 0.57$ [122] [6].) The combination of both effects yields to a $\omega_{sp} \sim 1/\sqrt{m^*}\sqrt{1+\epsilon(0)}$-value two orders of magnitude lower than for classical semiconductors at a given carrier concentration n (see top scales of Fig. 3.14).

Starting from a t-expansion of the Poisson distribution of multiple losses (Eq. 3.11), B. N. J Personn and J. E. Demuth [103] derived an elegant analytic formula for the variance of the broadening of the elastic peak due to bulk free carriers described by a Drude term:

$$\Delta_n^2 = \frac{C}{4}\pi^2\omega_{sp}^2\left[\frac{2}{e^{\hbar\omega_{sp}/k_BT}-1}+1\right] \text{ with } \quad C = \frac{4}{\pi}\frac{1}{\epsilon(0)+1}\frac{1}{\cos^2\Theta_I}\frac{1}{k_I a_0}, \tag{3.21}$$

where $a_0 = 4\pi\epsilon_0\hbar^2/me^2$ is the Bohr radius and the other parameters have been previously defined. By adding an apparatus function Δ_a^2 , the evolution of the quasi-elastic FWHM (FWHM $= 2\sqrt{2\ln 2}\sqrt{\Delta_n^2+\Delta_a^2}$) can be obtained either as a function of carrier concentration at fixed temperature (Fig. 3.14-a, dotted line) or vice-versa (Fig. 3.15, dotted lines). For instance, Eq. 3.21 has been used to determine ionization energy of hydrogen doped zinc oxide [97] from the temperature dependence of the quasi-elastic peak broadening. But the comparison between TiO_2 and ZnO (see Fig. 3.16 vs Fig. 3.14-3.15) shows that rutile elastic peak is much less sensitive to broadening; this difference mainly stems from the value of static dielectric function in the two materials which results in a much smaller ω_{sp} in TiO_2 than in ZnO for the same bulk plasma frequency. Starting from reasonable values of the carrier concentration after vacuum annealing [3, 29, 142] in the range of $n = 10^{18-19}$ cm^{-3} and of the effective mass $m^* \simeq 10$ [25, 32], a visible temperature dependence is expected from Eq. 3.21 for rutile (Fig. 3.14-a, red and violet dotted line).

Although useful to pinpoint the main phenomena, strictly speaking the approach of Personn and Demuth is valid only for infinitesimal Γ_P and ω_{sp}, a fact which is not overlooked in the analysis of Ref. [97]. Full numerical simulations of the elastic peak shape have therefore been carried out to identify the effect of carrier damping Γ_P. As shown in Fig. 3.14, increasing Γ_P at fixed carrier density n/m^* surprisingly sharpens the quasi-elastic peak down to the resolution function. In a similar way to in the analytic formula of Personn and Demuth (Eq. 3.21), a progressive broadening of the quasi-elastic is observed upon increasing the carrier concentration up to a turn over point at which the surface plasmon frequency ω_{sp} is high enough to generate an isolated single excitation (Fig. 3.17-a). This latter appears as a side shoulder of the elastic peak which can even mix with phonon excitation to generate the so-

[6] Those values are close to $m^*_{\mathrm{Si}} = 1.08$ or $m^*_{\mathrm{ZnO}} = 0.3$.

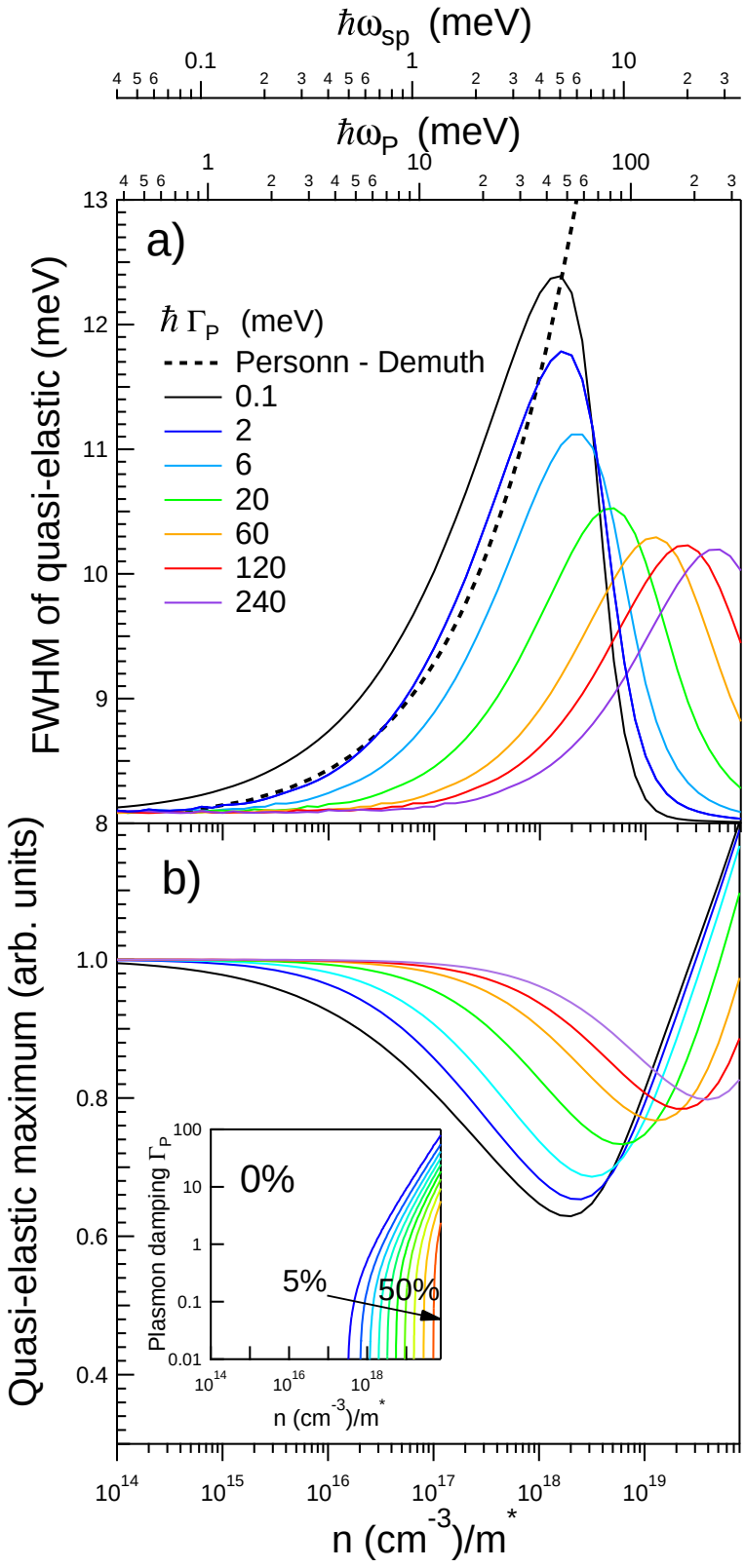

Figure 3.14: a) FWHM and b) maximum of the quasi-elastic peak at $T = 300$ K as obtained from a simulated spectrum including multiple excitations (Eq. 3.11). Quantities are plotted as a function of (i) carrier density n normalized by the effective mass m^* (bottom scale) or (ii) the bulk plasmon ω_P or surface plasmon ω_{sp} frequency (top scales) for various carrier plasmon dampings Γ_P. The comparison with the analytic formula Eq. 3.21 (dotted black line) is added for completeness in Fig. a. The inset of Fig. b shows the fraction of elastically scattered electrons versus carrier density and damping.

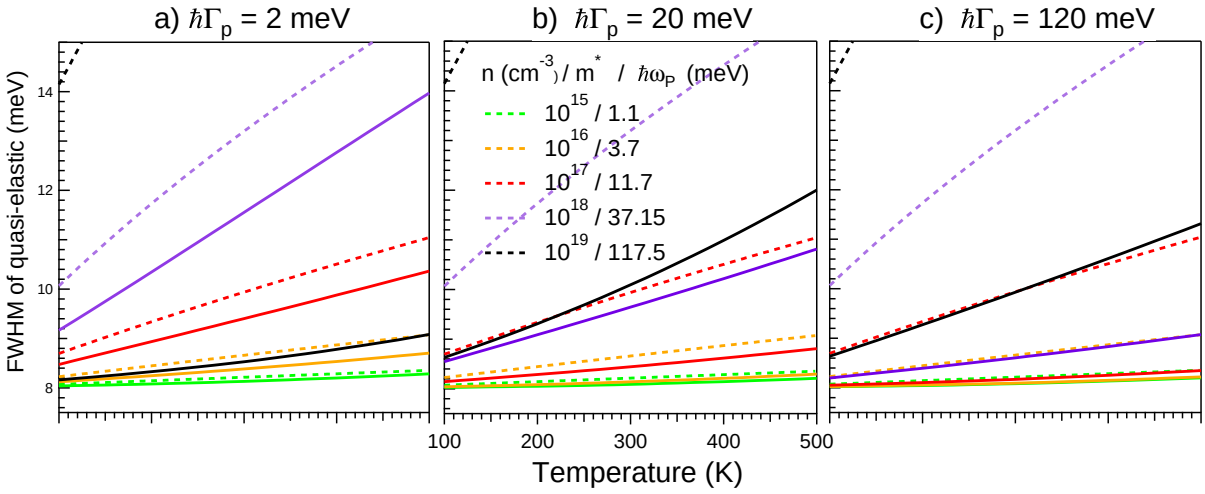

Figure 3.15: Same as Fig. 3.14 (full lines) but as a function of temperature for various carrier densities n/m^* (or plasmon frequencies ω_P) and three different dampings: a) $\hbar\Gamma_P = 2$ meV, b) $\hbar\Gamma_P = 20$ meV, c) $\hbar\Gamma_P = 120$ meV. Data are compared to the analytic results of Eq. 3.21 (dotted lines).

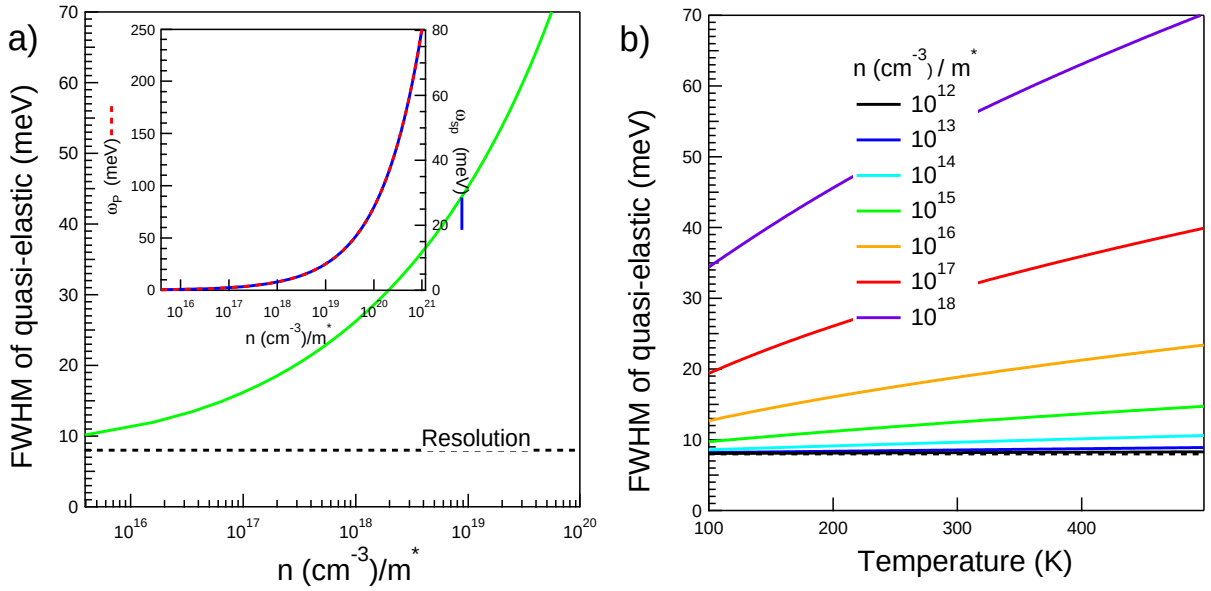

Figure 3.16: Evolution of the FWHM of the quasi-elastic peak for ZnO accordingly to Eq. 3.21 as a function of a) carrier density n/m^* at $T = 300$ K and b) of temperature for various n/m^* values. The inset shows ω_P, ω_{sp} versus n/m^*. Notice the difference with TiO_2 (Fig. 3.14-3.15).

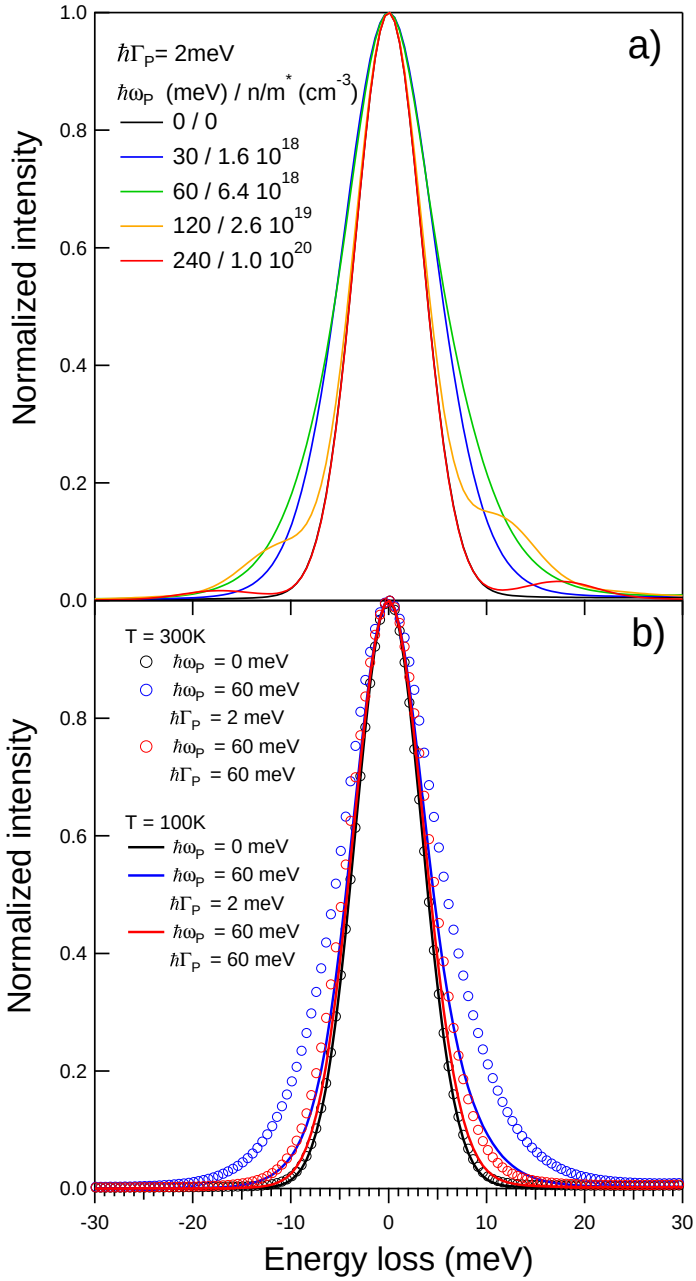

Figure 3.17: Elastic peak shape a) for selected plasmon frequencies ω_P (or carrier density n/m^*) at given broadening $\hbar\Gamma_P = 2$ meV and room temperature and, b) at two different temperatures $T = 100, 300$ K for plasma frequencies ω_P, Γ_P given in figure.

called "plasmaron" [99, 100, 143]. In parallel, the quasi-elastic maximum follows the reverse trend by decreasing before the turn over point and then increasing up to value higher than with a carrier-free substrate (Fig. 3.17-b). This translates the increase of the elastic contribution to the quasi-elastic. Indeed, as shown in the inset of Fig. 3.14, the progressive metallization of the substrate increases the fraction of electrons which are actually elastically scattered; it is given theoretically [61] by $e^{\mathcal{P}(t=0)}$ (Eq. 3.11). Furthermore, a measurable temperature dependence of the elastic peak is found with a complex interplay between damping and carrier density (Fig. 3.15). Indeed, despite the existence of possible combinations of phonon modes at $\hbar\omega_{sph,2} - \hbar\omega_{sph,1} = 9.2$ meV, the elastic peak without carrier contribution ($\omega_P = 0$) should

be insensitive to temperature (Fig. 3.17, black curve and circles) in contrast to experimental findings (see Chap. 5-Fig. 5.4).

In passing, it is worth noticing that the analytic Eq. 3.21 is not even able to reproduce the behaviour at very small damping (Fig. 3.14 black dotted vs black full line) since the underlying limit $\omega_{sp} \to 0$ is not reached; it also overestimates too much the temperature dependence.

3.2.4.3 Screening of phonons by carrier excitations

The plasmon-phonon coupling was addressed by J.-F. Baumard and F. Gervais [29, 111] in their infrared study of samples with variable reduction states. As shown in Figs. 3.18-3.19-3.20, free carriers have a triple effect on phonon losses: (i) a broadening, (ii) a shift toward higher frequency and (iii) a variation of the relative intensity of the features. The broadening is clearly the consequence of surface plasmon multiple excitations (see inset of Fig. 3.18) but also of the damping Γ_P and follows more or less the trend of the quasi-elastic peak. Regarding shifts, the low energy phonons at $\hbar\omega_{sph,1} \simeq 45.2$ meV and $\hbar\omega_{sph,2} \simeq 54.4$ meV are much less affected than the peak around $\hbar\omega_{sph,3} \simeq 92.9$ meV which is the focus of Fig. 3.19. This trend is particularly clear in Fig. 3.20 where fictitious spectra are plotted in the single loss approximation at reduced damping to enhance peak visibility; the shift which is a direct consequence of the screening of phonon excitation by carriers correlates with the appearance of the surface plasmon feature close to the elastic peak. Up to a carrier density of $n/m^* \simeq 5\,10^{17}$ cm^{-3} ($\hbar\omega_P \simeq 20$ meV) (Figs. 3.19-3.20), $\hbar\omega_{sph,3}$ stays constant at its bulk value 95.4 meV with a slight decrease in intensity due to broadening. Above, a nearly Γ_P-independent and noticeable shift is observed. In this regime, phonon intensity and its Γ_P-induced broadening are strongly correlated (Fig. 3.19-b): the higher the plasmon damping Γ_P the lower the intensity.

To first order, these findings can be rationalized in the single excitation regime by accounting for phonons with a model of isolated oscillator of strength Ω, frequency ω_0 and damping Γ screened by a constant background ϵ_c:

$$\epsilon_{osc}(\omega) = \epsilon_c + \frac{\Omega^2}{\omega_0^2 - \omega^2 - i\Gamma\omega}. \tag{3.22}$$

Close to ω_0, the corresponding loss function:

$$\mathrm{Im}\left[\frac{1}{1+\xi_{osc}(\omega)}\right] = \frac{\Gamma\omega\Omega^2}{\left[(1+\epsilon_c)(\omega_0^2-\omega^2)+\Omega^2\right]^2 + \Gamma^2\omega^2(1+\epsilon_c)^2} \tag{3.23}$$

displays a quasi-lorentzian shape [61] centered on ω_{osc}, of intensity I_{osc} and of FWHM W_{osc} given by:

$$\omega_{osc} = \omega_0 + \frac{\Omega^2}{2\omega_0(1+\epsilon_c)}, \tag{3.24}$$

$$I_{osc} = \frac{\Omega^2}{\Gamma\omega_0(1+\epsilon_c)^2}, \tag{3.25}$$

$$W_{osc} = \frac{\Omega^2}{\omega_0(1+\epsilon_c)} - \Gamma. \tag{3.26}$$

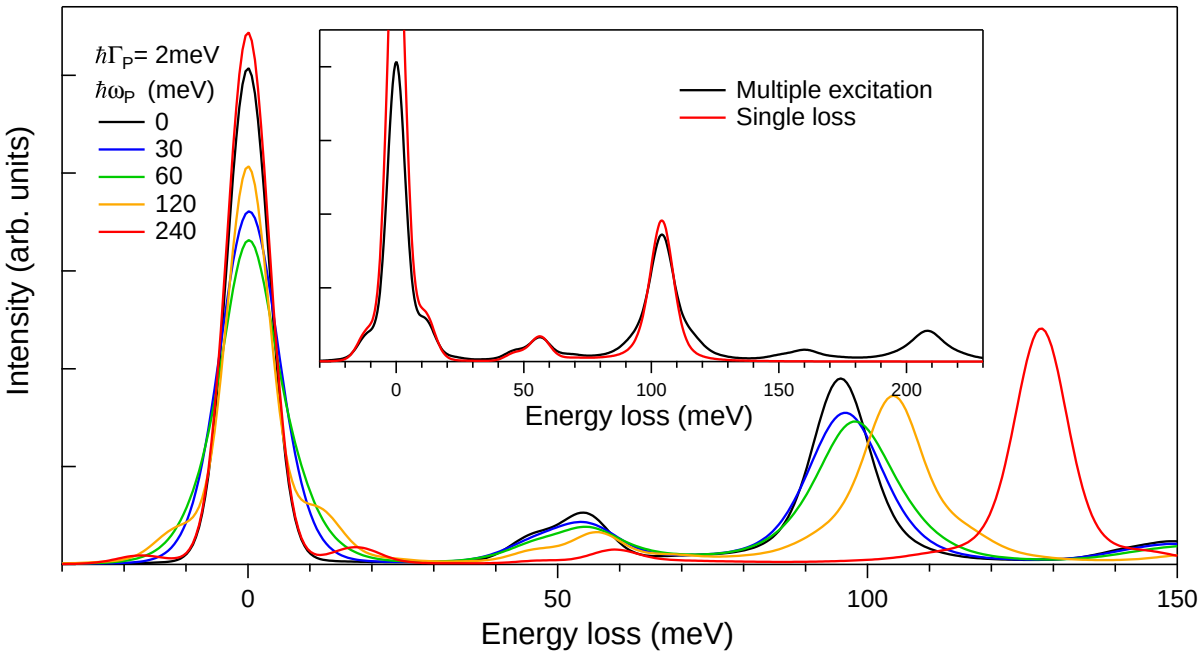

Figure 3.18: Evolution of the phonon energy loss region with the plasmon frequency ω_P at fixed damping $\hbar\Gamma_P = 2$ meV. Multiple (black line) and single (red line) losses are compared in the inset in the $\hbar\omega_P = 120$ meV case.

In the case of plasmon, the screening constant $\epsilon_c \simeq \epsilon_{c,0} - \omega_P^2/\omega_0^2$ decreases with the plasmon frequency below the value given by the remaining excitations $\epsilon_{c,0}$. For plasmon frequencies smaller than the oscillator eigen-frequency ω_0 or more precisely when $\omega_P \ll \omega_0\sqrt{1+\epsilon_{c,0}}$, the frequency shift, the variation of intensity and the width vary linearly with the carrier density $n \sim \omega_P^2$ with slopes α_P, β_P given by:

$$\Delta\omega_{osc} = \alpha_P\omega_P^2 = \frac{\Omega^2\omega_P^2}{2\omega_0^3(1+\epsilon_{c,0})^2}, \tag{3.27}$$

$$\Delta I_{osc}/I_{osc} = \beta_P\omega_P^2 = \frac{2\omega_P^2}{\omega_0^2(1+\epsilon_{c,0})^2}, \tag{3.28}$$

$$\Delta W_{osc} = 2\alpha_P\omega_P^2 = \frac{\Omega^2\omega_P^2}{\omega_0^3(1+\epsilon_{c,0})^2}. \tag{3.29}$$

Although the trend of shift towards higher energy is well predicted, the model is not able to give quantitatively absolute values. By using the oscillator strengths of Ref. [119] and $\epsilon_{c,0}$ obtained from the parametrization of Ref. [114] (see Sect. 3.2.2), the calculated slope values α_P given in Tab. 3.2 are systematically larger than the ones obtained through simulations with single excitation. Although the linearity of the phonon shift with ω_P^2 is verified below $(\omega_P^m)^2$ (see inset of Fig. 3.19), the discrepancy lies in the hypothesis of independent oscillators, not speaking about multiple excitations and plasmon damping; a shift of a given peak will change in a sizeable way the screening of its neighbours. To first order, $\omega_{sph,3}$ is expected to

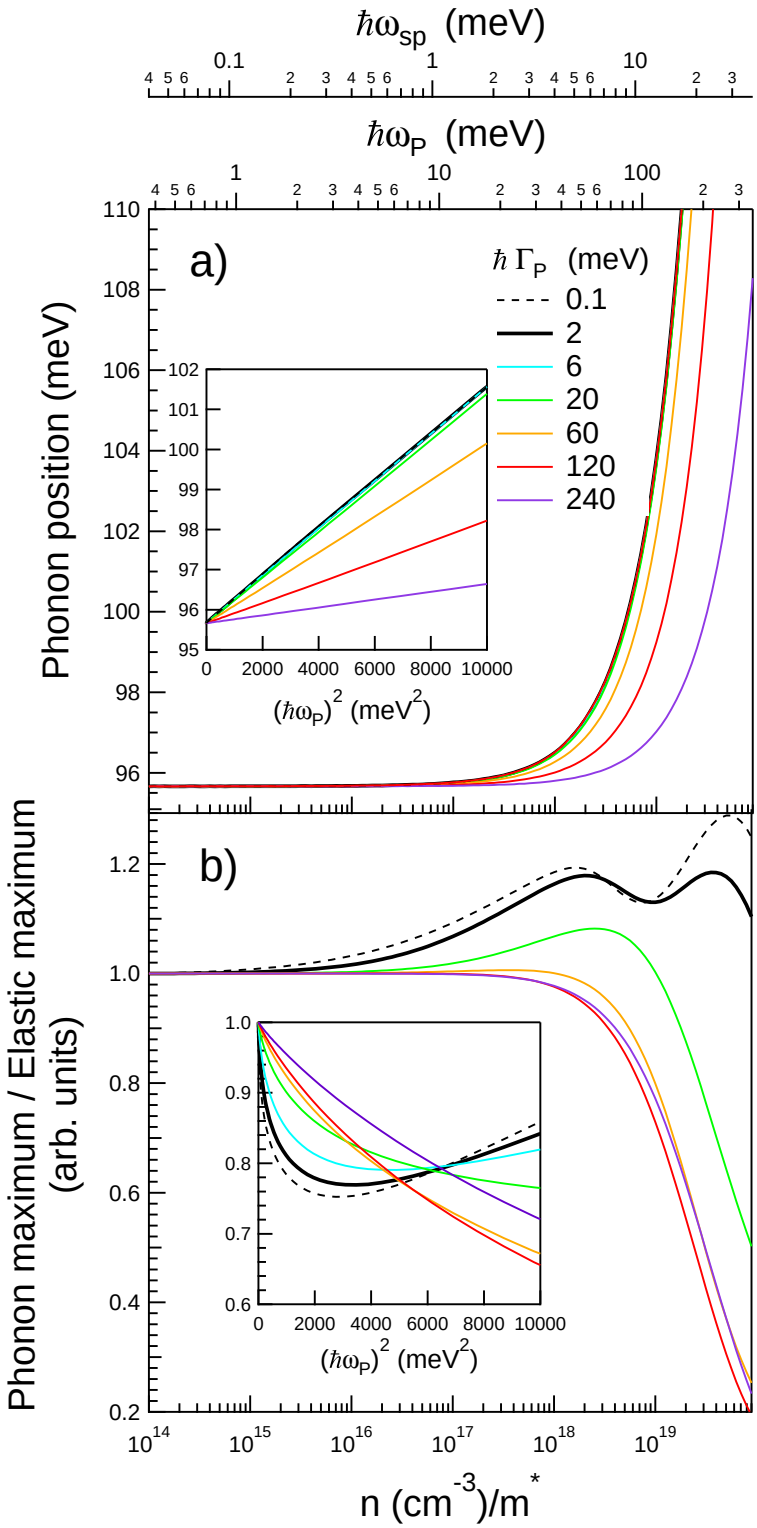

Figure 3.19: Dependence on carrier density n/m^* (bottom scale) or plasmon frequencies ω_P, ω_{sp} (top scales) for various dampings Γ_P of the $\omega_{sph,3}$-phonon: a) peak position and b) peak intensity normalized to elastic intensity. Simulations include multiple excitations. The insets show the position and phonon intensity as a function of $\omega_P^2 = ne^2/m_e m^* \epsilon_0$ once normalized to elastic.

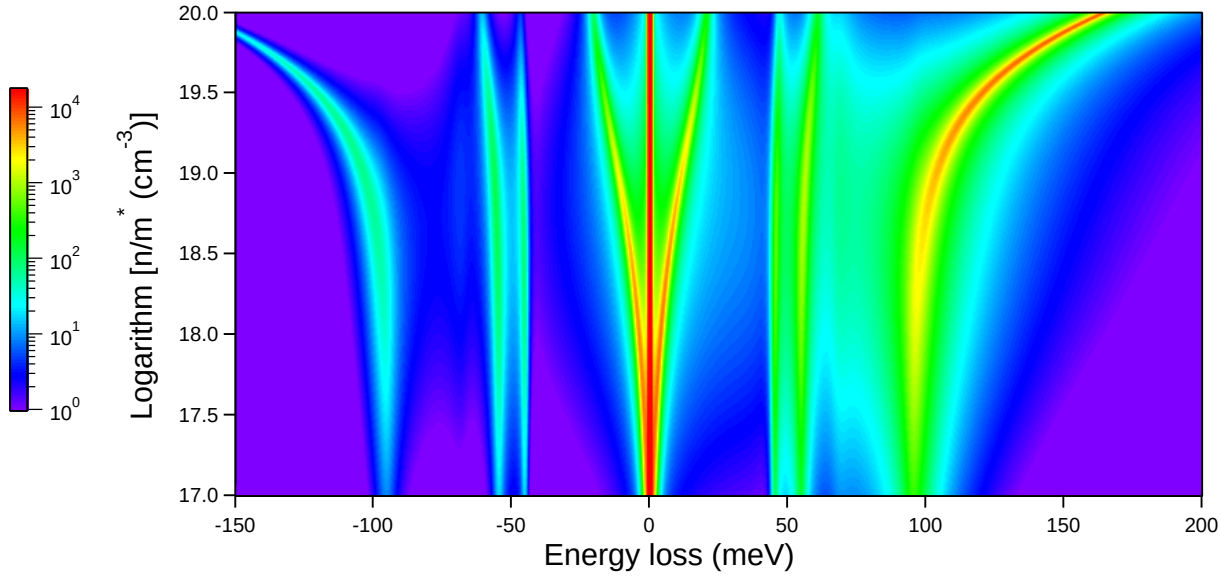

Figure 3.20: Map of HREELS spectra in the single loss approximation at enhanced resolution $\Delta_a = 1$ meV and poor phonon/plasmon damping $\hbar\Gamma = 1$ meV as a function of carrier density n/m^*. Notice the correlation between the appearance of the plasmon feature and the strong shift of the high energy surface phonon $\omega_{sph,3}$.

Phonon	$\hbar\omega_{sph}$ (meV)	$\hbar\omega_0$ (meV)	$\hbar\Omega$ (meV)	$\epsilon_{c,0}$
1	45.3	23.4	204.9	25.8
2	54.6	47	50	2.6
3	95.4	62.7	87.7	1.6

Phonon	ω_P^m (meV)	ω_{gs}^m (meV)	$\alpha_P \times 10^4$ (meV^{-2})	$\beta_P \times 10^4$	$\alpha_{gs} \times 10^6$ (meV^{-2})	$\beta_{gs} \times 10^6$
1	121	5200	22.9/0.8	0.7	1.25/0.1	0.07
2	89.2	1900	9.4/1.4	1.25	2.0/0.4	0.55
3	101	1600	23.1/5.7	1.0	9.1/4.5	0.77

Table 3.2: Screening effect of longitudinal phonons by plasmon and band gap states: surface frequency ω_{sph}, transverse frequency $\omega_0 = \omega_{TO}$, oscillator strength Ω from decomposition of Ref. [119], screening value $\epsilon_{c,0}$, maximum value for linearity $\omega_P^m = \omega_0\sqrt{1+\epsilon_{c,0}}$ and $\omega_{gs}^m = \omega_{gs}\sqrt{1+\epsilon_{c,0}}$, slopes α_P, α_{gs} (from Eq. 3.24/from full calculations) and β_P, β_{gs} with ω_P^2 and Ω_{gs}^2 (see text for definition).

shift faster than $\omega_{sph,2}$ which decreases the screening $\epsilon_{c,0}$ and therefore increases its α_P. The same reasoning applies to $\omega_{sph,1}$ and its neighbours at high energy $\omega_{sph,2}$. Regarding peak intensity and broadening, the situation is even more complex. Anyway, accordingly to the inset of Fig. 3.19, if all multiple excitations are taken into account, a sizable shift of several meV is to be expected for $\omega_{sph,3}$ while increasing ω_P up to 100 meV and therefore the carrier concentration up to $n/m^* = 7\,10^{18}$ cm^{-3}.

3.2.4.4 Screening of phonons by band gap states

The impact of band gap states on polar phonons of TiO_2 was envisionned in the original HREELS works [21, 89, 90] and indirectly in infrared study of Refs. [29, 111] as modification of the dielectric function at infinity ϵ_∞ for phonons (see Eq. 3.15).

EELS spectra with a beam energy $E_I = 38$ eV and a resolution $\Delta_a = 50$ meV similar to experiments have been calculated including BGS described by an oscillator (Eq. 3.18) of strength Ω_{gs} in a semi-infinite substrate (Fig. 3.21-a inset). This latter appears as a low intensity feature in between the phonon clump and the band-to-band transitions located above the 3.2 eV band gap of rutile. Besides an obvious increase of its intensity with Ω_{gs}, the BGS shifts to higher energy (Fig. 3.23-a) and gets asymmetric because of multiple excitations; in particular, a second order excitation appear in the $\hbar\Omega_{gs} = 2000$ meV curve of the inset of Fig. 3.21-a at around 2500 meV. As shown by Eq. 3.24 for a simple oscillator, this shift roots into the EELS cross section which is proportional to $\mathrm{Im}(1/1 + \epsilon(\omega))$ (see Eq. 3.23) and is linear in Ω_{gs}^2 modulo the sensitivity function as shown in Fig. 3.23-a.

In contrast to interband transitions which seem insensitive to BGS [7], the phonon region is strongly affected by the BGS intensity. This screening effect is fairly well illustrated in Fig. 3.21-a in high resolution spectrum including (Fig. 3.21-a) or not (Fig. 3.22) the multiple losses, but it is less obvious at moderate resolution (Fig. 3.21-a, inset). Phonons evolve in the opposite direction to the case of carrier excitations; they all redshift and the $\omega_{sph,3}$ intensity decreases (Fig. 3.23-b). Phonon screening by the tail of BGS excitation is again the main driving force but in this case, since the frequency of BGS is larger than those of phonons, the real part of the BGS dielectric component is negative. In a similar way to the case of carrier excitations, the effect can be rationalized and understood by accounting for phonons by isolated oscillators (Eq. 3.6); this leads to variations of position, intensity and broadening linear in Ω_{gs}^2 in the regime of single excitation and for $\Omega_{gs} \ll \omega_{gs}^m = \omega_{gs}\sqrt{1+\epsilon_{c,0}}$:

$$\Delta\omega_{osc} = -\alpha_{gs}\Omega_{gs}^2 = -\frac{\Omega^2\Omega_{gs}^2}{2\omega_0\omega_{gs}(1+\epsilon_{c,gs})^2}, \tag{3.30}$$

$$\Delta I_{osc}/I_{osc} = -\beta_{gs}\Omega_{gs}^2 = -\frac{2\Omega_{gs}^2}{\omega_{gs}^2(1+\epsilon_{c,gs})^2}, \tag{3.31}$$

$$\Delta W_{osc} = -2\alpha_{gs}\Omega_{gs}^2 = -\frac{\Omega^2\Omega_{gs}^2}{\omega_0\omega_{gs}(1+\epsilon_{c,gs})^2}. \tag{3.32}$$

The main findings *i.e* downwards shifts and decreases of phonon intensities obtained in the case of multiple excitations (Fig. 3.23-a) are well accounted for. But again, the failure of the hypothesis of isolated oscillators and single loss explains the quantitative discrepancy between calculated slopes α_{gs}, β_{gs} and actual ones (see Tab. 3.2 for the comparison).

Surprisingly, the BGS also impacts the quasi-elastic peak intensity which increases at constant FWHM (Fig. 3.23-a). This phenomenon finds its origin in the transfer of intensity

[7] Because of much smaller oscillator strengths than phonons (See Fig. 3.8)

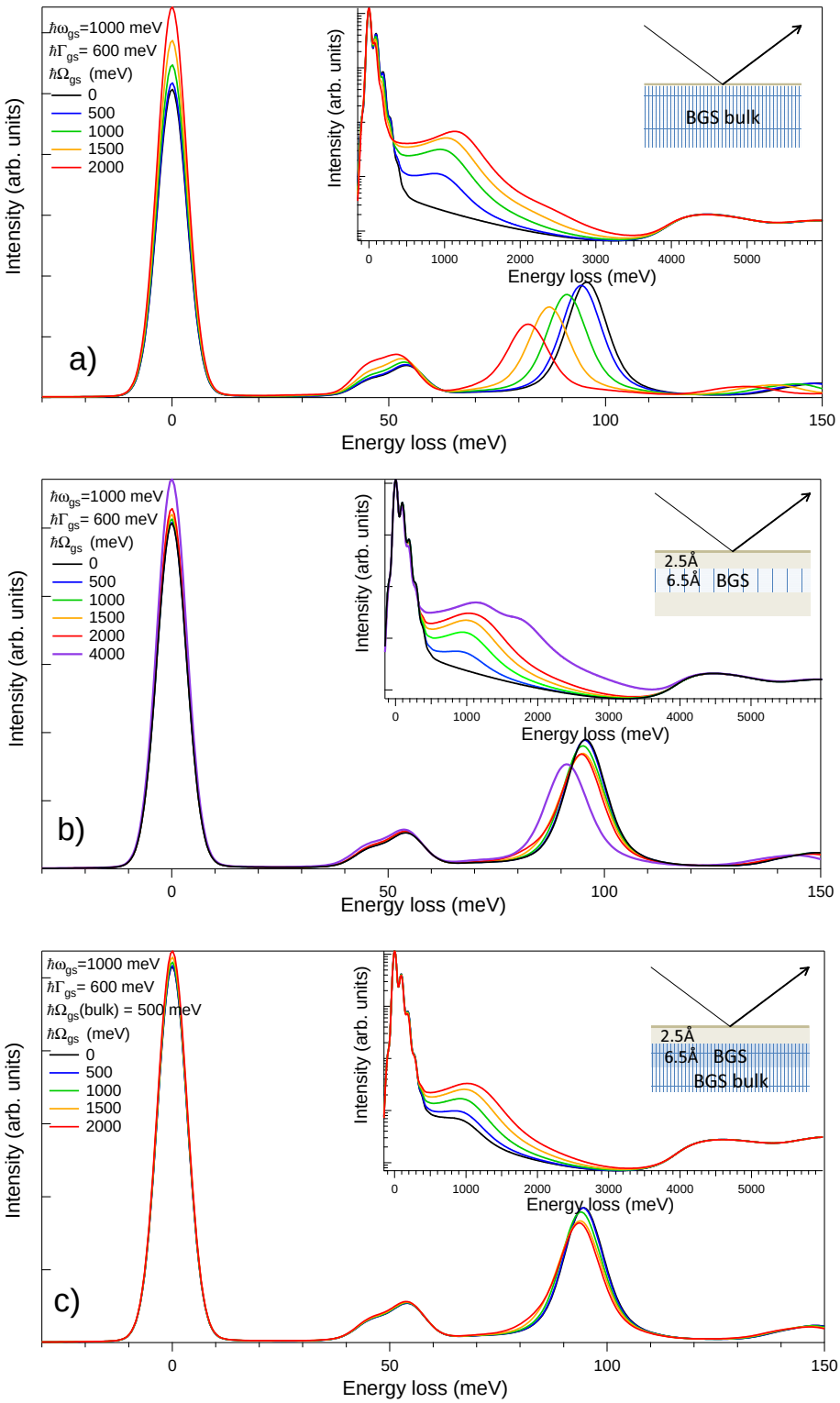

Figure 3.21: Evolution of the phonon (main graphs, linear scale) and band gap (insets, logarithmic scale) electron energy loss spectra as a function of the band gap state strength Ω_{gs} (at constant frequency $\hbar\omega_{gs} = 1000$ meV and damping $\hbar\Gamma_{gs} = 600$ meV): a) semi-infinite substrate, b) BGS localised in a layer thickness 6.5 Å just below the surface, and c) mixture of both configurations with $\hbar\omega_{gs}^{bulk} = 500$ meV. Dielectric profile is chosen accordingly to the fits of Chap. 5-Sect. 5.2.2

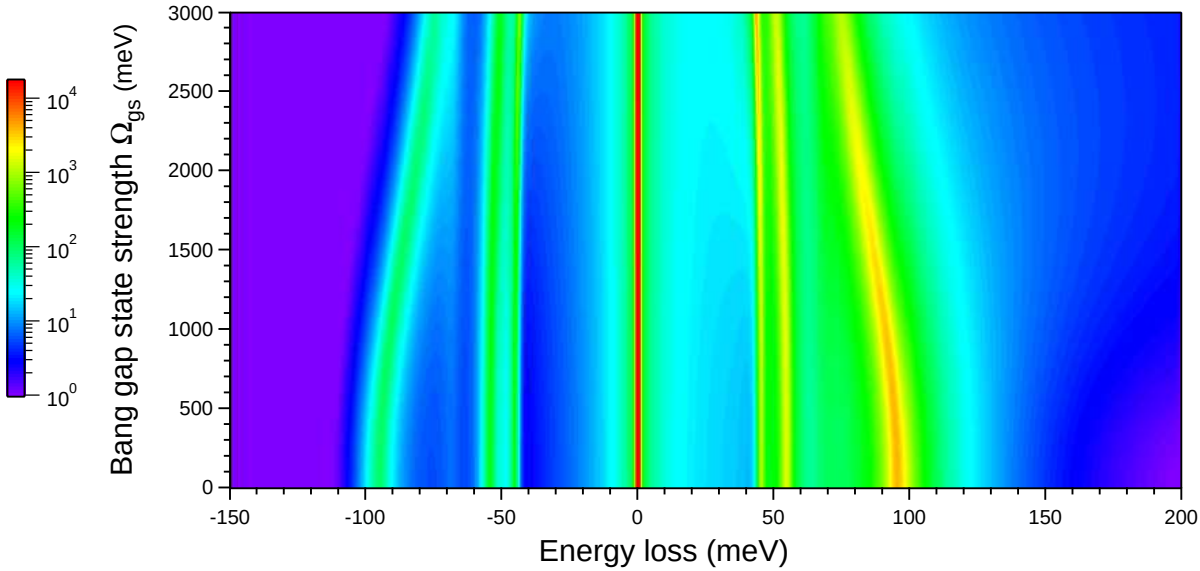

Figure 3.22: Map of HREELS spectra of phonons in the single loss approximation at enhanced resolution $\Delta_a = 1$ meV and poor phonon/plasmon damping $\hbar\Gamma = 1$ meV as a function of band gap state strength Ω_{gs}. A clear downward shift of the surface phonons, in particular $\omega_{sphn,3}$ is observed.

from phonons and their multiple excitations to the actual elastic contribution of the quasi-elastic peak. Therefore, once normalized to the elastic peak, the phonons decrease in intensity upon increasing the BGS strength (Fig. 3.23-b inset). This relative variation of phonon/elastic appears in an obvious way on experimental spectra during healing of defects (see Chap. 5-Fig. 5.3).

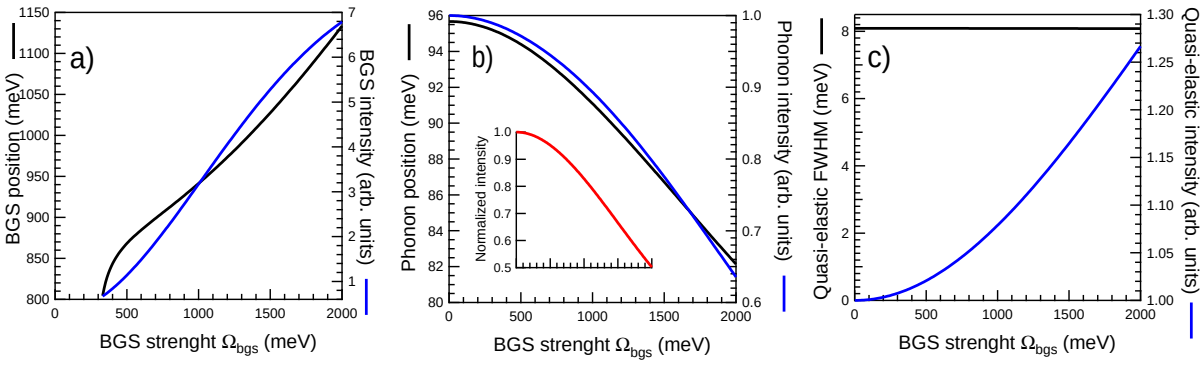

Figure 3.23: Variation with the band gap state strength Ω_{gs} of the peak intensities, positions and FWHMs of the a) BGS, b) phonon and c) elastic peak. Notice the BGS is a maximum-less shoulder below a critical Ω_{gs} value. The phonon intensity normalized to the elastic intensity is shown in inset of Fig.-b. All multiple losses have been accounted for.

3.2.5 Surface versus bulk excitations: the question of depth sensitivity

3.2.5.1 Probing depth in EELS ?

Up to now, the discussion was restricted to semi-infinite samples and any profile of dielectric function, in particular BGS, was discarded. However, a strong contribution from near-surface defects in particular oxygen vacancies is obviously expected [2–9], not speaking about the strong debate on the nature of BGS and its bulk versus surface character (see Chap. 4). This debate relies strongly on photoemission spectroscopy (in particular from ultra-violet laboratory source) and scanning tunnelling spectroscopy for which probing depth is difficult to assess although those techniques are surface sensitive. Regarding this issue, due to the dipolar interaction, the EELS in reflection has an intrinsic depth sensitivity which can be varied as a function of impact energy, loss and scattering geometry. Although there is no theoretical definition of the EELS probing depth [61, 109], a reasonable estimate is given by the evanescent decay length d_p of the electric field due to the incoming electron (see Chap. 2, Eq. 2.12). It is worth noticing that this probing depth is quite different from other electron spectroscopies for which it is based on an escape depth of inelastically scattered electrons. To first order, according to the dielectric theory, d_p is given by the inverse of the electron wave vector transfer along the perfectly specular trajectory given by $k_\parallel = (k_S - k_I)\sin\Theta_I$; this quantity given by $d_p(\theta_E, \Theta_I) = 1/(k_I\theta_E \sin\Theta_I)$ (for $\theta_E = \hbar\omega/2E_I \ll 1$) increases with the energy loss. d_p has been plotted in Fig. 3.24 for the beam energies $E_I = 8; 38$ eV, typical for phonon and BGS loss regimes. It is also compared to its average over a detector aperture of $\theta_c = 1^\circ$ for a perfectly parallel incoming beam:

$$\begin{aligned} \langle d_p \rangle (\theta_E, \Theta_I, \theta_c) &= \frac{1}{\pi\theta_c^2} \int_0^{\theta_c} \theta_S d\theta_S \int_0^{2\pi} d\phi_S d_p(\theta_S, \phi_S) \\ \frac{1}{d_p(\theta_E, \Theta_I, \theta_S, \phi_S)} &= k_I \left[(\theta_E \sin\Theta_I - \theta_S \cos\phi_S \cos\Theta_I)^2 + (\theta_S \sin\phi_S)^2 \right]^{1/2}. \end{aligned} \quad (3.33)$$

While the measurements are bulk sensitive for phonons ($d_p \simeq 200$ Å) not speaking about quasi-elastic excitations, EELS at $E_I = 38$ eV probes the sub-surface at the BGS energy ($d_p \simeq 30$ Å) and is very surface sensitive in the case of interband transition ($d_p < 10$ Å). Of course, the higher the beam energy the deeper the probing depth. The main effect of slit integration is to smoothen the divergence at $\theta_E = 0$. Even if trends are correctly described, those figures should be taken with caution since the EELS cross section dependence on a given profile is quite complex (see Eqs. 3.1,3.6). The case of a semi-infinite medium *i.e.* a constant profile of $\epsilon(\omega)$ given by the bulk sensitivity function $F(\mathbf{k}_I, \omega)$ [61] (see Sect. 3.2.1.2) does not event follow the $d_p(\omega)$ trend (Fig. 3.24). Already in this case, a better definition of d_p should account for the weight given for each $k_\parallel$ by the sensitivity function; as demonstrated in Ref. [109], this decreases the probing depth from $d_p = 1/(k_I \sin\Theta_I \theta_E)$ to values lower than $d_P = 1/(k_I\theta_E)$.

Regarding out-of-specular measurements, the definition of the probing depth is even less clear since impact scattering starts dominating the electron-target interaction. Nevertheless,

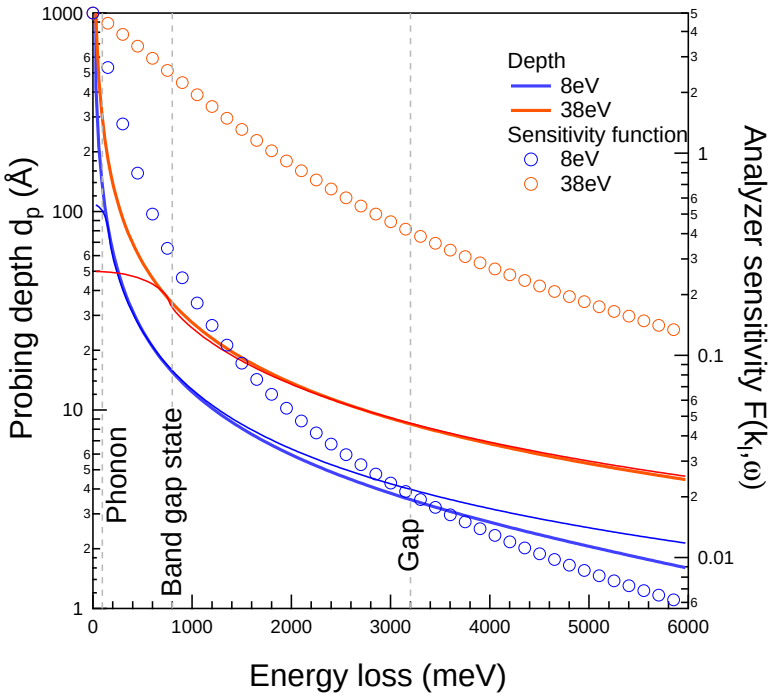

Figure 3.24: Probing depths (left scale) and analyser sensitivity function (right scale) for two beam energies $E_I = 8; 38$ eV. The simple estimate d_p (thick lines) is compared to the average $\langle d_p \rangle$ over a circular slit of aperture $\theta_c = 1°$ (thin lines) (see text). Phonon, band gap state and band gap of TiO_2 are shown by dotted lines. Notice that d_p was also calculated well outside the regime of negligible loss at $E_I = 8$ eV.

the inverse $d_p^{os} = 1/k_\parallel^{os}$ of the wave vector transfer given by:

$$k_\parallel^{os}(\theta_E, \Theta_I, \Theta_S, \theta_s, \phi_S) = k_I \left[(\theta_E \sin\Theta_S + \sin\Theta_I - \sin\Theta_S - \theta_S \cos\phi_S \cos\Theta_S)^2 + (\theta_S \sin\phi_S)^2 \right]^{1/2} \tag{3.34}$$

can still be used to estimate the probing depth. Θ_S is the detection angle as measured from the normal to the surface (see Fig. 3.1) and a similar slit average $\langle d_p^{os} \rangle$ to Eq. 3.33 can be performed. As shown in Fig. 3.25 for the two typical beam energies $E = 8 and 38$ eV at fixed incidence Θ_I, $\langle d_p^{os} \rangle$ drops quickly at fixed energy loss as soon as the detection angle Θ_S gets away from the resonant condition given by $k_\parallel^{os}(\theta_s = 0) = 0$ *i.e.* $\sin\Theta_S = \sin\Theta_I/(1+\theta_E)$. Therefore, to be more surface sensitive simultaneously for all energy losses, this resonance should be avoided by rotating the analyser towards the surface normal.

3.2.5.2 A few examples of effects of dielectric function profile

For a give dielectric profile, the depth sensitivity of the technique depends not only on the sensitivity function $F(\mathbf{k}_I, \omega)$ but also on the $k_\parallel$-dependence of the loss function $G(k_\parallel, \omega)$ (Eq. 3.1) which expression is complex for a stratified medium (Eq. 3.6). Therefore, it is mandatory to resort to full numerical simulations to accurately discuss depth sensitivity effects and profile of dielectric function. The aim of this section is to illustrate this sensitivity through selected pertinent examples.

In Figs. 3.21, several models of distribution of BGS (bulk Fig. 3.21-a, subsurface Fig. 3.21-b, and mixture of both Fig. 3.21-c) are compared for an increasing BGS oscillator strength. As shown in the schematic profile of the inset, subsurface BGS are put in a 6.5 Å thick layer below a 2.5 Å dead-layer to mimic the localisation of charge on subsurface Ti atoms seen by resonant photoemission experiments [52] (see Sect. 4.6.2 and Sect. 5.2.2 for a full justification). While

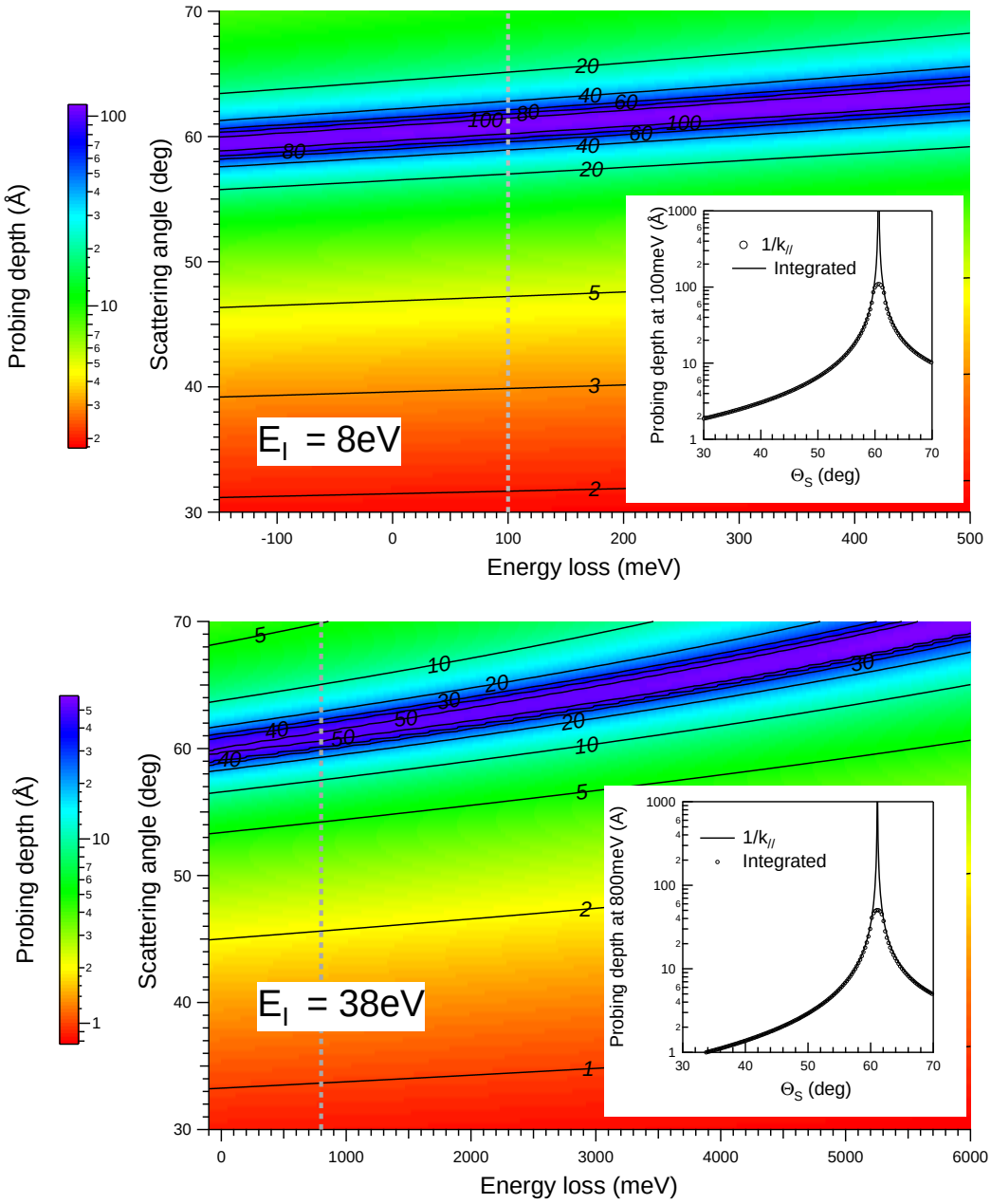

Figure 3.25: Out-of-specular probing depth $\langle d_p^{os} \rangle$ averaged a detector aperture $\theta_c = 1°$ as a function of energy loss and detection angle Θ_S at fixed $\Theta_I = 60°$ incident angle for beam energies of $E_I = 8$ eV (top panel) and $E_I = 38$ eV (bottom panel). The angular range ($\Theta_I = 60°, \Theta_S = 30 - 70°$) corresponds to the accessible scattering geometry of our monochromator-analyser setup at fixed sample position (see Fig. 3.1). The inset shows $\langle d_p^{os} \rangle$ and $d_p^{os}(\theta_S = 0)$ at typical phonon and BGS loss values (gray dotted line on the map)

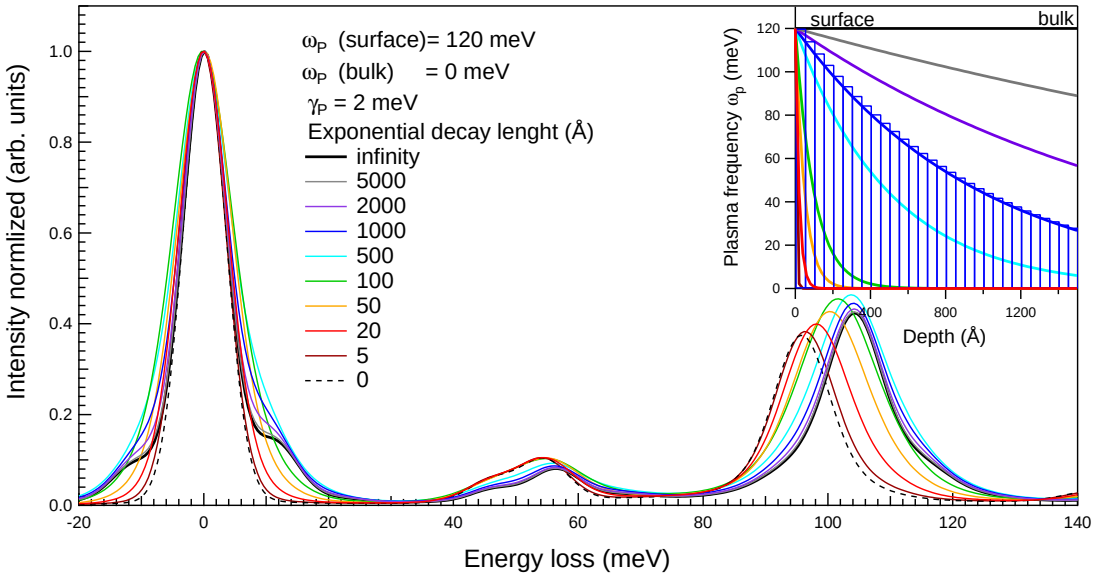

Figure 3.26: Effect of an exponential gradient of carrier density (shown in inset) on the HREELS phonon spectrum in the absence of BGS contribution. The plasma frequency goes from $\hbar\omega_P = 120$ meV at the surface to $\hbar\omega_P = 0$ meV in the bulk while the damping is taken constant equal to $\hbar\Gamma_P = 2$ meV. The exponential decay length goes from 0 Å to infinity *i.e.* from an undoped substrate to flat profile. The profile is sampled over 60 slices in between 0 and 3Λ as illustrated by the blue staircase curve for $\Lambda = 1000$ Å. Spectra are normalized to the elastic peak maximum.

bulk BGS have a sizeable impact on phonon position and intensity relative to elastic peak (Fig. 3.23-a), this effect is considerably damped for a subsurface excitation despite a similar intensity as a band gap feature in EELS (Fig. 3.21-b). This effect finds its origin in the difference of probing depth between excitations at phonon and band gap state energies (Fig. 3.24). In a similar way, a bulk BGS excitation buried at a depth below 6.5+2.5=9 Å (Fig. 3.23-c; black line in inset) is barely visible but strongly shift the main phonon peak (Fig. 3.23-b and Fig. 3.23-c; black lines).

Fig. 3.26 illustrates the case of a more complex profile of dielectric function which describes an exponential decaying gradient of carriers from a surface value $\hbar\omega_P = 120$ meV to a bulk value $\hbar\omega_P = 0$ meV. This profile could mimic an accumulation layer due to band-bending and charge transfer with surface defects. The profile was sampled in a stair case way (inset of Fig. 3.26) over 3 times the decay length Λ and the loss function computed recursively as described in Sect. 3.2.1.4 (Eq. 3.6). The effects on the quasi-elastic peak, the phonon position and their relative ratio is similar to the trends that were described in Sects. 3.2.4.3-3.2.4.4 for a semi-infinite sample. Interestingly, the spectrum poorly evolves between $\Lambda = 2000$ Å(violet curve) and a bulk substrate (bold black line) in the phonon range while sizeable differences are still visible for the quasi-elastic peak. The explanation lies in the difference of probing depth (see Fig. 3.24) at the two energies. The sensitivity to such high Λ-values for phonons

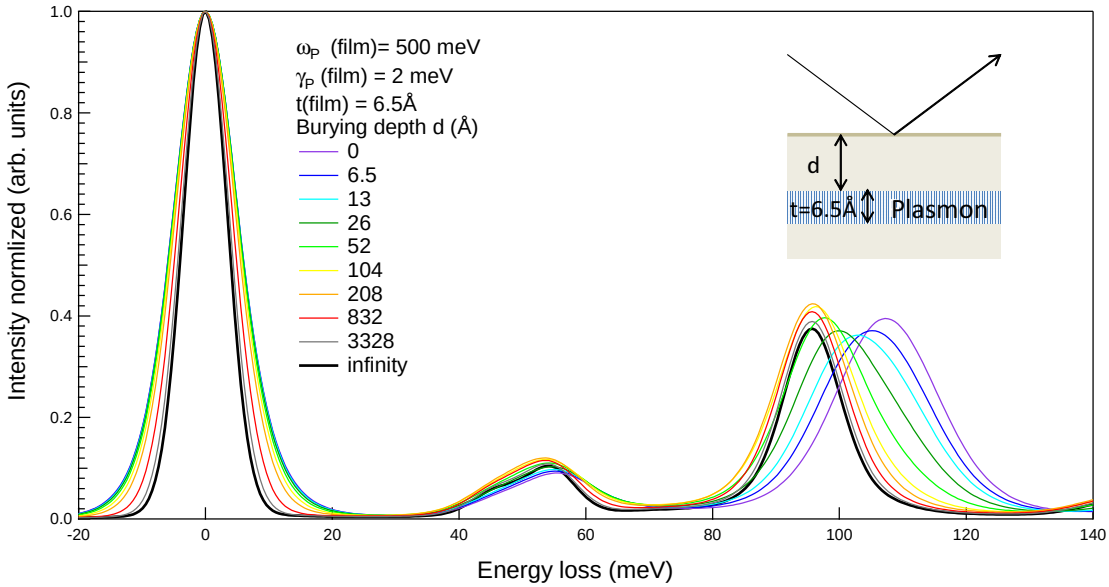

Figure 3.27: Effect of a conductive layer ($\hbar\omega_P = 500$ meV, $\hbar\Gamma_p = 2$ meV, $t = 6.5$ Å) buried at different depth d on the HREELS phonon spectrum (see inset). Spectra are normalized to the elastic peak maximum.

compared to the expected probing depth $d_p \simeq 200$ Å lies only in the initial difference of slopes of $\omega_P(z)$; this would mean that a linear profile would give a quite similar spectrum.

The last example (Fig. 3.27)deals with a fictitious highly conductive layer ($\hbar\Gamma_p = 2$ meV) of thickness ($t = 6.5$ Å) equivalent to the distance between Ti planes buried at increasing depth below the surface. Its plasma frequency $\hbar\omega_P = 500$ meV corresponds to a surface carrier density of $n_S/m^* = 1.2\,10^{13}$ cm^2 typical for a doping by a fraction of monolayer of defects (see Chap. 5-Sect. 5.2.2). This layer impacts the phonon position $\omega_{sph,3}$ down to around the expected probing depth of $1/k_{\|} = d_p \simeq 200$ Å, but the peak intensity is not yet converged. The surface plasmon excitation confined in this layer are still able to broaden the quasi-elastic peak up to a rather large burying depth.

3.3 Resolution enhancement in EELS based on iterative semi-blind Lucy-Richardson algorithm

A new spectral restoration algorithm of reflection energy electron loss spectra is proposed [35]. It is based on the maximum likelihood principle as implemented in the iterative Lucy-Richardson approach. Resolution is enhanced and point spread function recovered in a semi-blind way by forcing cyclically the zero loss to converge towards a Dirac peak. Synthetic phonon spectra of TiO_2 are used as a test bed to discuss resolution enhancement, convergence benefit, stability towards noise and apparatus function recovery. Attention is focused on the interplay between spectral restoration and quasi-elastic broadening due to free carri-

ers. A resolution enhancement by a factor up to 6 on the elastic peak width can be obtained on experimental spectra of TiO_2(110) and helps revealing mixed phonon/plasmon excitations.

The published article [35] is given in annex Chap. 7

3.4 Conclusion

This theoretical chapter used intensively the dielectric approach to describe the impact of all solid-state excitations on the shaping of (HR)EELS spectra of reduced TiO_2. It was proposed to describe BGS by an oscillator and conductivity through a Drude term. While BGS appears as an isolated feature in the band gap, the signature of the existence of carriers is less obvious. The large static dielectric function of the material combined a sizeable effective mass lead only to a broadening of the quasi-elastic peak through the excitation of surface plasmons at moderate carrier density. Enhancing apparent resolution allows to glimpse their existence and their combination modes with surface phonons. Fortunately, the carrier excitations can be tracked down not only through the imaginary part of their dielectric function but also through the real part and the screening that it induces. Due to its very large oscillator strength, one longitudinal phonon can be used as a reporter; with frequency which is between the frequencies of Drude term and BGS, it shifts upwards with the plasmon frequency and downwards with the BGS oscillator strength. However, the effect of the profile of dielectric function, in particular due to the existence of surface vacancies may blur these conclusions. Thus, the next chapter will employed the above evoked energy and angular depth sensitivity of the (HR)EELS technique to gain some insights on this profile and the surface versus bulk contributions.

CHAPTER 4

SURFACE VERSUS BULK CONTRIBUTION TO THE BAND GAP STATES IN TiO_2

4.1 Introduction

Titanium dioxide is a promising material in many important fields due its (photo)catalytic properties [1, 2, 8], especially those related to energy and environment such as water and air treatment, hydrogen production by water splitting and solar energy conversion. In this respect, point defects play a key role in the production of active species resulting from complex pathways of adsorption and dissociation of oxygen and water (see reviews [2–8]). The creation of defects results in the filling of a Ti 3d level by the so-called associated excess electrons and the appearance of a Ti^{3+} formal oxidation state. Experimental evidences of those levels are numerous [2–8] and obtained with techniques with variable depth sensitivity: photoemission [10, 12, 20, 52, 130], electron energy loss [21, 89, 131], occupied density of states in scanning tunneling spectroscopy [15, 22], near-infrared optical absorption [23, 132, 133] and electron spin-resonance [24]. They appear as broad feature at 0.8-1 eV below the Fermi level and can be produced in various ways (reduction by annealing, bombardement, doping, photoexcitation etc....). But yet, the nature and the spatial distribution in the surface region of the defects and of the resulting band gap states (BGS) is not fully understood. On TiO_2(110), the dominant contribution to BGS, either oxygen vacancies O_b-vac or titanium interstitials Ti_{int} [1], either surface or bulk defects, is still under debate. These unresolved issues prevent a clear understanding of the surface processes that are involved in the applications of TiO_2 among which electron transport [1, 2] that is partially treated in Chap. 5.

It has long been suggested that the main origin of BGS is surface oxygen vacancies [2–7]. Y. Du *et al.* [19] argue that O_b-vac can also provide excess charges at Ti_{5c} site due to its par-

[1] The common "surface science" notation of those defects will be used in this chapter instead of the KrögerVink one from solid-state chemistry (see Sect. 2.2).

tially delocalized character. N. Petrik *et al.* [11] tested the abilities of oxygen chemisorption of samples with different surface vacancy densities but similar subsurface defects densities. Their data show that surface defects are the main cause of surface reactivity. X. Mao *et al.* [13] and C. M. Yim *et al.* [12] used different methods to prepare samples with different defects density and found a nearly linear dependence of BGS intensity in ultra-violet photoemission (UPS) on surface defects density; therefore they made the conclusion that BGS come mainly from O_b-vac. Conversely, S. Wendt *et al.* [14] found that oxygen can dissociate on Ti_{5c}, and concluded that the large amount of excess charges which are needed for this dissociation must be mainly provided by Ti_{int}. With STM, they found that the ratio between surface oxygen vacancies O_b-vac before oxygen adsorption and oxygen adsorbed on Ti_{5c} (O_{ad}) is more than 1:1 and that, besides single O_{ad}, O_{ad} pairs appear. On the basis of of Density Functional Theory (DFT) calculations and other supporting experiments, they claim that these excess O_{ad} pairs were created by a second non-vacancies related dissociation channel of O_2 on Ti_{5c} site, and the excess charges are provided by the Ti^{3+} interstitials (Ti_{int}) from subsurface. In UPS, 300 L of O_2 are needed to quench the BGS peak which is far more than what is needed to remove UPS σ-OH peak (4 L) of the hydroxylated surface; this also supports the view that excess charges can be provided by subsurface defects, *i.e.* Ti_{int}. Similar suggestions were made by E. Lira *et al.* [16–18] and by A. Papageorgiou *et al.* [15] who combined STM experiments and numerical simulations. K. Mitsuhara *et al.* [55] and S. Takata *et al.* [144] also suggested that Ti_{int} contribute to BGS. An interesting observation of K. Mitsuhara *et al.* is that upon annealing a nearly perfect surface at 870 K, the increase in intensity of BGS in photoemission spectra is not accompanied by band bending or change in work function, from which they infer that only bulk or subsurface defects are created. The spatial localisation of excess charges is another important pending questions. Firstly, through diffraction of photoelectons [52, 145] or STM data combined with *ab initio* modellings [22, 53, 54], excess electrons were suggested to locate in the subsurface instead at the very surface but the concentration profile of the excess charges over the surface region is not known. Then, while BGS are currently healed by exposure to oxygen, change in BGS intensity upon water adsorption has been observed [93], though no further discussion was provided.

The above puzzles mainly stem from the inability to experimentally distinguish the respective contributions of Ti_{int} and O_b-vac to the formation of BGS. Both an unambiguous identification of the origin of BGS and a description of the distribution of the excess charges are needed. In this chapter, a series of original experiments are performed by taking advantage of the possibilities offered by EELS in the analysis of BGS: (i) the ability of the technique to measure the surface temperature via the Bose-Einstein distribution of loss and gain phonons allows the annealing of the surface by a hot filament at temperatures at which Ti_{int} diffusion can be discriminated from the formation of O_b-vac; (ii) measurements at different sampling depths were performed by using off-specular analysis; (iii) finally, comparison of measurements at 100 and 300 K and use of electron bombardment at different energies lead to some unambiguous observations regarding surface and bulk defects and the reactivity of the defective rutile TiO_2(110) surface.

4.2 Exposure to oxygen of reduced rutile samples

Fig. 4.1 shows the evolution of BGS in EELS spectra recorded on the reduced R-TiO_2(110) surface upon exposure to molecular oxygen at 300 K (Fig. 4.1-a) and 100 K (Fig. 4.1-b). Those spectra, and most of the following ones if not stated, (i) have been acquired at a beam energy of $E_I = 38$ eV and in the specular direction $\Theta_I = \Theta_S = 60°$ *i.e.* in the dominant dipole loss regime, and (ii) been normalized to the maximum of the $\omega_{sph,3}$ phonon around 95 meV [2]. In this case, at variance to lower beam energies ($E_I = 7.5$ eV in Fig. 5.3), the ratio phonon/elastic intensity is poorly sensitive to variations related to surface conductivity change due to the larger probing depth (see Chap. 5). Although the beam energy was slitghlty higher than the threshold (34 eV) of stimulated desorption of oxygen through the Knotek-Feibelman process [56,57], spectra are stable over hours of measurements without any increase or decrease of the BGS intensity. As estimated in Ref. [94], the flux of electrons at the sample in the range of a fews nA is insignificant to produce any beam damage.

The BGS (Fig. 4.1) gives rise to an electron energy loss peaking at around 0.8 eV. Its integrated intensity normalized to the maximum value prior to exposure is shown in Fig. 4.1-c; at 100 K, the decrease in intensity is much faster than at 300 K, in particular at low coverage. In the absence of a direct titration of the density of O_b-vac, it can be assumed that it amounts to around 10 % which corresponds to $\sim 5.2 \times 10^{13}$ O_b-vac.cm^{-2}, a common order of magnitude for such a preparation method [2–8]. As shown previously, at 100 K, adsorbed oxygen heals O_b-vac but does not dissociate [93]. Since a third of the O_b-vac ($\sim 1.7 \times 10^{13}$ O_b-vac.cm^{-2}) is healed after an exposure of 0.05 L oxygen (1.65×10^{13} O_b-vac.cm^{-2}), the sticking probability of the molecular oxygen on the R-TiO2 surface can be assumed to be close to unity. This estimate is in good agreement with the value (greater than 0.5) found by M. A. Henderson [93]. This observation suggests long-living physisorbed oxygen molecules that diffuse on the rutile surface until they adsorb on O_b-vac sites [93] to quench the excess electrons. The much slower healing of O_b-vac on rutile at 300 K is indicative of a shorter lifetime for physisorbed oxygen. However, the normalized BGS intensity of 0.37 that is reached after 3000 L is similar to that reached after a few tens of Langmuirs at 100 K (Fig. 4.1- c). This has two important consequences. Firstly, the BGS healing likely results in both cases from oxygen adsorption on the same sites even if the adsorption mechanisms are different since at 300 K, in contrast with what happens at 100 K, oxygen molecules dissociate on O_b-vac to give rise to bridging oxygens and oxygen adatoms [131] sitting on the Ti_{5c} sites of the surface [4–7,94]. The second consequence of the above observation is that the healing does not involve any diffusion of Ti_{int} since this diffusion is definitely prevented at 100 K (see Sect 2.2.1) in rutile [49,146] due to the activation energy of around 1 eV [14, 42, 50]. Nevertheless, this does not mean that Ti_{int} do not contribute to the healed BGS. A charge transfer cannot be excluded in a way similar as that described by A. C. Papageorgiou *et al.* [15] or S. Wendt [14]. Another pending question is the origin of the remaining BGS intensity which is observed even after strong exposures to oxygen. To answer those questions, experiments have been performed in which the extreme surface of the TiO_2(110) crystal was annealed by a hot filament, as described in Chap. 2.

[2] Oxygen affects the absolute counting rate, probably through the emission by the Lab_6 filament. A spectrum normalization is therefore required for comparison.

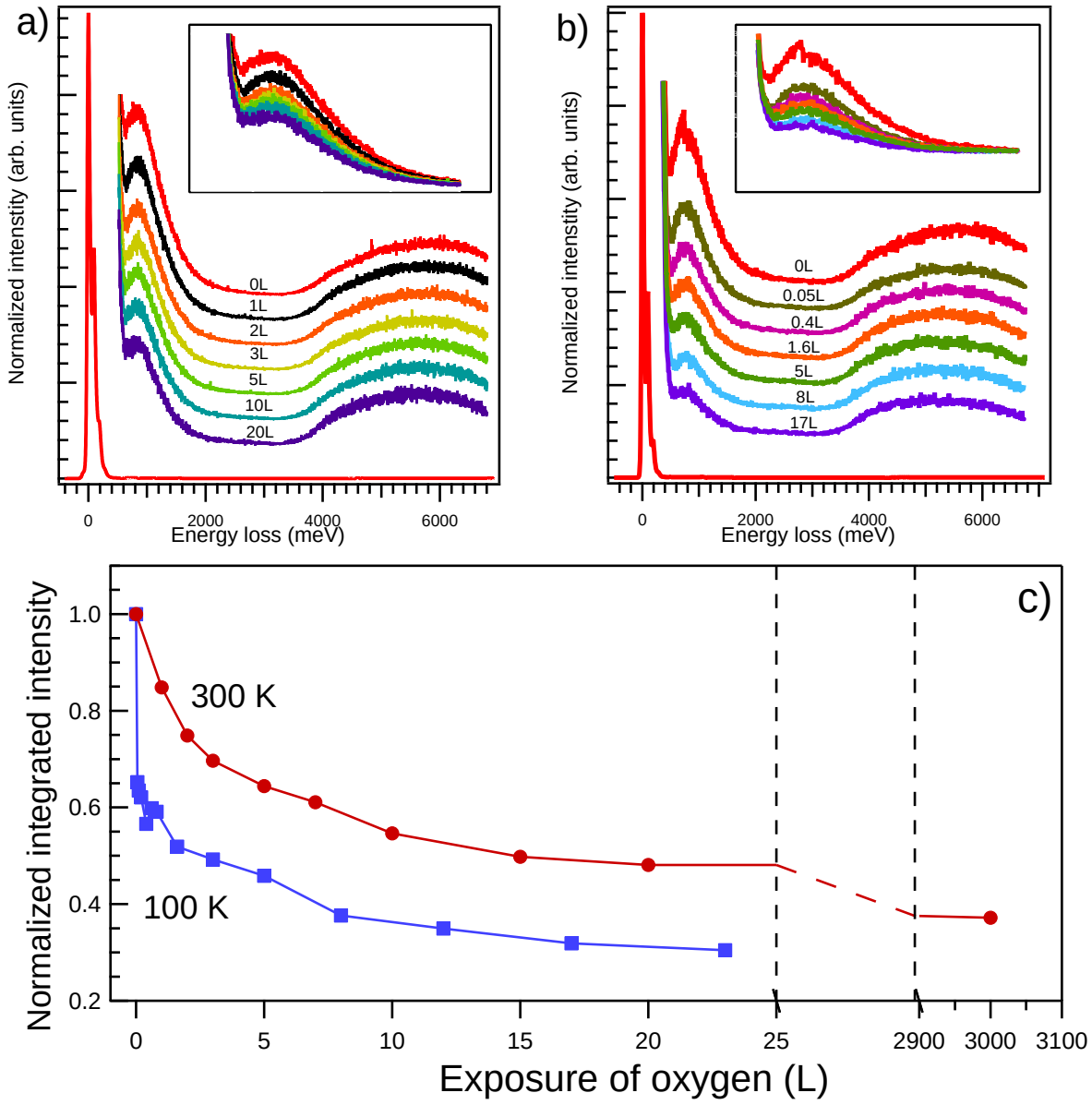

Figure 4.1: Specular EELS spectra (E_I = 38 eV, $\Theta_I = 60°$) recorded during the exposure of R-TiO_2(110) surface to molecular oxygen at a) 300 K and b) 100 K. Offsets are used to improve the readability of spectra (unshifted curves are presented in insets). Exposures (in Langmuir L) are indicated in figure. c) BGS integrated intensity normalized to the maximum value as a function of the oxygen exposure. Data points are derived from the spectra shown in Figs.-a,b. The inset shows the integrated intensity without normalization in range from 0 to 23 L. Oxygen heals nearly the same amount of BGS at 100 K and 300 K, although the process is much faster at 100 K at low exposure.

The idea is to overcome the thermal equilibrium between surface and bulk obtained when annealing from the back side of the sample.

4.3 Surface annealing

4.3.1 When the hot filament only allows surface annealing

When resistively heated, the filament placed in front of the sample in the HREELS chamber anneals the surface and, depending on its bias [3], can also illuminate it with electrons. Indeed, since both heat and electrons can generate defects on the $TiO_2(110)$ surface, the latter through the Knotek-Feibelman process [11, 12, 56, 57, 59], it is of strong interest to determine their respective role. The filament was placed at a distance of a fews mm in front of the grounded sample; in a such geometry, surface temperature up to 970 K could be reached (see Sect. 4.3.2 below). The sample was successively exposed during 10 s to this hot filament which was successively: (i) grounded, (ii) biased at −100 V leading to a total electron current detected on the sample in the range of 1 mA, or (iii) biased at +100 V to insure that absolutely no electrons are emitted as confirmed by the sample current. Between each treatment, the sample was exposed to a large amount of oxygen to recover the oxidized state. The key observation was that all treatments give exactly the same BGS intensity as observed by EELS. This clearly demonstrates that the BGS are only created by the heat radiation and not by electron bombardment. In the following, the filament was grounded during all the experiments and this treatment is referred to as surface annealing.

4.3.2 Surface temperature measurements

"Surface annealing" is of particular relevance since it is performed in conditions in which the surface can be probed by HREELS. The surface temperature can be determined through the Bose-Einstein distribution of losses and gains in the phonon region [61]. Their ratio is simply given by the Boltzmann factor $\exp(-\hbar\omega/k_bT)$ (where $\hbar\omega$ is the involved energy loss/gain, k_B the Boltzmann constant, T the sought temperature) as demonstrated in Fig. 4.2-a. The accuracy of this temperature determination is of the order of 1 K. This temperature corresponds to that of the near surface region; it is an average over the EELS probing depth for phonon loss, which typically amounts to a few nanometers (see Sect. 3.2.5). Stationary temperature conditions were achieved during those measurements since no evolution was observed over time, at least between two consecutive scans (one minute). No significant temperature rise was observed on the thermocouple of the manipulator owing to its large thermal capacity. Fig. 4.2-b shows the temperature evolution as a function of the filament power, when the filament-sample distance is kept constant (here at $d = 22$ mm). Fig. 4.2-c shows the reciprocal that is to say the change of temperature as a function of the filament-sample distance at constant filament power (here 23 W). Values of distances and powers are specific to the present work. As shown in Figs. 4.2-b,c reproducible surface temperature can be achieved by selecting the couple distance-power. Temperatures cannot be measured beyond 650 K (Fig. 4.2-c) because, when the filament is too close to the sample, it perturbs too much

[3] The potential drops accross the filament is around 10 V.

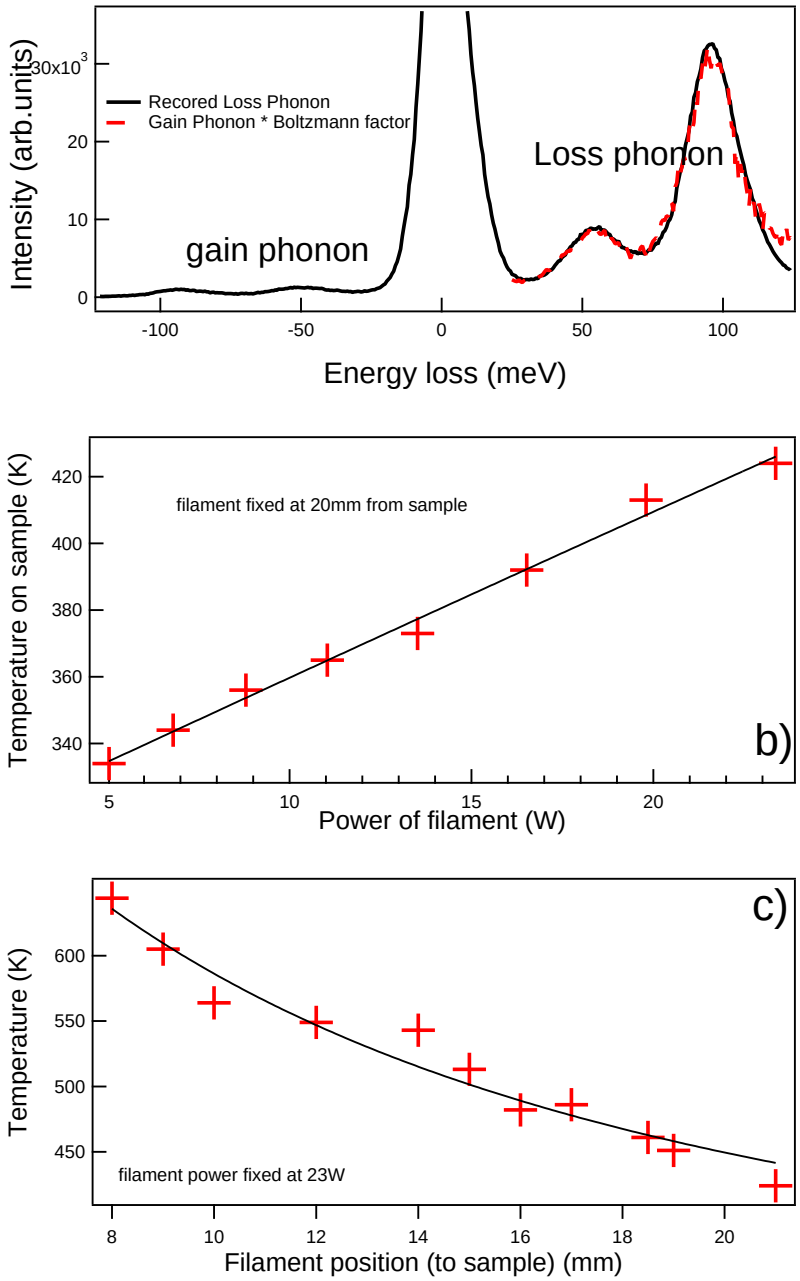

Figure 4.2: Surface temperature of $TiO_2(110)$ when exposed to the hot filament: a) experimental phonon spectrum with losses overlapped with gain counterpart multiplied by the Boltzmann factor to determine temperature; b) surface temperature versus filament power for a sample-filament distance of $d = 20$ mm; c) surface temperature versus distance d at fixed filament power of 23 W (crosses correspond to measurements; the line is the fitted curve). Distances and powers given in those figures are indeed specific to the present set-up but reproducible.

the trajectory of the HREELS electron beam to have a reasonable counting rate. To estimate the surface temperature above 650 K when the filament is close to the surface, the measured data were extrapolated by using the power law dependence $T(K) = \alpha/(d-\beta)^2+300$ expected from flux conservation; the fitted curve is shown in Fig. 4.2-c. Afterwards, two specific annealing temperature were chosen: (i) 420 K where creation of O_b-vac cannot happen, but diffusion of Ti_{int} is possible [14, 42, 49, 50, 55]; (ii) around 1000 K where the creation of O_b-vac is systematically observed by bulk annealing [2–8]. The applied sample treatment will be denoted hereafter A-TiO_2-T-t where T stands for the stationary temperature and t the annealing time. Two durations were compared: (i) short $t = 10$ s corresponding to a flash

annealing and (ii) longer ones $t = 100$ s. All surface annealing treatments were performed on samples that had been oxidized by saturating amounts of oxygen at room temperature. The saturation term, although abusive in the light of Fig. 4.1, means an amount of oxygen enough to heal the largest part of the BGS intensity (*i.e.* at least 20 L at 300 K).

4.3.3 BGS due to Ti interstitial diffusion for a surface temperature of 420 K

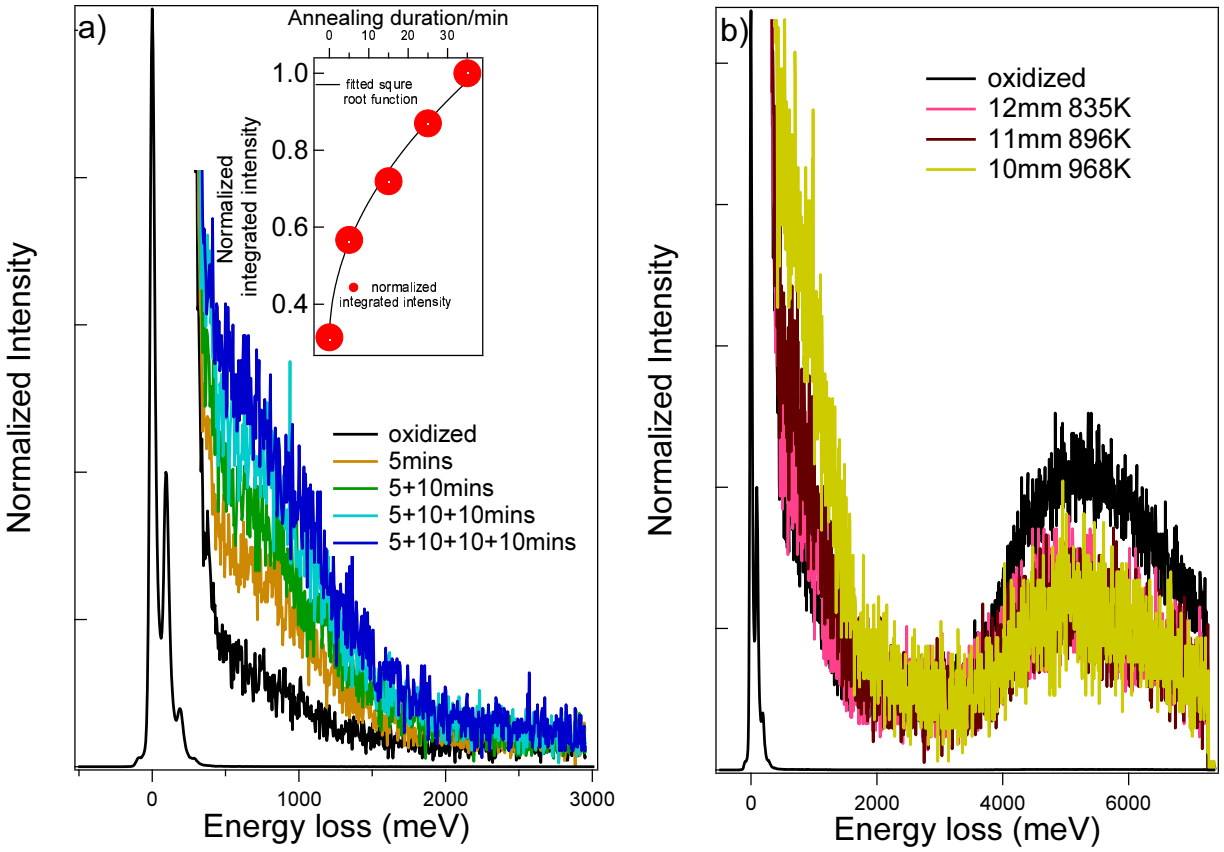

Figure 4.3: Formation of BGS upon annealing of R-TiO_2 exposed to 20 L of O_2: a) Annealing at 420 K during different durations; the inset shows that the integrated intensity displays a square-root temporal dependence which points to a diffusion mechanism, b) Sequential annealing during 10 s at increasing temperatures by changing the distance between filament and sample; BGS starts increasing at 835 K as estimated by fitted curve Fig. 4.2-c).

BGS changes upon annealing time was examined when the surface was heated at 420 K (Fig. 4.3-a). The BGS starts growing in intensity only after a few minutes of this mild annealing but the rise slows down with time as shown in Fig. 4.3-a. In fact, the BGS integrated intensity follows a square-root behaviour with time (inset of Fig. 4.3-a), which is indicative

of a diffusion mechanism. This observation is consistent with the existence of a temperature gradient between surface and bulk that drives the creation of BGS via diffusion of titanium interstitials; indeed, this is the only possible mechanism at 420 K [14, 42, 49, 50, 55], a temperature at which the direct formation of oxygen vacancies by annealing is completly excluded accordingly to all previous measurements [2–8].

4.3.4 BGS due to a combination of Ti interstitials and oxygen vacancies at various surface temperatures

Afterwards, change in BGS intensity was investigated by short heat flash during 10 s of the surface at different temperatures. This latter was controlled by adjusting the distance between the filament and the sample at constant power. The corresponding EELS spectra shown in Fig. 4.3-b demonstrate that defects start being created at 835 K (estimated through the fitted curve Fig. 4.2-c). The higher the temperature the higher the BGS. Under such annealing conditions, BGS can be due either to O_b-vac and/or to Ti_{int}. According to C. M. Yim *et al.* [12], the linear relationship that is observed between the BGS intensity as measured by UPS and the O_b-vac population as determined by STM suggests that BGS are mainly due to surface vacancies. This point is checked below during the study of water adsorption (Sect. 4.4).

4.3.5 Toward a defect-free TiO_2(110) surface

Fig. 4.4 shows the BGS change after successive surface annealings and, between each annealing step, an exposure to oxygen at saturation (> 20 L) to heal BGS. The impact on the BGS integrated intensity after each step of the treatment is plotted in the inset. In line with the above observation of the diffusion of Ti_{int} upon surface annealing (Sect. 4.3.3), the decrease in the residual BGS, that is observed at the end of exposure to oxygen of surfaces annealed at increasing surface temperatures, suggests that this residual is due to Ti_{int}. In line with Refs. [16–18] the suggested mechanism is that adsorbed oxygen withdraw excess charge from Ti_{int} close to the surface during adsorption at 300 K, reacts with Ti_{int} to regrowth TiO_{2-x} islands on the surface, and enhances Ti_{int} outwards diffusion from deeper layers as the surface temperature is increased during the annealing step. Deeper Ti_{int} are affected at higher temperatures. More precisely, in step. 1, the A-TiO_2-420K-10s treatment is able to create BGS at the surface of a R-TiO_2 exposed to more than 20 L of oxygen at room temperature. However, in step. 3, after the harsh A-TiO_2-970K-10s treatment of step. 2 followed by oxidation, the mild A-TiO_2-420K-10s annealing cannot create BGS anymore, because A-TiO_2-970K-10s had already driven all Ti_{int} that are shallow enough to the extreme surface of the sample where they were healed by oxygen. The subsurface is consequently depleted with Ti_{int} at an increasing depth which, after exposure to oxygen and healing of the surface BGS, results in a progressive weakening of the BGS signal due to Ti_{int}.

Therefore, cycles of surface annealing and oxidation, can lead to a "perfect" surface, which is defect-free at least over the probing range of EELS *i.e.* of a few nanometers (see Sect. 3.2.5). However, this does not mean that BGS created by surface annealing are only due to Ti_{int}.

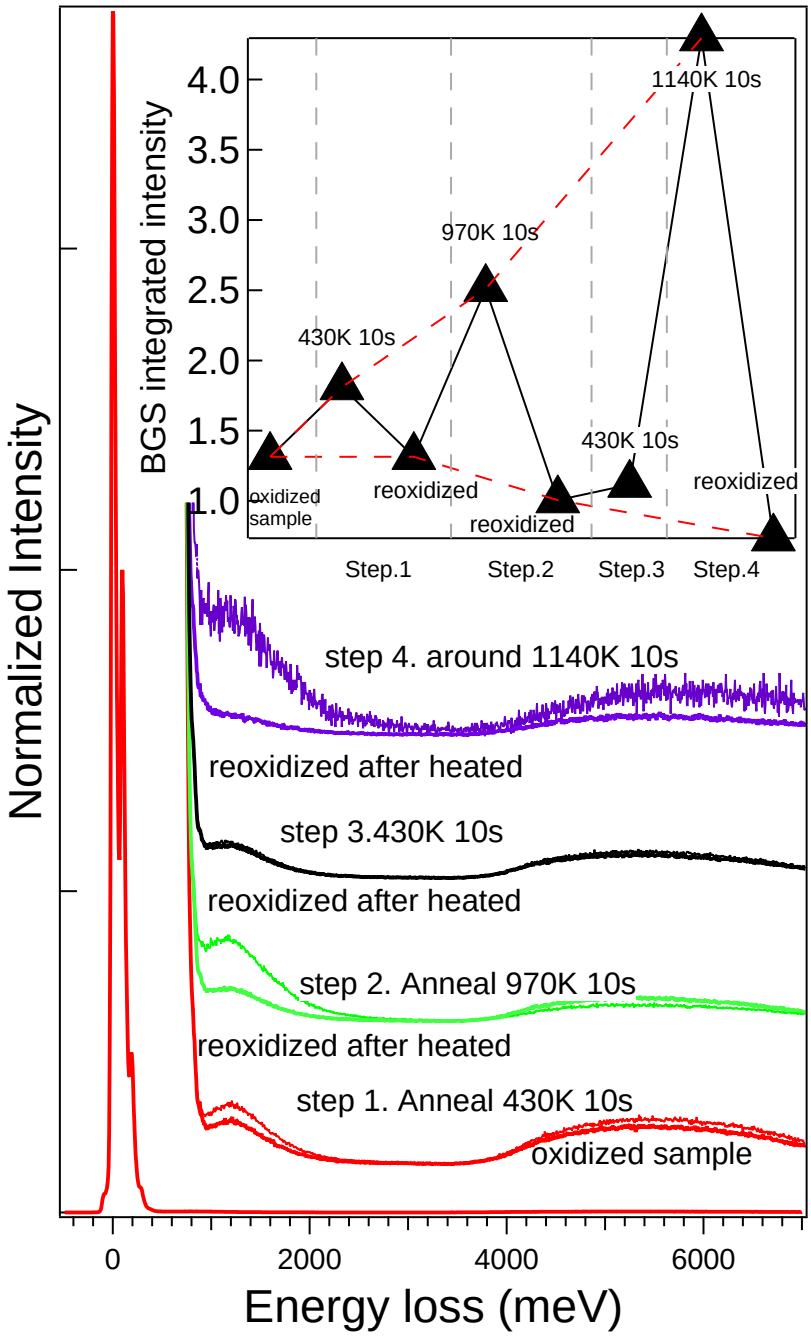

Figure 4.4: A-TiO_2-T-10 annealing/oxidation treatments at increasing surface temperatures: change of BGS after successive annealings at increasing temperatures, each annealing being followed by an exposure to oxygen at 300 K up to saturation. The resulting integrated BGS intensities are shown in the inset. Notice that, while the annealing treatments result in increasing BGS intensity, oxidations that follow tend to progressively decrease the residual BGS intensity.

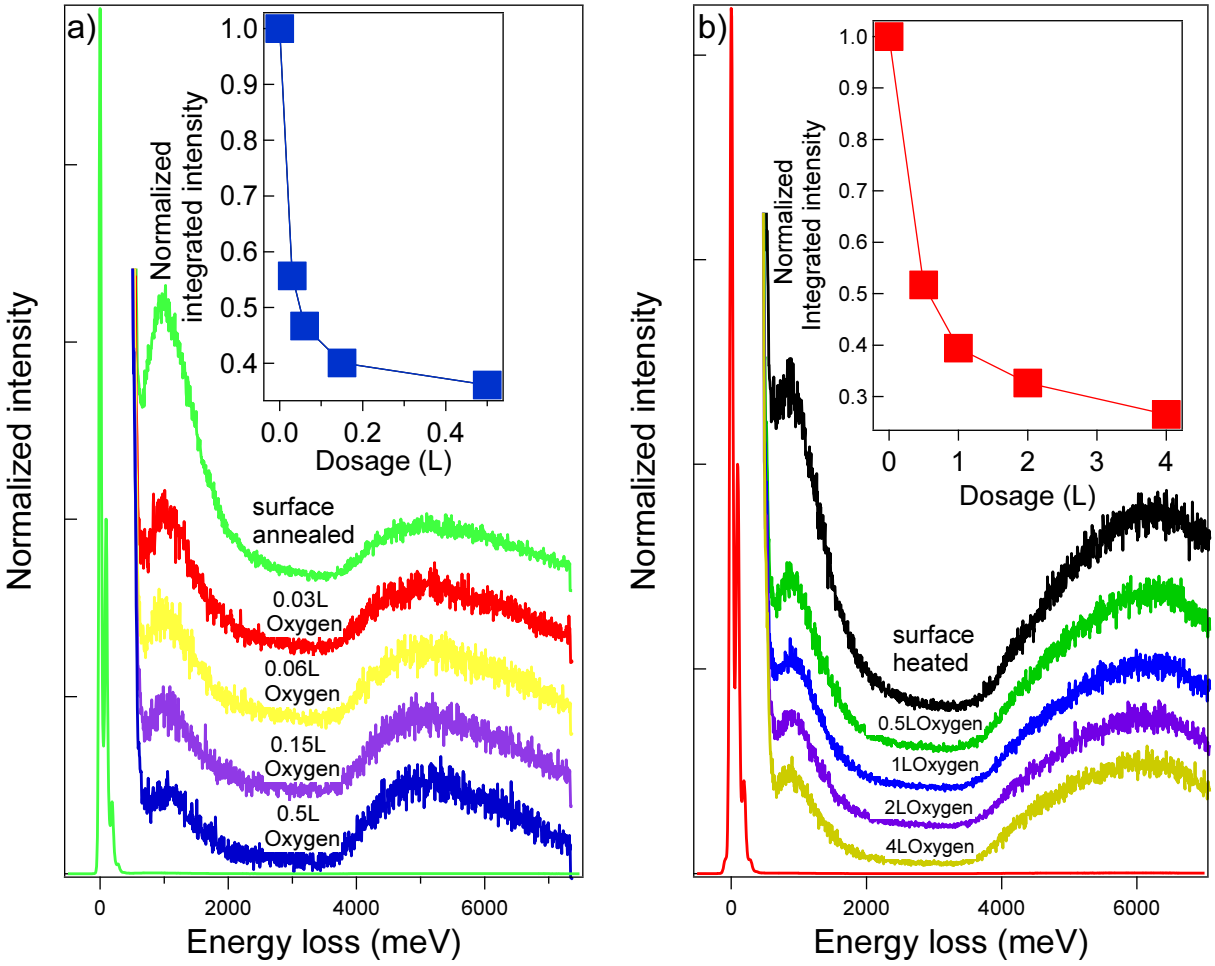

Figure 4.5: Exposure to oxygen of BGS that are formed by a A-TiO_2-970K-10s treatment: a) at 100 K and b) at 300 K. Normalized integrated intensity of BGS upon oxygen exposure is plotted in the inset. BGS decreases rapidly upon oxygen exposure, most of BGS created by surface annealing are removed by 0.15 L of oxygen at 100 K, by 1 L of oxygen at 300 K.

Fig. 4.5 shows the healing by oxygen of BGS that result from A-TiO_2-970K-10s treatments, which correspond to very short annealing at 970 K. Dosage as low as 0.15 L of oxygen at 100 K after this annealing treatment could remove most BGS. Such a dramatic healing process suggests that this is a very surface process and, therefore, that most BGS created by a short flash at high temperature are mainly due to O_b-vac. This observation is consistent with UPS/STM results [12]. Observations made at room temperature are quite similar although, as expected, higher exposures are required to heal the defects.

Notably, BGS are now assumed to come from either oxygen vacancies or titanium interstitials, with similar fingerprints. The issue is fully discussed in Chap. 5 while the present chapter focuses more on surface/bulk defects.

4.4 How water adsorption can heal BGS associated with surface vacancies ?

While BGS of TiO_2 are commonly healed by exposure to oxygen, most authors [6, 7] claim that BGS are insensitive to water in agreement with *ab initio* calculations [53, 54]. But in our experiments, a sizeable decrease in BGS intensity can be observed upon exposure of R-TiO_2 to water vapor, as shown in Fig. 4.6. The same phenomenon appears in the EELS study of Ref. [93] but it will be demonstrated that water does heal vacancies only under electron beam of appropriate energy.

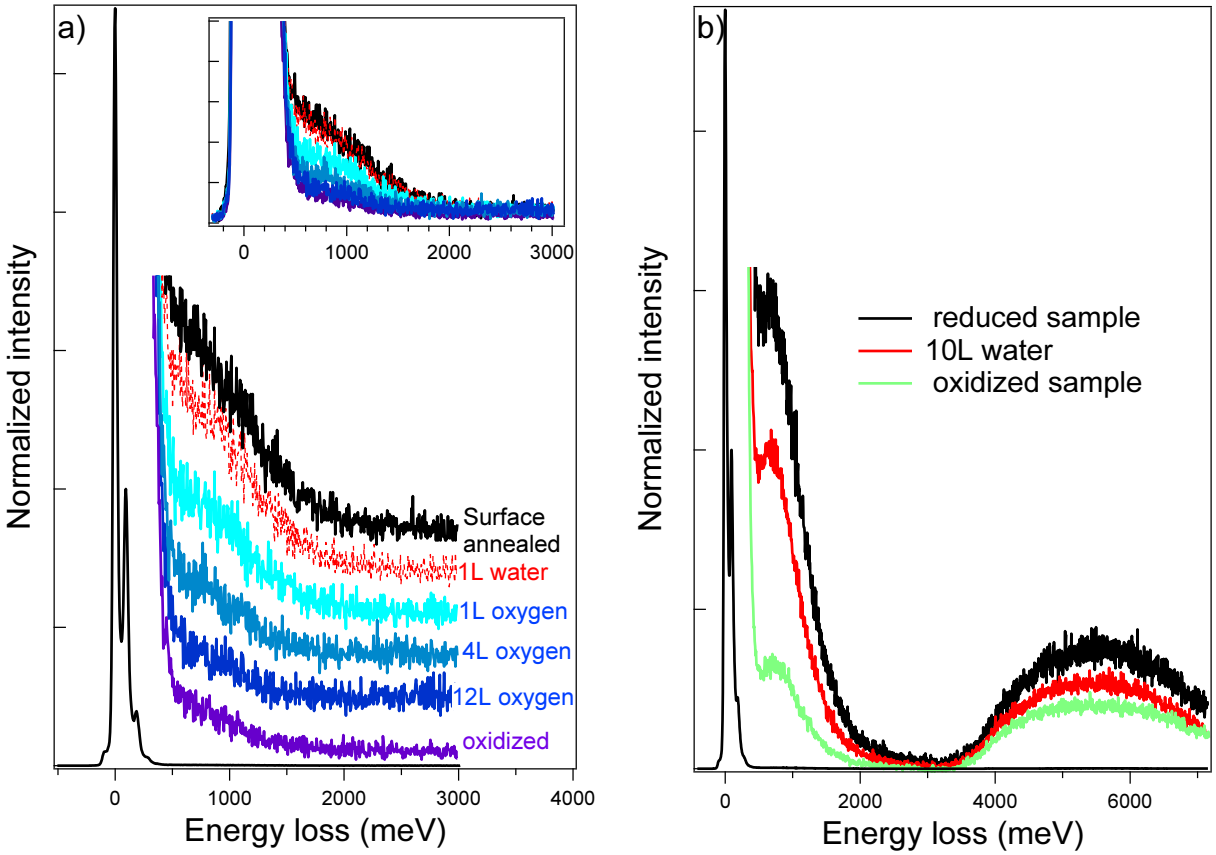

Figure 4.6: a) Exposure to water and oxygen under electron radiation at $E_I = 38$ eV of BGS created by A-TiO_2-420K-2100s treatment. Water hardly changes BGS of A-TiO_2-420K-2100s while oxygen remove it rapidly. Inset shows curves without offset. b) Decrease in BGS intensity observed upon water exposure of R-TiO_2(110) at 300 K under an electron beam of $E_I = 38$ eV.

It is well documented that water dissociates on oxygen vacancy sites at room temperature to give rise to OH groups in vacancy sites and protons on neighboring bridging oxygen atoms [2–8]. Now, if the protons are desorbed, the final result would be oxygen atoms filling vacancies, the same result as with molecular oxygen but without adsorbed oxygen O_{ad}. In

Fig. 4.6-b, the used beam energy of $E_I = 38$ eV, is far higher than the threshold of 22 eV for the electron stimulated desorption of H^+ from OH adsorbed at the TiO_2(110) surface [57]. To verify this assumption, an impact energy of 22 eV was used; the reason why lower beam energy was not selected is that, in this case, the BGS signal overlaps with a strong background due to multiple phonon losses which prevents its analysis. The experiments performed on a O_b-vac-rich surface (after a A-TiO_2-970K-10s treatment) at $E_I = 22$ eV and $E_I = 38$ eV are compared in Fig. 4.7. When the EELS beam energy is 38 eV, water nearly heals all the BGS, while at 22 eV, water exposure hardly perturbs BGS at all. These parallel experiments prove that water can heal defects with the help of an electron beam of relevant energy; at 22 eV, there is still a slight decrease of BGS intensity because this is the onset of the electron stimulated desorption of H^+ with a tiny (but finite) cross section.

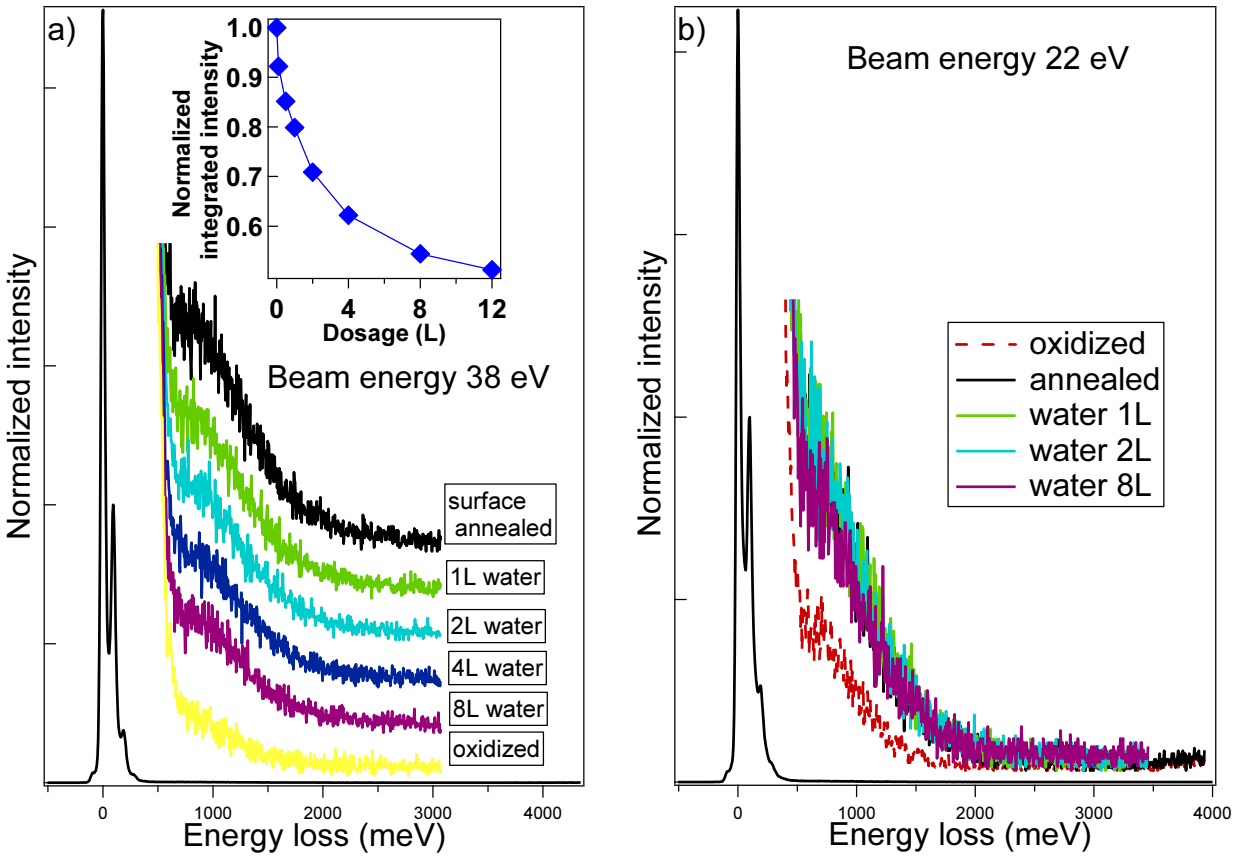

Figure 4.7: Exposure to water of BGS created by a A-TiO_2-968K-10s treatment, under electron irradiation at: a) $E_I = 38$ eV and b) $E_I = 22$ eV. Change of integrated intensity of BGS is shown in inset. Exposure to water removes nearly all BGS with electrons at 38 eV, but hardly changes BGS with 22 eV electrons.

The data recorded upon exposure to water of surfaces mildly annealed at 420 K (A-TiO_2-420K-2100s) are shown in Fig. 4.6-b. Water has nearly no effect on the BGS created in

this way, even under electron radiation of 38 eV, meanwhile oxygen heals all those BGS. As discussed before, the only possible process upon annealing at 420 K is a diffusion of Ti interstitials. The lack of reactivity of water in the present case supports the fact that the treatment A-TiO_2-420K-2100s only creates subsurface defects that cannot be healed by water. Now, let's go back to water adsorption under an electron beam at 38 eV after a A-TiO_2-968K-10s treatment (Fig. 4.6-a). The healing of almost all BGS is consistent with the fact that a short but powerful surface annealing creates nearly only O_b-vac since BGS associated with sub-surface Ti_{int} would not react in this way. Moreover, it rules out the possibility that the healing of BGS in Fig. 4.7-a is due to oxygen species generated by electron stimulated dissociation of molecular water, because in that case, water should be able to heal interstitials also, like oxygen.

The spectra of Fig. 4.6-a show that, even with the help of an electron beam, BGS still can not be completely removed upon water exposure. What is left is BGS due to subsurface defects that can be healed by oxygen. From the present data, it appears that both surface vacancies and titanium interstitials contribute to BGS, in a proportion which much depends on the way the rutile surface is prepared. Upon harsh surface annealing, surface vacancies dominate, while after mild annealing at 420 K, interstitials become the major source of BGS. Both types of defects play an important role in the surface reactivity in reduced TiO_2(110). It is possible to control the formation of specific types of defects by appropriate treatments (surface annealing, electron bombardment). This extremely flexible behaviour certainly explains why the origin of BGS in the surface region of TiO_2(110) is so vividly debated.

4.5 Creation of oxygen vacancies by electron bombardment

4.5.1 Creation of only oxygen vacancies

Electron bombardment (see Sect. 2.2.3) is an other method to create defects [11,12,56,57,59], yet the discussion about whether it creates only O_b-vac is still alive [12,147]. It was performed *in situ* at a flux of around 1 μA.cm^{-2} and beam energy of 75 eV [4] with the gun in front of the sample. It must be noticed that the present electron bombardment is not accompanied by a surface annealing owing the gun geometry. Therefore, what it probed is the effect of the electron bombardment alone. Its effect was tested herein by dosing oxygen on the E-TiO_2 surface. Fig. 4.8-a shows the decrease of BGS upon oxygen exposure at 300 K. More than 15 L of oxygen are needed to recover the spectrum as it was before electron bombardment. For the same experiment at 100 K (Fig. 4.8-b), an exposure of 1 L of oxygen is enough to get rid of all BGS created by electron bombardment, which clearly demonstrates that this method only creates surface O_b-vac. This result agrees with the conclusions of Refs. [12, 58].

In Fig. 4.8-c, a O-TiO_2 (see Sect. 2.2.3) was annealed at 500 K for 10 mins by the furnace located at the backside of the sample to let Ti_{int} diffuse to near surface region. Then

[4] A value close to the optimum of electron stimulated desorption of oxygen [57].

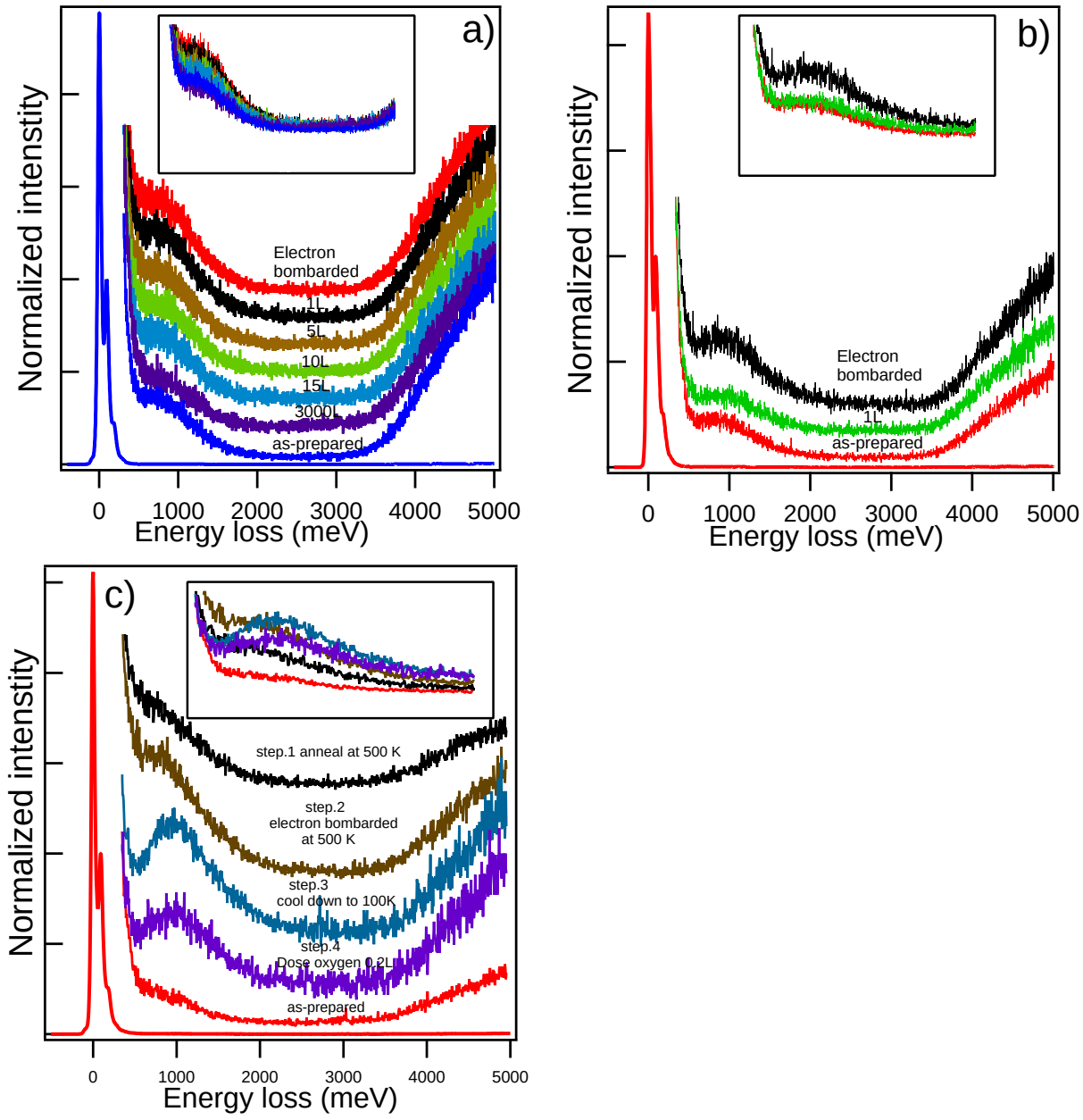

Figure 4.8: Interaction of oxygen with BGS of E-TiO_2 at a) 300 K and b) 100 K. c) Interaction of oxygen with BGS of a sample which was prepared by electron bombardment of an annealed O-TiO_2 (see text) (insets are spectra without any offset); low exposure to oxygen remove very quickly the BGS created by electron bombardment, but hardly react with BGS created by the annealing.

the sample was cooled down to 100 K and electron bombarded during 1 hour with a beam energy of 75 eV and a current intensity of $\sim 1\mu$ A/cm^{-2}. Finally, it was exposed to oxygen. Despite the difference in shape of the BGS spectra, it can be seen that only 0.2 L of oxygen are required to recover the intensity of that BGS had after annealing, but before electron bombardment. With this observation, it is reasonable to say that, at 100 K, low dosage of oxygen will interact with surface defects only. The result confirms that electron bombardment that are performed herein only create surface vacancies.

15 L of oxygen are needed to heal all O_b-vac on E-TiO_2 at 300 K while less than 1 L is required at 100 K. The reason is the strong temperature dependence of the balance between the mobility of physisorbed oxygen on the surface, the probality for oxygen molecules to be adsorbed on vacant sites and the life time of physisorbed oxygen. The latter quantity is likely much larger at 100 K than at 300 K.

Finally, it can be noted that the amount of BGS created by electron bombardment in the present conditions is much smaller than that created by surface annealing or reduction (Fig. 4.9).

4.5.2 The limited efficiency of electron bombardment

The electron bombardment has been tested with a fixed flux of electrons (1μA.cm^{-2}; 75eV) but the BGS intensity was observed to saturate after only a few tens of seconds. Longer exposure to the electron beam did not change the BGS intensity even up to hours (not shown). In K. Onda *et al*'s work [58], a small population of defects was also obtained using similar bombardment conditions. However, much larger population of O_b-vac was obtained by N. G. Petrik *et al.* [11] with a focalised raster gun using a much larger local flux and therefore lower exposure time but with the same total integrated dose. In the process of electron bombardment, the beam does not only create vacancies, but also heal the newly created vacancies with the help of the water vapour residual pressure (as demonstrated previously in Sect. 4.4) which is systematically found in UHV chambers. The final population of O_b-vac is limited by the competition between the two processes. This explains why the vacancy population created by electron bombardment tends to rapidly level off in our tests and that different authors obtain different results despite a similar total integrated flux (*i.e.* number of electrons per unit of surface [11, 58]). However, this process seems to be completely inefficient [5] under the EELS electron beam because of a much lower cross section at the scanning energy [57] and a total current much lower than with the bombardment gun.

[5] BGS intensity is stable during hours of scan.

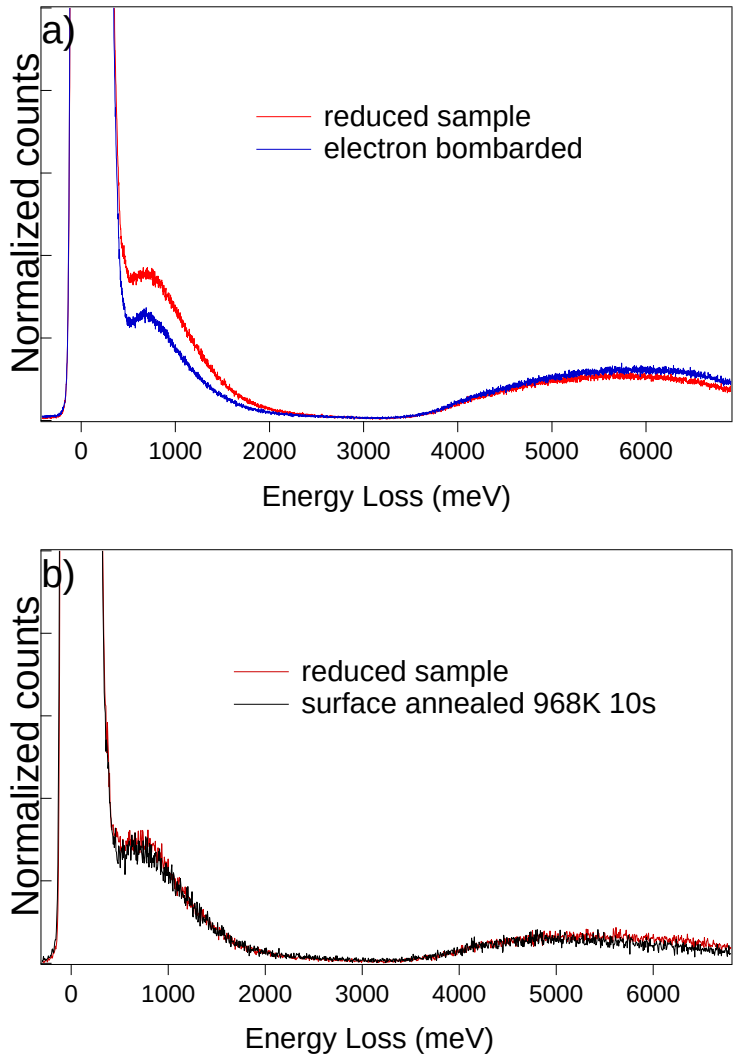

Figure 4.9: BGS intensity comparison a) between reduced sample R-TiO_2 and electron bombarded one E-TiO_2 and b) between R-TiO_2 and A-TiO_2-968K-10s. Taking BGS on reduced sample as reference, surface annealing creates a lot more BGS than electron bombardment in the present conditions.

4.6 Out-of-specular EELS spectra and the profile of excess electrons

4.6.1 BGS recorded from different probing depths

Despite the interest of the issue, nothing is known about the BGS profile through the surface region of TiO_2. Indeed, BGS are mostly studied by photoemission, a technique whose probing depth was never clearly discussed in the conditions in which BGS are analysed. In EELS, the probing depth is inversely proportional to the modulus of the electron wave vector transfer parallel to the surface $k_{\|}$ as discussed in depth in Sect. 3.2.5. It can be changed by varying the detection angle to gain information from depths of the order of magnitude of 1 to 100 Å below the surface; it is given by $|k_{\|}/k_I| = |\theta_E \sin\Theta_S + \sin\Theta_I - \sin\Theta_S|$ where $\theta_E = \hbar/2E_I$ is the opening of the dipolar cone and Θ_I, Θ_S are the incident and detection angle (see Fig. 3.1). It is worth reminding again (Sect. 2.3.3) that, in EELS, electrons can undergo two major processes which are distinguished through the range of interaction: (i) dipole scattering is a

long distance interaction in which most electrons are scattered in specular direction; the loss cross section is expected to strongly decay with the detection angle; (ii) impact scattering is a short distance process; compared to dipole scattering, it is more like a non-angular dependent background.

Fig. 4.10-a and -b present EELS spectra of R-TiO_2 and O-TiO_2 collected at different detection angles Θ_S at fixed incidence Θ_I [6]. Due to the fast decay of the dipolar loss cross section with Θ_S that impacts strongly the quasi-elastic peak and the phonon losses, out-of-specular spectra have been systematically normalized to the high energy part of inter-band transitions losses which are even in specular condition already dominated by impact scattering and very surface sensitive (see Fig. 3.25-$E_I = 38$ eV).

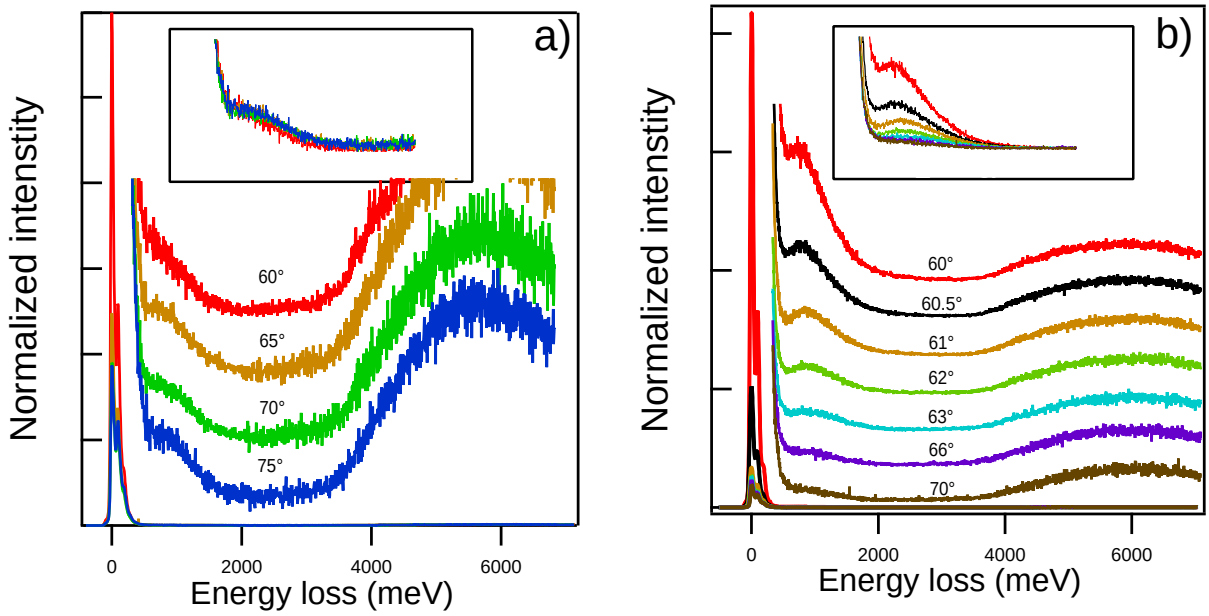

Figure 4.10: Out-of-specular EELS spectra for selected detection angles Θ_S (with respect to the normal to the surface) at fixed incidence $\Theta_I = 60°$: a) O-TiO_2 and b) R-TiO_2. Insets show the same spectra without any offset. Normalization is applied on the interband transition losses. Note that, while a strong angular dependence was found in the case of R-TiO_2, O-TiO_2 spectra hardly change as a function of the detection angle.

On O-TiO_2, on which nearly all surface defects and subsurface defects were healed by annealing under oxygen, although there was still some remaining BGS intensity there, nearly no change of BGS intensity has been observed, even in very surface sensitive conditions. The present findings indicate (i) that dipolar and impact contribution are of similar intensity in O-TiO_2 and (ii) that the residual BGS is coming from very surface defects, therefore ruling out Ti_{int} as expected from the depletion induced by the surface preparation applied to

[6] Rotating the analyser is more accurate in our set-up than rotating the sample

O-TiO_2. Obviously, those defects are not oxygen vacancies. An hypothesis could be step edges since regrowth of TiO_2 islands on the surface is known to happen during such a surface reoxidation [16–18, 23, 48, 49]. This point requires further investigations.

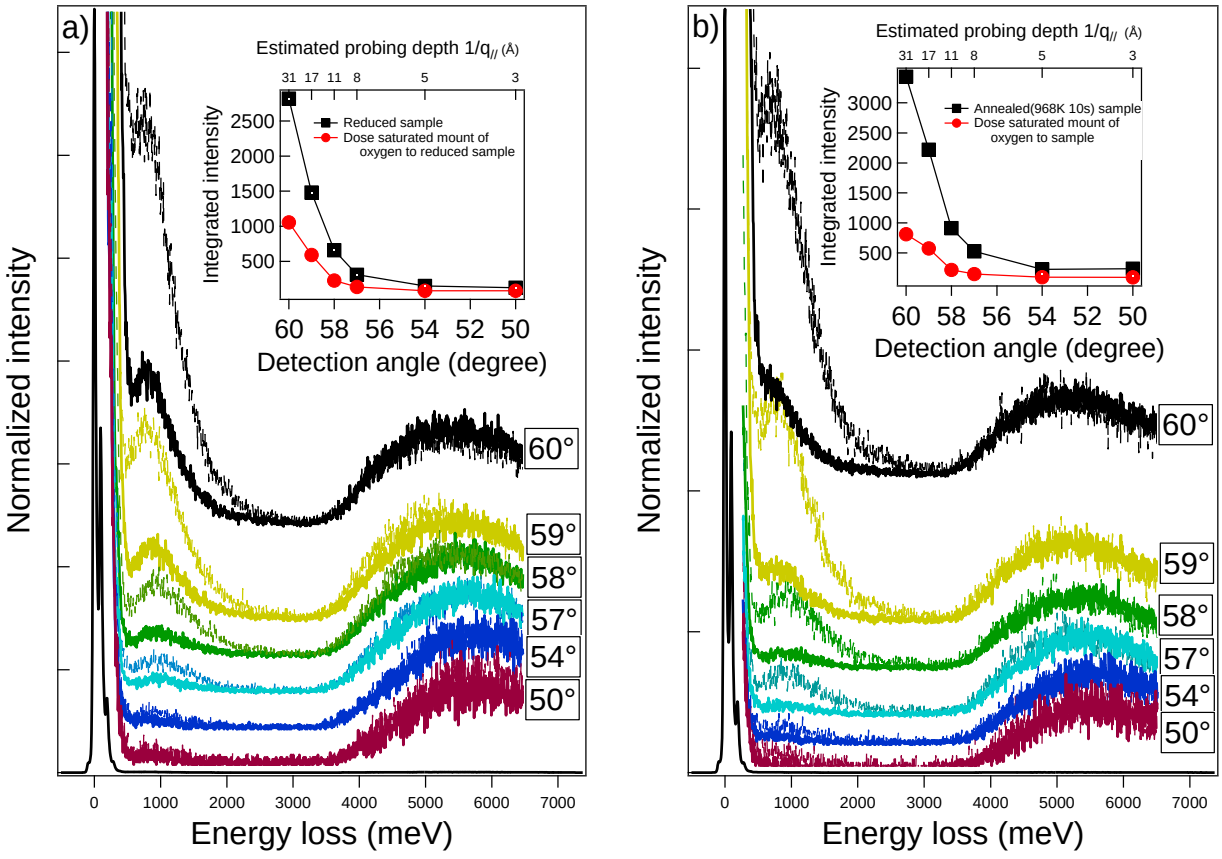

Figure 4.11: Comparison of probing depth effect on BGS of different samples before (dash line) and after (solid line) exposure to oxygen at saturation: a) R-TiO_2 and b) A-TiO_2-970K-10s. Insets present BGS integrated intensities as a function of detection angle Θ_S (bottom scale) or probing depth $d_p = 1/k_{\|}$ (top scale). BGS intensities of both samples decrease as probing depth decreases, but much slower on A-TiO_2-970K-10s. BGS can not be detected at large angles in both cases *i.e.* for very sensitive conditions.

Conversely, in experiment on R-TiO_2 (Fig. 4.10-b), a strong angular dependence indicates that dipole scattering dominates the loss process. Fig. 4.11 presents EELS spectra of R-TiO_2 and A-TiO_2-970K-10s at different detection angles, before and after healing by oxygen. In both cases, the BGS intensity decreases when the detection angle goes away from the specular direction. Before oxygen treatment, although the BGS intensities of both samples decrease as probing depth decreases, the decreasing rate of A-TiO_2-970K-10s (Fig. 4.11-b) is slower than that of R-TiO_2 (Fig. 4.11-a). In addition, at each detection angle, oxygen reduces more BGS intensity on A-TiO_2-970K-10s than on R-TiO_2. These two observations suggest that BGS on A-TiO_2-970K-10s are mostly from surface defects and that subsurface contribution from Ti_{int}

is involved in R-TiO_2. Finally, on both R-TiO2 and A-TiO_2-970K-10s (Fig. 4.11), at largest detection angles, when spectra are very surface sensitivity ($d_p \simeq 3$ Å) and impact dominates, there is no intensity of BGS at all. This demonstrates that, although O_b-vac is located at the surface as seen by STM, the excess charge due to O_b-vac is actually not located at the extreme surface, as suggested by the photoemission data of P. Krüger and coworkers [52, 145] and *ab initio* electronic calculations [34, 54] combined with STM measurements [22, 53]. Finally, the removal of the residual BGS by changing the probing depth indicates that those residual states are mainly associated with bulk defects that are too deep to be healed by oxygen though they are detected by EELS in specular direction.

4.6.2 Qualitative description of the profile of excess charges

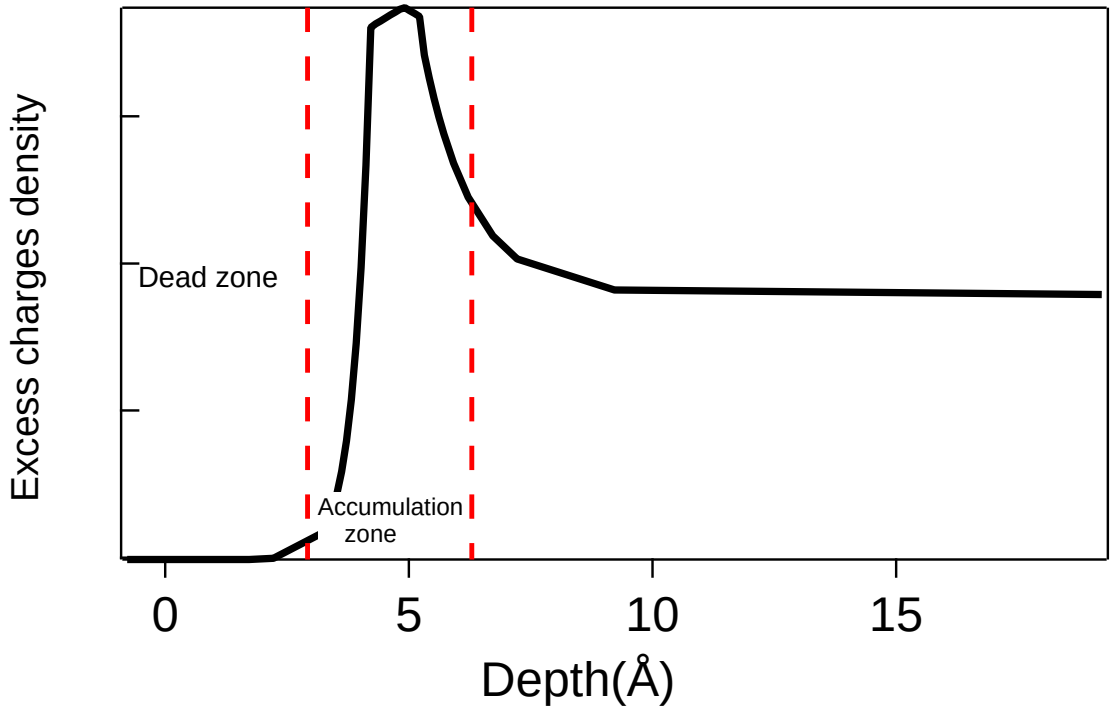

Figure 4.12: Profile of excess charges due to BGS through the surface region of the rutile crystal, as suggested by our experimental data. From surface to bulk, are found a charge-free surface, a charge accumulation zone which has the highest state density and then a progressive decrease of the density towards an asymptotic value.

The results from BGS angular dependence experiments together with all the experiments described in this chapter provide a schematic idea of the distribution of the excess charges through the R-TiO_2 surface region (Fig. 4.12). Excess charges are not located at the very surface where are found the O_b-vac. Below, in the first subsurface layers, there is a charge accumulation zone which has the highest state density and to which electrons from O_b-vac are transferred. Deeper, the contribution from BGS become lower and lower and finally reaches a

bulk average value in a way that depends on the sample oxydo-reduction history. This profile agrees with previous findings of the literature [22, 52–54], at least on the localisation of the excess charges from O_b-vac in the subsurface. This kind of profile will be used to reproduce quantitatively the (HR)EELS experimental data using the dielectric theory in Chap. 5.

4.7 Conclusion

In this chapter, various surface treatments applied to the $TiO_2(110)$ surface were compared in terms of band gap state intensity, namely vacuum annealing (R-TiO_2), surface annealing by a hot filament (A-TiO_2), electron bombardment (E-TiO_2), intense oxidation at high temperature (O-TiO_2), exposure to either oxygen or water vapour at different temperatures (100/300 K). Some of these are original (surface annealing in particular). By analysing their effects on the observed BGS in EELS, both in specular and out-of-specular geometries and at several beam energies, it has been possible (i) to demonstrate that both O_b-vac or Ti_{int} contribute to the BGS and (ii) to find conditions in which one or the other is the unique defect of the rutile surface and (iii) to observe the reactivity of these defects with either oxygen or water. Finally, a schematic profile of excess electrons through the surface region of $TiO_2(110)$ was proposed.
The strength of the study mostly came from the combination of data, the specific opportunities offered by the EELS technique and the novelty of the interpretations.

CHAPTER 5

EXCESS ELECTRONS IN REDUCIBLE TiO_2 RUTILE: DUAL BEHAVIOUR OR COEXISTENCE OF TRAPPED AND FREE STATES ?

5.1 Position of the question

Besides the question on the major contribution to the BGS addressed in Chap. 4, the localisation of excess electrons in TiO_2, whatever the way they are created (reduction upon annealing, doping with foreign elements, light excitation, etc...) is still a controversial issue, all the more than it is polymorph dependent. The issue is of paramount importance in the (photo)catalytic processes at its surface [1, 2, 8]. Excess electrons are formally associated to a Ti^{3+} oxidation state through the filling of Ti 3d orbital (see Eqs. 2.1). The observed high conductivity in defective rutile [25], or more precisely the very high electron mobility and its decrease with temperature above 100 K, is compatible with "free-like" carriers in the conduction band. This seems contradictory with the apparent deep character of the defect level at 0.8-1 eV below the Fermi level as observed by photoemission [10, 12, 20, 52, 130], electron energy loss [21, 89, 131], occupied density of states in scanning tunneling spectroscopy [15, 22], near infrared optical absorption [23, 132, 133] and electron spin-resonance [24]. Those spectroscopies suggest that native defects behave as filled donors while lower activation energies (a few tens of meV) are deduced through temperature dependent transport measurements [25, 31, 148, 149]. Analysis of resonant photodiffraction of the BGS [52, 145] on TiO_2(110) located excess electrons (due to surface oxygen vacancies or due to deposited alcaline metal) on subsurface titanium with a dominant contribution from the first layer under Ti_{5c} (see Fig. 2.5). In parallel, standard Density Functional Theory (DFT) predicts shallow levels which are resonant with the conduction band and strongly delocalized over several titanium atoms [150]. But once having corrected the weakness of the Kohn-Sahm electronic spectrum by resorting to more advanced *ab initio* methods (DFT+U, hybrid functional, PBE+U etc... [33, 34, 43–45, 54, 151–156]) to

localize the charge [1], a much deeper level is obtained in close agreement with spectroscopic findings.

Therefore, there is still a blurred landscape in the literature about (i) the coexistence of trapped and free-electron like states associated to different defects that would account respectively for spectroscopic and transport measurements or (ii) a dual behaviour of excess electrons depending on the way they are excited, a question which points to the problem of electron localisation. This dual behaviour is related to the polaronic distortion that goes with the filling of the Ti 3d orbitals to form Ti^{3+}. An electronic charge in an highly polarizable medium such as TiO_2 (see Sect. 3.2.2.3) causes the atoms which surround it to relax to screen it. The quasi-particle consisting of an electron coupled to the lattice distorsions in its immediate surrounding is called a polaron, an electron dressed by phonons, as initially named by L. Landau [157]. Depending on the extent of lattice relaxation and the range of interaction, the polaron behaviour [134, 136] is categorized into small (Holstein model [158]) or large (Fröhlich model [159]). While large polarons may travel as free-like carriers with an enhanced effective mass due to the phonon cloud, small polarons are prone to hopping transport from one site to the other [134, 136]. The main difference lies in the temperature dependence of the mobility which increases with phonon population and temperature for a small polaron in constrast to the large one. In rutile, excess electrons of TiO_2 compete between free-like carriers in the conduction band and polaronic configurations. In fact, TiO_2 rutile seems to lie typically in a regime of intermediate coupling [25, 32] with a behavior that changes with temperature [22]. Clearly, from transport measurements, hoping dominates below 4 K [30, 31]. However, above 250 K [25], conduction is well explained by donor centres completely exhausted into a conduction band with an activation energy of few tens of meV while Hall mobility decreases by one order of magnitude [25].

Regarding the contradiction between spectroscopic and transport behaviours, a beginning of answer came recently in some theoretical papers [22, 26, 27, 153] [2] which pinpointed the question of vertical and thermodynamic transitions related to the polaronic character of the defect states [22, 26, 27] (Fig. 5.1). This was already stressed much earlier in the case of photoemission from doped transition oxides by A. Fujimori *et al.* [28].

Vertical (or optical) transitions, such as probed by photoemission or optics/EELS, retain the starting state polaron strained geometry as if the lattice atoms were frozen during the time scale of the experimental probe; the level seems filled and deep. Thermodynamic transition states involved in electron transport implies the continuous relaxation of polarization and an activated migration of the polaron from one site to an adjacent one. The level appears as much shallower (Fig. 5.1). Fig. 5.2 shows the results from the most extensive calculations [26] of the levels for both bulk O-vac and Ti_{int} in rutile and anatase. Although sensitive to the U-parameter, the diagram suggests a much stronger donor character in anatase than in rutile for the defects.

An other possibility is that the polaronic configuration competes with free-like or more delocalized electrons, the difference with a large polaron being quite subtle [22, 27]. Recent

[1] Even on purpose through the adjustable Hubbard repulsion U.

[2] In particular Ref. [26].

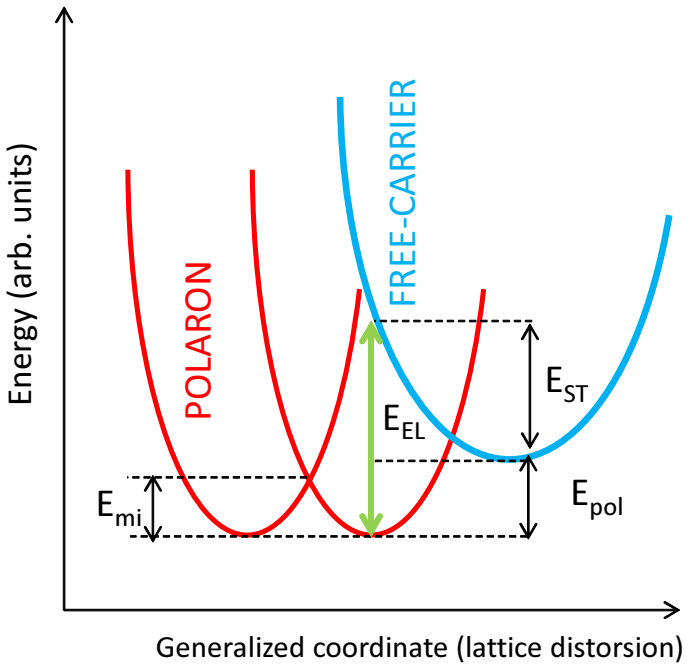

Figure 5.1: Schematic configuration diagram showing the energy as a function of the lattice distortion for polaron and delocalized electron configurations. E_{st} is the strain energy to deform the lattice, E_{el} the energy gained by localizing the electron on a Ti site in such a distorted lattice and E_{pol} is the formation energy defined as the total energy difference between the polaronic and fully delocalized free-carrier solution. $E_{el} = E_{st} + E_{pol}$ is the energy measured in photoemission/EELS. E_{mi} corresponds the migration or hoping barrier between localized polaronic configurations. Interpreted from Refs. [22, 27, 33, 137].

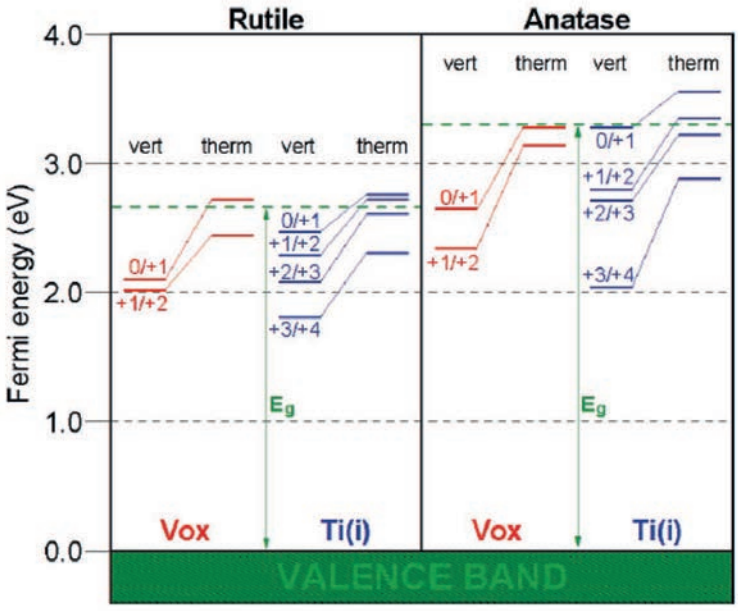

Figure 5.2: Position of the vertical and thermodynamic transitions levels of excess electrons associated to bulk oxygen vacancy and titanium interstitials in rutile and anatase. The calculated gap corresponds to the green dotted line. Calculation have been performed in DFT-LSD-GGA+U with a local spin density generalized gradient approximation, plus Hubbard U correction. From Ref. [26]

ab initio electronic calculations [22, 27] from C. G. Van de Walle and G. Kresse groups (using self-consistent U-values and combined with STM measurements) on rutile and anatase led to the conclusion that the polaronic configuration is slightly more favourable than the delocalized one in rutile in constrast to anatase. In bulk rutile, a stabilization energy of $E_{pol} = 0.15$ eV (Fig. 5.1) was found with a migration barrier of $E_{mi} = 30$ meV along the c-axis and $E_{mi} = 9$ meV perpendicular to it [27,33]. The polaron may also form some complexes with the associated defect which asks the question of the formal charge of defects (V_O, $V_O^{\cdot}$, $V_O^{\cdot\cdot}$ or $Ti_i^{\cdot\cdot\cdot\cdot}$, $Ti_i^{\cdot\cdot\cdot}$, $Ti_i^{\cdot\cdot}$, $Ti_i^{\cdot}$, Ti_i) which depends on the actual position of the Fermi level [26,27,153]. On the TiO_2(110) surface, *ab initio* molecular dynamics simulations [22, 34] or more static calculations [53,54] predict a fast diffusion among many polaronic configurations very close in energy but with a strong weight in the first layer in agreement with photodiffraction [52,145]. An apparent activation energy of around 70 meV was found in the molecular dynamic simulations of Ref. [34]. Finally, it seems that hydroxylation of the surface (OH_b) does not change the conclusions drawn regarding excess electrons provided by surface vacancies O_b-vac [53,54].

The difficulty to predict energy levels, the lack of temperature effect and the smallness of energy differences make wise regarding predictions of electronic calculations compared to experimental observations. But, on the other hand, up to now, no real experimental evidence that reconciles *simultaneously* transport and spectroscopic measurements has been provided. The aim of this chapter is to use the ability of the (HR)EELS to probe both types of excitations with a surface/bulk sensitivity in order to discuss the question of the dual behaviour of excess electrons. In a first part, experimental proofs on the existence of carrier-related excitations in the (HR)EELS spectra will be given through the quasi-elastic peak shape, its temperature dependence and the phonon line shape (Sect. 5.2.1). By using the simplified profile of dielectric function suggested in Sect. 4.6.2, experimental results will be fitted (Sect. 5.2.2) using the dielectric theory developed in Chap. 3. The obtained results about surface and bulk excess electrons will be discussed in the light of the existing literature (Sect. 5.3).

5.2 (HR)EELS from reduced TiO_2(110) surface

5.2.1 On the existence of carrier excitations

Since reduced TiO_2 is a n-type semiconductor in terms of electrical transport, direct evidences of conductivity induced by the sub-stoichiometry are expected in the EELS spectra as demonstrated in Chap 3.

5.2.1.1 Effect of oxygen exposure

The evolution of band gap states and phonon/quasi-elastic losses upon exposure to molecular oxygen at 100 and 300 K was scrutinized both in high (Fig. 5.3-a,c) and low resolution (Fig. 5.3-b,d) on a vacuum annealed R-TiO_2(110) surface (see Sect. 2.2.3). All of the measurements were performed with the incident beam normal to the bridging oxygen row *i.e.* normal to the c-axis of TiO_2. Great care was taken to keep exactly the same apparatus settings and

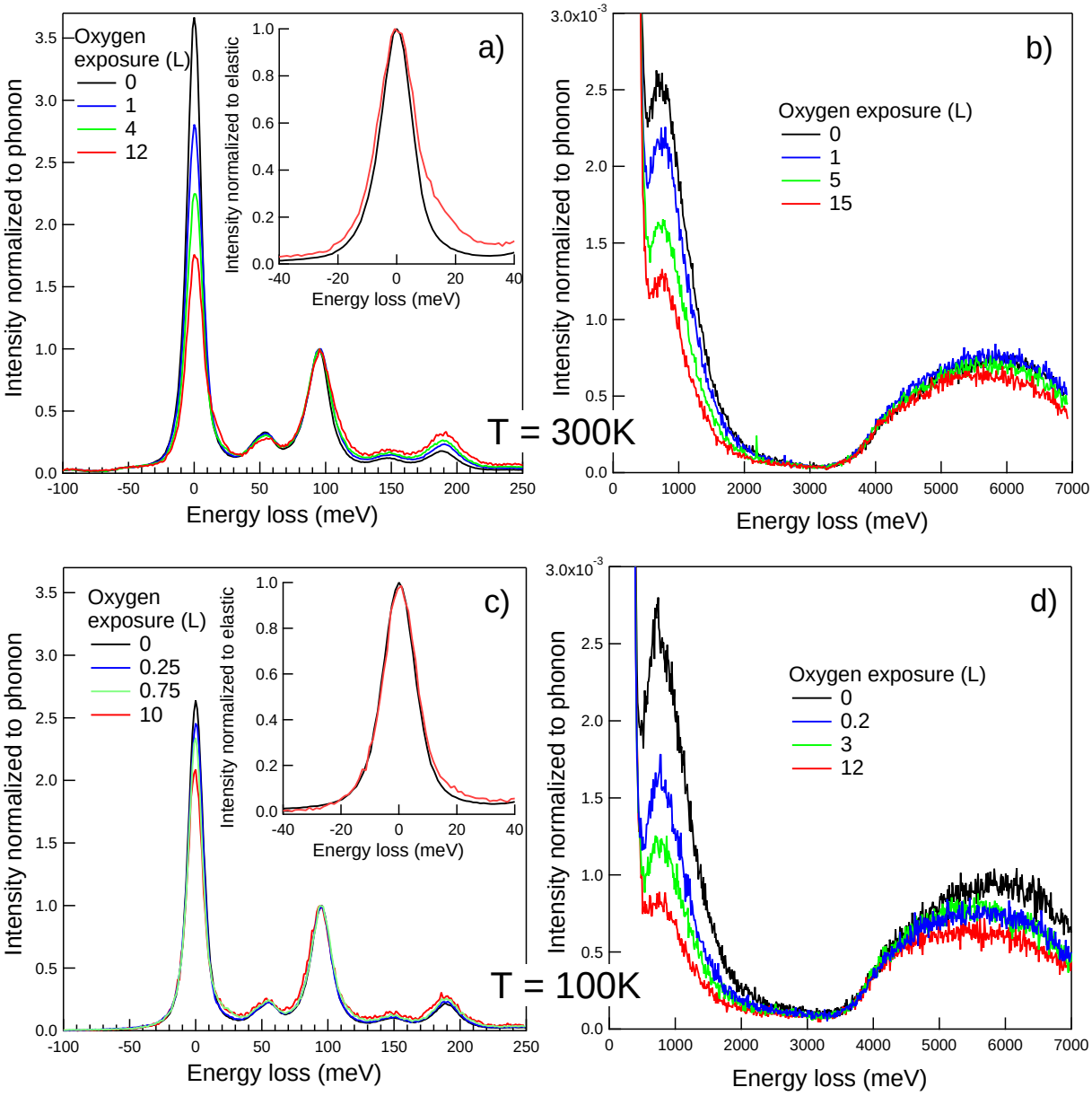

Figure 5.3: Effect of molecular oxygen exposure on a)c) HREELS (E_I = 7.5 eV; FWHM of quasi-elastic of 13 meV) and b)d) EELS (E_I = 38 eV; FWHM of quasi-elastic of 50 meV) spectrum of a vacuum reduced R-TiO_2(110) surface held at a)b) 300 K and c)d) 100 K. Intensity has been normalized to the main phonon peak at 95 meV. The decrease of elastic peak intensity is more apparent in high than in low resolution. The shape of the quasi-elastic peak before and at the end of exposure is shown in inset after normalization to its maximum. Data have been acquired for an incident beam perpendicular to the bridging oxygen rows.

resolution function all along the measurements despite the decrease of couting rate [3]. The quasi-elastic peak, three single phonons, their multiple and combination modes, the band gap states due to defects and the interband transitions appear upon increasing the energy loss. Since absolute counting rate is affected by gas exposure, data have been normalized to the maximum of the most intense phonon line around $\hbar\omega_{sph,3} = 95$ meV. Three noticeable features appear on the raw data:

(i) a decrease of the band gap state intensity around 0.8-1 eV down to a residual value that can not be further reduced even after intense exposure (up to 3000 L, not shown, see Chap. 4 for a full analysis),

(ii) a decrease of the relative intensity of the quasi-elastic peak with respect to the phonon losses, in particular $\omega_{sph,3}$,

(iii) a more apparent high energy asymmetry of the elastic peak around 10 meV that replicates at the foot of $\omega_{sph,3}$ (Fig. 5.3-a,c-insets),

(iv) a slight variation of the intensity of interband transitions,

(v) a sharpening of the BGS peak with temperature.

The sizable variation of the relative intensity of phononic excitations and elastic peak was tentatively interpreted in the work of M. A. Henderson to a variation of the phonon oscillator strengths due to oxygen adsorption which is unlikely owing to the large depth sensitivity for such losses (see Chap. 3.2.5). In the light of the simulations that were perfomed in Chap. 3 and later on by using dielectric fits, this finding will be reassigned to a modulation of the conductivity of the near surface and the disappearance of the band gap states due to the healing of surface defects. In passing, if electron stimulated desorption of H is avoided by selecting the rigth beam energy (see Chap. 4), no change in (HR)EELS spectra is observed when the surface is exposed to water although this latter dissociates to form bridging hydroxyls [6, 7]. This confirms that OH groups do not perturb the electronic configuration of the surface as shown by *ab initio* calculations [53, 54].

5.2.1.2 Quasi-elastic peak: shape and temperature dependence

By using a spectral restoration algorithm to improve apparent resolution [35] (Chap. 3 and Annex Chap. 7), it was stressed that the asymmetry of the quasi-elastic peak could be compatible with the existence of surface plasmon excitation at an energy of around 10 meV (Figs. 10-11 of Ref. [35]). All phonon and plasmon combination modes, were detected in the resolution-enhanced spectra at positions predicted by dielectric simulations including free-like carriers.

However, elastic peak asymmetry and broadening due to spectrometer lens settings [61, 66] could be misinterpreted as a surface excitation (see Eq. 16 of Ref. [35] - Chap. 7 or Eq. 3.11). But this hypothesis could not explain a change of elastic peak shape upon gaz exposure as

[3] Probably due to the interaction of O_2 with LaB_6 filament.

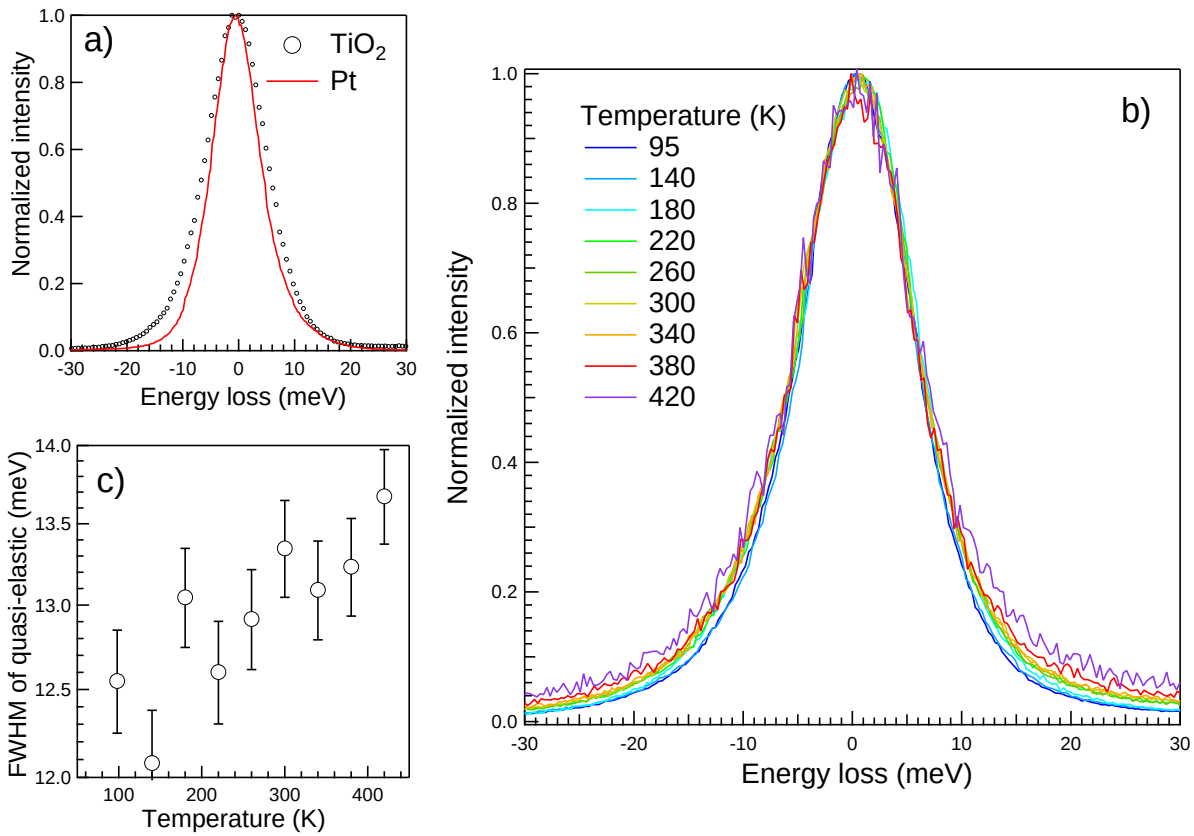

Figure 5.4: a) The quasi-elastic peak shape of a vacuum reduced R-TiO_2(110) compared to that of Pt(111) (FWHM of 10 meV), b) its evolution and c) FWHM upon increasing temperature from 95 K to 420 K.

observed in insets of Fig. 5.3-a,c since apparatus settings were kept constant. To settle the question, the quasi-elastic peak shape of R-TiO_2(110) and Pt(111) surface were compared with similar spectrometer lens settings and pass energies (Fig. 5.4-a). The metal elastic peak can be considered as a good estimate of the apparatus function although roughness and electron-hole excitation broadening may bias it. The apparent extra-broadening of 2.5 meV on the FWHM of the elastic peak for TiO_2 is compatible with the existence of a carrier excitation in the range of a few tens of meV accordingly to Fig. 3.14. Furthermore, the temperature dependence of the quasi-elastic was carefully analysed by keeping the same spectrometer settings and by compensating only from the thermal drift of the sample position. Data acquired (Fig. 5.4) from 95 K to 420 K shows a slight but reproducible temperature broadening of more than 1 meV. Accordingly to the previous simulations (Fig. 3.17), no temperature dependence is to be expected from stoichiometric titania or from BGS alone. The order of magnitude of the broadening, of its temperature dependence and of the expected surface plasmon frequency around 10 meV match well the case $n/m^* = 10^{19}$ cm^{-3} with poor damping (see fits below for an accurate determination). Finally, the assignment of the quasi-elastic asymmetry to the existence of a combination phonon mode at $\hbar\omega_{sph,2} - \hbar\omega_{sph,1} = 9.2$ meV is to be ruled out, not

only through simulations which predict a poor intensity, but also because this latter alone is insensitive to gas exposure and should disappear at $T = 100$ K at variance to observations (see inset of Fig. 5.3-c). All these findings point to the existence of a temperature dependent excitation in the quasi-elastic peak with a profile that is modified by oxygen adsorption.

5.2.1.3 Phonon line shape

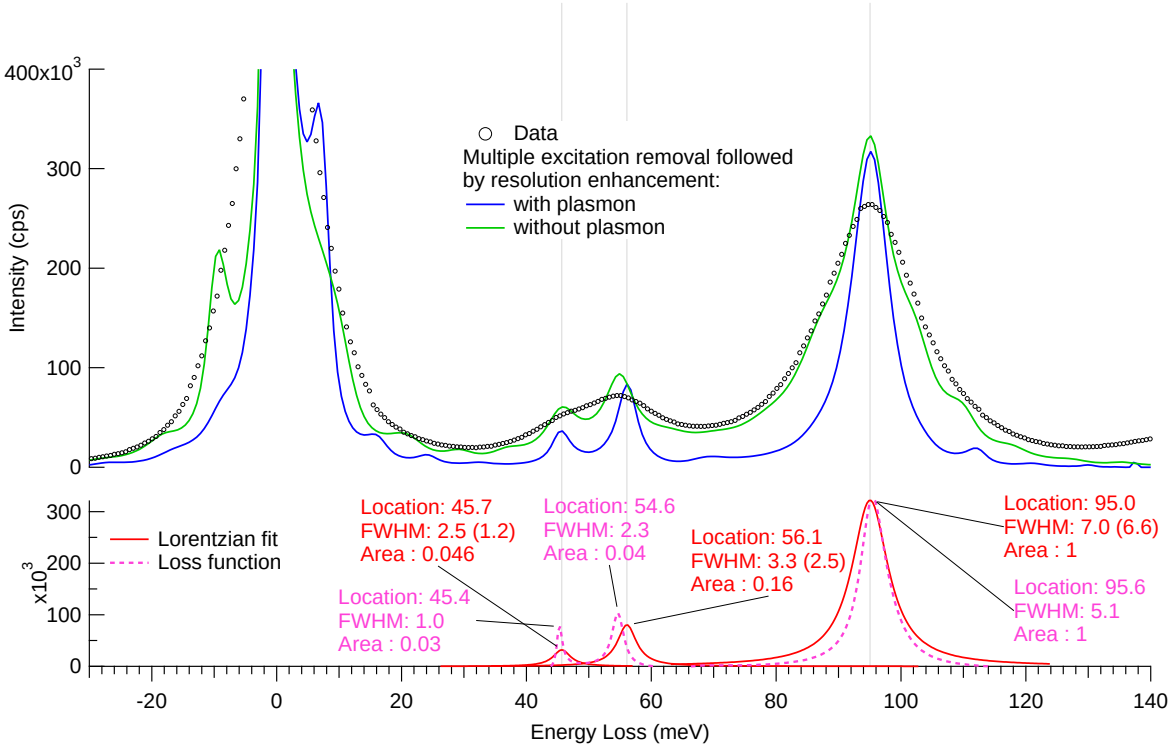

Figure 5.5: Effect of multiple excitation removal followed by resolution enhancement using the semi-blind Lucy-Richardson algorithm (see text) on an HREELS spectrum at 98 K (circles). The quasi-elastic peak shoulder is treated as an actual excitation (blue curve) or included in the resolution function (green curve) in the multiple phonon removal. Lorentzian fits (red curve) of the phonon peak (blue curve) is compared to the simulation of the loss function $\mathrm{Im}[1/1 + \epsilon_{\perp}(\omega)]$ without plasmon excitation (pink dotted curve). Values of peak position, FWHM and area relative to the phonon at ~ 95 meV are given in figure. The experimental value $\mathrm{FWHM}_{s,ph}$ given in parenthesis was obtained by removing the remaining elastic peak $\mathrm{FWHM}_a = 2.2$ meV: $\mathrm{FWHM}^2_{s,ph} = \mathrm{FWHM}^2 + \mathrm{FWHM}^2_a$.

An other indirect proof of the existence of carrier excitations is given by an accurate analysis of the phonon line shapes and positions compared to dielectric simulations (see Chap. 3). Although $\omega_{sph,3}$ peaks quite systematically around 95 meV on all vacuum annealed samples, shift and natural line widths of phonons appears more clearly on treated spectra. In Fig. 5.5,

multiple excitations have been removed using the Fourier transform technique of Ref. [98] (see Sect. 3.2.1.5) by excluding or not the plasmon shoulder in the definition of the apparatus function from the elastic peak. Thereafter, resolution has been enhanced through the semi-blind Lucy-Richardson algorithm developed in Ref. [35] (see Chap. 7) down to an elastic peak of FWHM of only 2.2 meV to avoid noise amplification. As shown in Fig. 5.5, nearly lorentzian single phonons peaks (red curve fits of the blue curve) are obtained as expected from theory (dotted pink curve; see Eq. 3.23) only if the quasi-elastic peak asymmetry is treated as a signal in multiple excitation removal. If not, the lorentzian shape is not recovered (green curve) by the algorithm. In passing, the found FWHM of the apparatus function is the same than on Pt(111) within 0.2 meV. The lorentzian fits of the single phonon excitations give the expected relative area between loss peaks calculated from tabulated dielectric loss function as developed in Sect. 3.2.2. But phonons are systematically shifted in frequency by a fraction of meV as predicted by a combined screening by BGS and carrier excitations. But, the obtained FHWMs of the single surface phonons are higher that expected even after subtraction of a apparatus function of 2.2 meV due the remaining elastic. A plausible explanation is the existence of a gradient of defects and of phonon shifts across the sample. Finally, despite the counting statistics, a shift of $\omega_{sph,3}$ could be observed at the earliest stages of sputtering/annealing of a native sample (Fig. 5.6). The limit value of 95 meV is reached very quickly after a few cycles below 1100 K or even only one at 1100 K as soon as the sample acquires a blue light color. No further shift could be achieved even up to TiO_2(110)-(1×2) reconstructed surface.

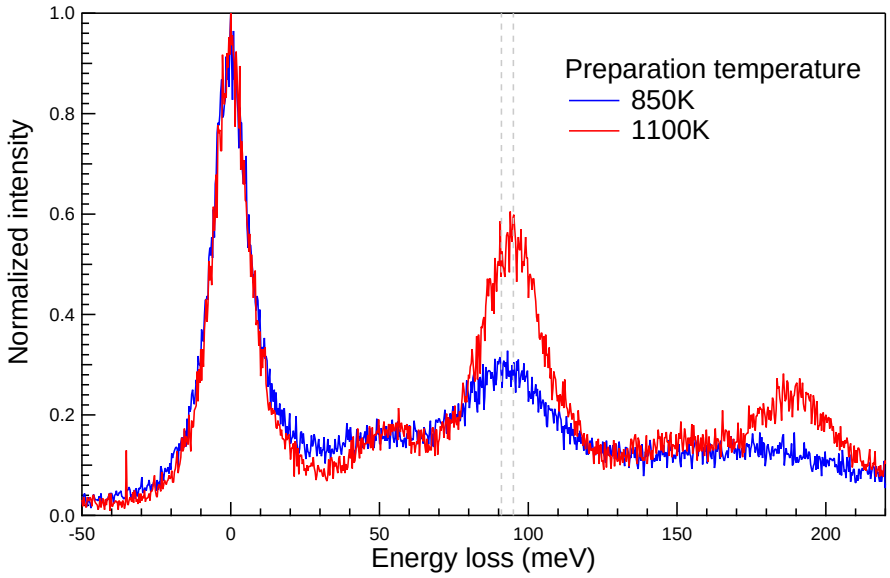

Figure 5.6: Phonon spectra of a TiO_2(110) sample at the earliest stages of preparation. The counting statistics of a few hundred counts is due to a poor surface reflectivity.

5.2.2 The profile of dielectric function for fits

To account for the well-documented healing of O_b-vac or OH_b groups [4] by molecular oxygen (see reviews [2–8]), data have been analysed within the dielectric theory using a simplified but representative profile of excess electrons associated to defects (inset of Figs. 5.7-a). Some hints about it have been obtained in the previous Chap. 4 from an analysis of the EELS BGS peak which combined surface annealing, exposure to gases and out-of-specular measurements. As demonstrated by photoelectron diffraction [52], filled-states STM imaging associated with modeling [22, 53], several first principle electronic structure calculations [22, 34, 54] and our EELS results (Chap. 4), excess electrons due to O_b-vac or OH_b are not localized on the defect but spread on six-coordinated Ti atoms in deeper layers with a strong weight on the first layer [22, 34, 52–54]. Therefore, before reaching a constant flat bulk behaviour, the assumed profile (inset of Fig. 5.7-a) is made of a 2.5 Å thick dead layer accounting for surface atoms and a layer of thickness t_S encompassing excess electrons due to surface defects. Only these surface defects are assumed to be sensitive to exposure and can be fully healed through a charge transfer to the oxygen molecule. From our previous findings (Chap. 4) and earlier photoemission measurements [14, 55, 58], BGS has a deeper bulk contribution, modeled here by a flat depth profile (coming most probably from Ti_{int}) although the majority of the experimental signal originates from surface defects [12, 13]. In this question about bulk-vs-surface contribution of BGS from photoemission, what was overlooked, is the escape depth of electrons [5] which overweights the surface contribution. In this respect, the present EELS measurements are more bulk sensitive (Fig. 3.24). Although simplified, the proposed scenario of excitation profile grasps the known main physics of electron spreading due to surface defects on TiO_2(110) and, more importantly, is able to reproduce the present experimental findings. The surface excess electrons are characterized on a dielectric point of view through their oscillator-like band gap states ($\Omega_{gs,S}, \omega_{gs,S}, \Gamma_{gs,S},$) and their Drude-like transport properties ($\omega_{P,S}, \Gamma_{P,S},$). In a similar way, ($\Omega_{gs,B}, \omega_{gs,B}, \Gamma_{gs,B}$) and ($\omega_{P,B}, \Gamma_{P,B}$) define the same quantities for the bulk counterpart. Attempts to fit data with flat profiles *i.e.* with only bulk excitations were unsuccessful to describe phonons spectra before exposure, especially the ratio of phonon/quasi-elastic peak intensity. This led to unreasonable detector aperture compared to expectation of Fig. 3.6.

Experimental spectra have been fitted with the dielectric theory developed in depth in Chap. 3 with the parametrization of the dielectric function of Sect. 3.2.2 and the approximate loss function $\xi(\omega) = \epsilon_{\perp}(\omega)$ [6]. Owing to the number of free parameters, the strategy was to fit first the EELS spectra (Figs. 5.7) which are less sensitive to phonon shifts and intensity variations due to a poorer resolution, starting from the highest exposure to obtain bulk values assuming that $\Omega_{gs,S} = 0$ (*i.e.* that all BGS have been healed in the surface layer); thereafter these obtained parameters were kept constant while fitting the surface values at lower exposure. During fit, a gaussian resolution function of 50 meV FWHM and a beam divergence of $\theta_c = 0.7°$ as determined by out-specular measurement on graphite were kept constant. Since BGS losses are several decades less intense than phonon losses due to sensitivity function (Fig. 3.24 and Sect. 3.2.1.2), the logarithm of the intensity was fitted to enhance the BGS

[4] A partial hydroxylation of the sample due to residual water can not be excluded.

[5] Which is unknown in the case of laboratory helium ultra-violet excitation.

[6] Beam is normal to oxygen bridging rows

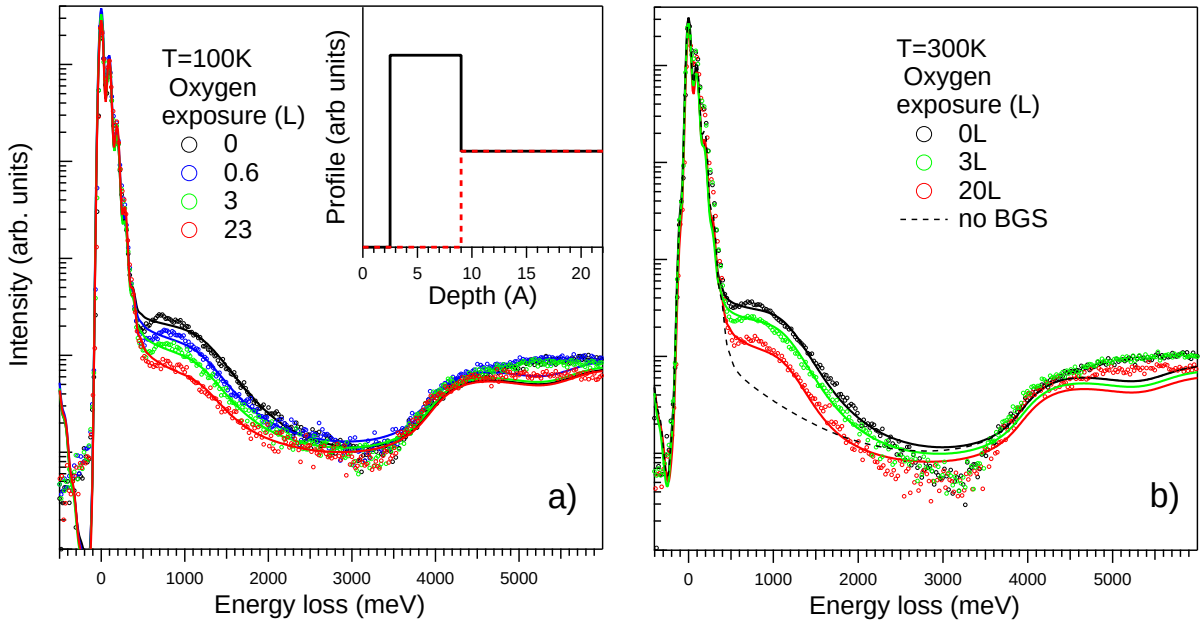

Figure 5.7: Experimental (circles) and fitted (lines) EELS spectra as a function of oxygen exposure at a) 100 K and b) 300 K. The inset shows the used profile of dielectric function for reduced (black full line) and oxygen exposed surface (red dotted line). The dotted line in Fig. b corresponds to a simulation without BGS contribution.

weight; but care was taken no to include interband transitions in the minimization process. In fact, the fit was limited to energies lower than 3 eV, in a range dominated by long range dipole interaction with negligible impact scattering (see Fig. 3.24). If simulations reproduce qualitatively the line shape of interband transitions (Figs. 5.7), they underestimate the experimental intensity and do not reproduce by any means the variation of intensity observed above the band gap upon reduction (Fig. 5.3-c,d). The surface sensitivity of EELS in this energy loss range (below $\simeq$ 10 Å ; Fig. 3.24) combined with a sizeable fraction of surface vacancies may induce a noticeable change of hybridization and explain this behavior. In passing, the EELS band gap which should be interpreted as the "surface" one accordingly to the probed depth, does not differ drastically from the bulk value [124] ($\simeq$ 3.1 eV at 300K; see simulations of Fig. 5.7) despite the reduction of coordination number of atoms at surface. This is in constrast to strongly ionic oxide for which the Madelung field mainly drives the band splitting [160]; the reason lies in the more covalent character of the bonding in titanium dioxide.

The bulk $(\Omega_{gs,B}, \omega_{gs,B}, \Gamma_{gs,B})$ and surface $(\Omega_{gs,S}, \omega_{gs,S}, \Gamma_{gs,S})$ BGS values deduced from EELS were fixed to fit the carrier dependent quantities on HREELS phonon spectra (Figs. 5.8) where the sensitivity to transport properties shows up. As in the case of EELS, bulk values $(\omega_{P,B}, \Gamma_{P,B})$ were obtained on the highest exposure spectra and fixed to obtain the surface ones $(\omega_{P,S}, \Gamma_{P,S})$ at lower exposure. If the slit aperture was kept constant at $\theta_c = 1.2°$, good fits could be obtained only by using a Voigt resolution function with an increasing lorentzian

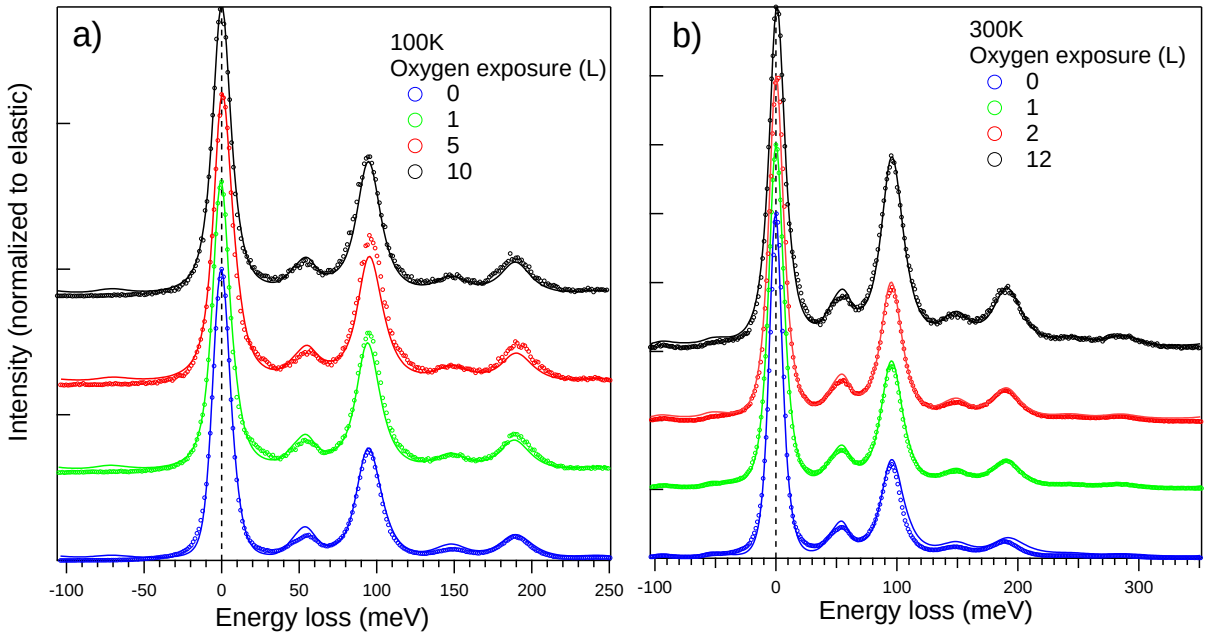

Figure 5.8: Experimental (circles) and fitted (full lines) HREELS phonon spectra for different oxygen exposures at a) 100 K and b) 300 K for a surface layer thickness of $t_S = 6.5$ Å. Data have been normalized to the quasi-elastic peak and shifted for clarity.

weight upon exposure but with an overall constant FWHM (see Fig. 5.9-c for fit results).

The good overall agreement between scans at 100 and 300 K and dielectric modelings, both in EELS (Figs. 5.7) and HREELS (Figs. 5.8) substantiates the chosen profile and the parametrization of the dielectric function. The obtained Drude parameters even improve the agreement between simulations and EELS data in the phonon range. The discrepancies between experiments and fits on the shape of the BGS (Figs. 5.7) and the two first phonons $\omega_{sph,1-2}$ (Figs. 5.8) lies in the simplified oscillator-like description of the BGS (Sect. 3.2.2.4 for discussion) and in the simplified treatment of dielectric anisotropy for the loss function $\xi(\omega) = \epsilon_\perp(\omega)$. In particular, theoretically [135, 136], the line shape of the absorption coefficient of a polaron is expected to be temperature dependent. Parameters are plotted in Fig. 5.9 as a function of exposure and gathered in Tab. 5.1 before and after oxygen exposure. While fitting, no temperature dependence of phonons and interband transitions was accounted for, in particular due to the lack of accurate studies of anharmonicity effects of phonon modes at low temperature. However, high temperature measurements of Ref. [117] showed the absence of a particular shift of the A_{2u} and E_u longitudinal modes (or in other words $\omega_{sph,3}$), on which the present analysis is based, between room temperature and 740 K.

Beyond the estimated error bars (Tab. 5.1), to ascertain the sensitivity to the various parameters, data and best fits of phonon losses have been compared in Fig. 5.10 to simulations for which one parameter is drastically varied. On the reoxidized surface (upper part of Fig. 5.10),

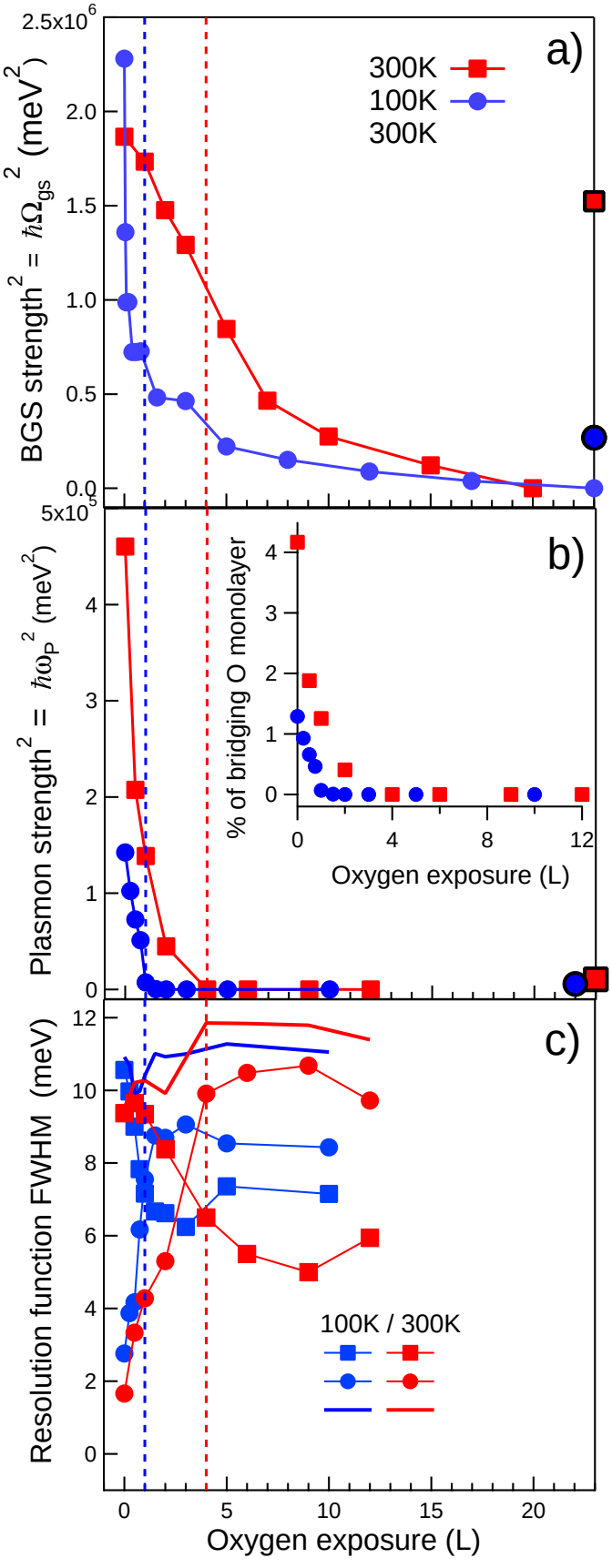

Figure 5.9: Evolution upon oxygen exposure at 300 K (red) and 100 K (blue) of a) the surface band gap strength $\Omega^2_{gs,S}$, b) the surface plasmon strength $\omega^2_{P,S}$ and c) the lorentzian FWHM$_L$ and gaussian FWHM$_G$ components of the resolution function (FWHM$^2_{tot}$ = FWHM^2_L + FWHM^2_G). The stroke symbols in Figs. a,b correspond to bulk values $\Omega^2_{gs,B}$, and $\omega^2_{P,B}$. The dotted lines are guides for the eyes for the transition on carrier density. The inset of Fig. b is the carrier surface density $t\omega^2_{P,S}\epsilon_0 m_e/e^2 = n_S/m^*$ in terms of bridging oxygen monolayer.

Plasmon	$\hbar\omega_P$ (meV)	n/m^* (cm^{-3}/cm^{-2})	$\hbar\Gamma_P$ (meV)	$\mu.m^*$ ($cm^2.V^{-1}.s^{-1}$)
Bulk (300 K)	92 ± 10	$6.1 \pm 1.3\ 10^{18}$	$\simeq 0 \pm 20$	> 60
Bulk (100 K)	40 ± 10	$1.1 \pm 0.6\ 10^{18}$	$\simeq 0 \pm 200$	> 6
Surface (300 K)	650 ± 150	$2.0 \pm 1.0\ 10^{13}$	> 500	< 2.3
Surface (100 K)	330 ± 150	$5.1 \pm 4.6\ 10^{12}$	> 500	< 2.3

Band gap state	$\hbar\Omega_{gs}$ (meV)	$\hbar\omega_{gs}$ (meV)	$\hbar\Gamma_{gs}$ (meV)
Bulk (300 K)	1270 ± 100	1260 ± 100	950 ± 100
Bulk (100 K)	470 ± 100	1170 ± 100	760 ± 100
Surface (300 K)	1500 ± 250	1100 ± 200	970 ± 200
Surface (100 K)	1150 ± 250	1150 ± 200	970 ± 200

Table 5.1: Fitted bulk and surface dielectric characteristics of carrier behaviours and band gap states at 100 and 300 K. Values are given for a surface layer of $t_S = 6.5$ Å. Values of the bulk n/m^* and the surface carrier density n_S/m^* are deduced from the plasma frequency $\omega_P^2 = ne^2/m_e m^* \epsilon_0$ and surface layer thickness t_S. Electron mobilities are obtained from the plasmon damping through $\mu m^* = e/m_e\Gamma$. Surface values are given for the pristine surface (*i.e.* after vacuum annealing or 0 L-exposure) while bulk values are extracted after the highest exposure to oxygen.

without bulk ($\hbar\omega_{P,B} = 0$) carriers or BGS ($\hbar\Omega_{gs,B} = 0$), or with strongly damped bulk carriers ($\hbar\Gamma_{P,B} = 350$ meV), obvious discrepancies on the $\omega_{sph,3}$ phonon loss position show up and are dramatically amplified in the multiple and combination modes. Moreover, only the presence of bulk carrier excitation allows to account for the elastic high energy asymmetry (in particular at 300 K). On the pristine surface, the large surface carrier density or plasma frequency $\omega_{P,S}$ (Tab. 5.1) requires a large damping $\Gamma_{P,S}$ to prevent $\omega_{sph,3}$ shifting to higher values (case $\hbar\Gamma_{P,S} = 10$ meV; lower part of Fig. 5.10). Finally, $\omega_{P,S}$ impacts not only the phonon line position but also the relative elastic/phonon intensity (case $\hbar\omega_{P,S} = 0$; lower part of Fig. 5.10).

Regarding the depth of the surface layer t_S, it has been varied as an integer number of titanium layer spacing along the [110] direction (6.5 Å); fits definitively much worsen (not shown) for thicknesses t_S above 26 Å (4^{th} layer) for both EELS and HREELS and are definitively much better for 6.5-13 Å (1^{st}-2^{nd} layer). Results are presented herein for $t_S = 6.5$ Å. Attempts were made to fit phonon spectra with a fixed surface thickness $t_{BGS} = 6.5 - 13$ Å for BGS as expected from previously published results [22,34,52–54] and a different thickness t_S for surface transport properties. Decreasing values from $t_S = 40$ Å down to nearly zero were obtained between 0 and 4 L. But, noticeably, whatever the model and the surface layer thickness, a constant product $t_S\omega_{P,S}^2 \sim n_S$ was found (not shown); this points to a nearly constant surface density n_S of carriers which value is shown in Tab. 5.1 and Fig. 5.9-b.

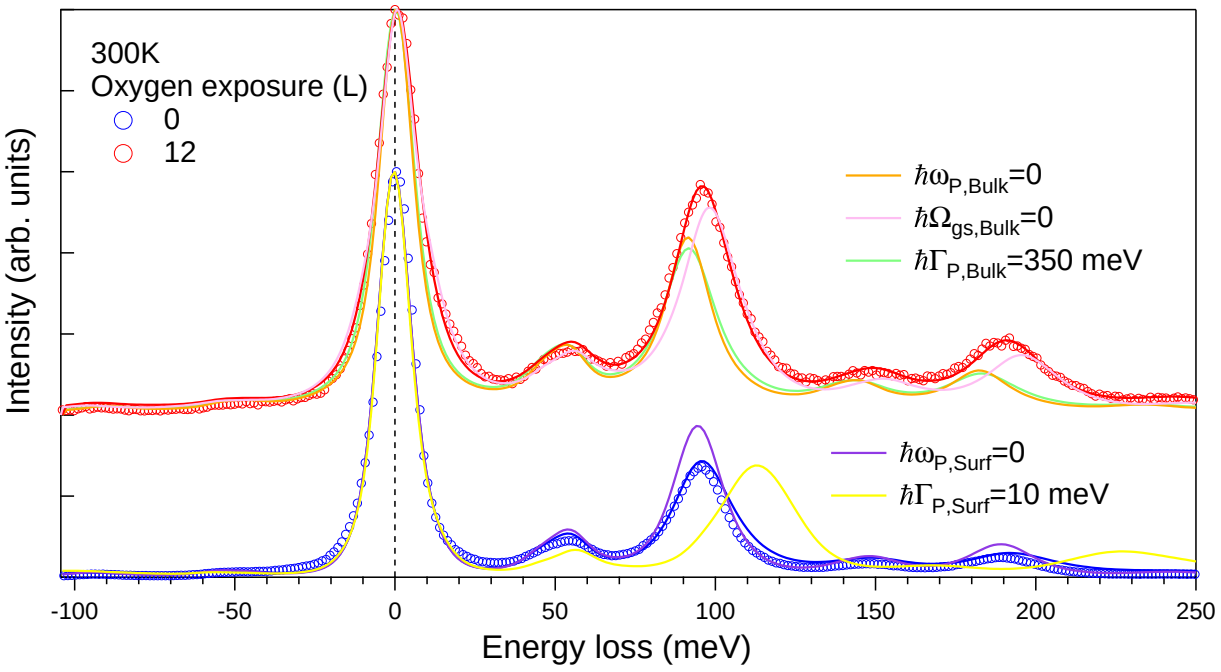

Figure 5.10: Comparison between best fits of Fig. 5.8-b (300K) and simulations i) for the oxidized surface (12 L; red circles) without the contribution of bulk carriers ($\hbar\omega_{P,B} = 0$, orange line), bulk BGS ($\hbar\Omega_{gs,B} = 0$, pink line) or with strongly damped bulk plasmon contributions ($\hbar\Gamma_{P,B} = 350$ meV, green line) and ii) for the reduced surface (0 L; blue circles) without surface carriers ($\hbar\omega_{P,S} = 0$, violet line) or poorly damped surface carriers ($\hbar\Gamma_{P,S} = 10$ meV, yellow line).

5.3 Bulk and surface excess electrons: dual behavior or coexistence of trapped and free states ?

Amazingly, the present (HR)EELS study of reduced rutile substantiates the existence of two type of carriers, bulk and surface ones, with different transport characteristics and quite similar BGS signatures (Tab. 5.1).

5.3.1 Bulk excess electrons

Regarding bulk carriers, using $\omega_{P,B}^2 = n_B e^2/m_e m^* \epsilon_0$, the obtained concentration normalized by the effective mass n_B/m^* (Tab. 5.1) shows a decrease by a factor ~ 5 between 100 K and 300 K in fair agreement with the temperature dependence of the Hall coefficient $R_H \sim 1/n_B$ of samples reduced in similar conditions and assuming a temperature independent effective mass [25]. Using an effective mass $m^* \simeq 10$ along the perpendicular direction as determined by transport measurements ($m^* = 10 - 16$ [25]; $m^* = 15$ [32]) and infra-red analysis ($m^* = 8 - 10$ [29]), the carrier density in our sample amounts to $n_B \simeq 6.1\,10^{19}$ cm^{-3} at room

temperature. Within the hypothesis that the exhaustion regime of stoichiometry defects is reached at 300 K as shown by transport measurements [25, 161] and that two electrons per defect are released, this n_B value sets a lower limit of donor (defects) concentration N_D and of the degree of reduction $x \simeq 10^{-3}$ in TiO_{2-x} [7]. Those values are consistent (i) with p_{O_2}-defect diagrams established by J. Nowotny *et al.* based on equilibrium constants validated on electrical conductivity, thermoelectric power, and thermogravimetric measurements [162] ($x \simeq 10^{-3}$ at $p_{O_2} = 10^{-8}$ Pa and $T = 1273$ K; Fig. 2.3) and (ii) with other determination for samples annealed in similar conditions [25].

The classical physics of semi-conductors [163] shows that, for exhausted donor level and $m^* = 10$ [25, 29, 32], the density of states $N_C = 2(2\pi m_e m^* kT/h^2)^{3/2} = 7.9\,10^{20}$ cm^{-3} in a parabolic conduction band model at $T = 300$ K sets the Fermi level $E_C - E_F = kT\ln(N_D/N_C) \simeq 66 \pm 15$ meV very close to the bottom of the conduction band E_C as seen by inverse photoemission [164] and I(V) curves in STM [22]. Assuming that the semi-condutor is in the freezing regime at 100 K as demonstrated by transport studies [25, 161], the position of donor level E_d deduced from $n_B = (\frac{1}{2}N_D N_c)^{1/2}\exp[-(E_C - E_d)/2kT]$ is at $E_C - E_d = 30 \pm 6$ meV [8]. If not all centers are exhausted at room temperature, the previous equation would give a density of donors of $N_D = 7.2\,10^{19}\sqrt{m^*}$ cm^{-3} from the obtained values of n_B/m^* at 100 and 300 K (Tab. 5.1). Since N_D should be lower than n_B, this yields $m^* < 1.4$ which is lower by one order of magnitude than all expectations from literature [25, 29, 32]. Although the value of the position of the donor level is theoretically outside the range of validity of the used formula $kT \ll E_C - E_d$ [163], this estimate matches previous findings of transport [9] in similar temperature ranges for the activation energy of carriers as determined by resistivity ($E_a = 20 - 30$ meV [148]; $E_a = 28$ meV [31]), Hall coefficient ($E_a = 25$ meV [25]) or for level position estimated by modelling conductivity and Hall mobility measurements ($E_C - E_d = 40 - 60$ meV [149]; $E_C - E_d = 25$ meV [161]). Our result which is based on a direct measurement of the carrier density activation energy in constrats to litterature shows that the donor level is very close to the conduction band. Finally, the bulk carrier damping $\Gamma_{P,B}$ yields an electron drift mobility $\mu_B = e\Gamma_{P,B}/m_e m^*$ in the range of a few cm^2.V.s^{-1} with a large uncertainty ($\mu_B > 6$ cm^2.V.s^{-1} for $m^* = 10$) but larger than Hall determinations [10] ($\mu_H = 0.2$ cm^2.V.s^{-1} [25, 149]).

In their infrared reflectivity study performed on $\epsilon_\perp(\omega)$ (*i.e.* along the crystallographic direction as herein), J.-F. Baumard and F. Gervais [29] analyzed the interplay between phonon and Drude-like response in samples with variable reduction states but with a spectral range limited up to 375 meV (3000 cm^{-1}). They underlined the linear link between the plasmon frequency ω_P and the high frequency value ϵ_∞ of the factorized form of the phonon dielectric function (see Eq. 3.15). They assigned the variation of ϵ_∞ to "transitions in the visible and near-infrared which darkens the crystal". Assuming a concentration independent position

[7] Since $TiO_{2-x} = Ti^{4+}(2xTi^{3+})O_2(xV_O)$, $[V_O] = n_B/2$ and $x = 2[V_O]/[O] = n_B/[O]$

[8] More precisely, for an unknown effective mass, $E_C - E_d = 21 + 4.2\ln(m^*)$ meV.

[9] Bulk resisitivity is given by $\rho_B = 1/en_B\mu_B$ where μ_B is the drift mobility. From Hall coefficient measurements $R_H = (\mu_H/\mu/B)/n_B ec$, the density of carriers can be estimated under the assumption that drift μ_B and Hall mobility μ_H are of the same which is not obvious in a tetragonal lattice [25, 165].

[10] Drift and Hall mobility may differ in tetragonal symmetry [25, 165]

$\omega_{gs,B}$ and damping $\Gamma_{gs,B}$ of the BGS as determined herein, this evolution of ϵ_∞ can be related to the oscillator strength $\Omega_{gs,B}$ (Fig. 5.11) defined in the present parametrization of the dielectric function developed on a broader energy scale (Eq. 3.14). The present (HR)EELS values of $\Omega_{gs,B}$ at 100 and 300 K follow closely the linear link $\Omega_{gs,B} = 10(\pm 0.2)\omega_{P,B}$ found from data of Ref. [29] showing the consistency of the two dielectric approaches.

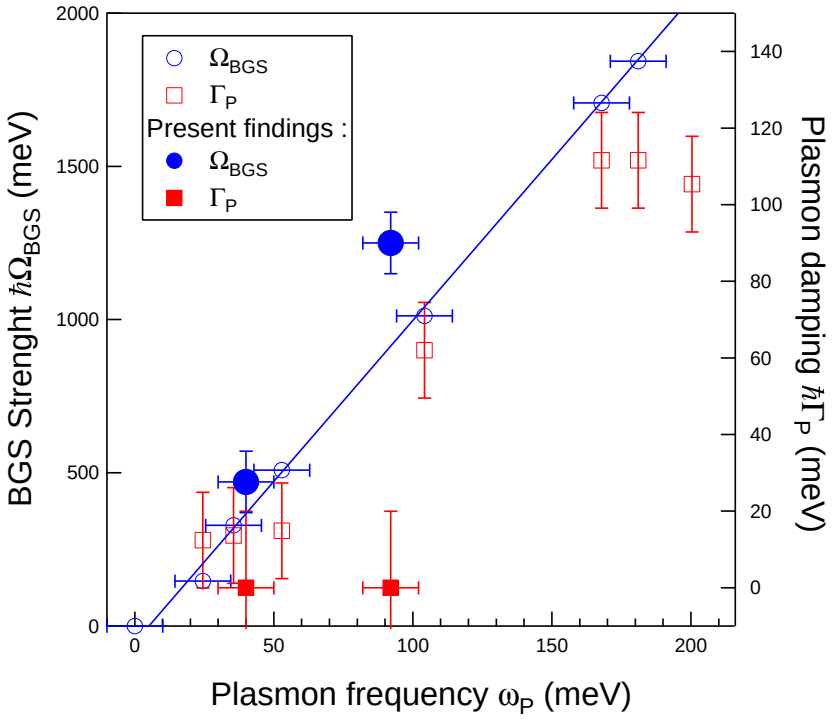

Figure 5.11: Evolution of band gap state oscillator strength $\Omega_{gs,B}$ (open circles) and plasmon damping $\Gamma_{P,B}$ (opens squares) versus the plasmon frequency $\omega_{P,B}$ as deduced from the analysis of infrared data of Ref. [29]. The present (HR)EELS findings for bulk electrons are overlapped with filled symbols.

This linear link is an obvious consequence of the dependence of both oscillator strengths $\omega_{P,B}, \Omega_{gs,B}$ on the sample oxygen deficiency x. Some attempts to vary the concentration of defects by increasing the annealing temperature of the crystal led to nearly no change of the surface phonon position $\omega_{sph,3}$ in HREELS. Coming back to dielectric simulations of the phonon screening by $\omega_{P,B}$ and $\Omega_{gs,B}$, a constant $\omega_{sph,3}$ would require a cancellation of both effects and the following link $\Omega_{gs,B} = \sqrt{\alpha_P/\alpha_{gs}}\omega_P$, where α_P, α_{gs} are the slopes defined in Sect. 3.2.4.3-3.2.4.4. Using the values of Tab. 3.2, a ratio $\sqrt{\alpha_P/\alpha_{gs}} = 11.2$ is found in close agreement to infrared findings [29] reinterpreted in Fig. 5.11. However, this linear link does not rule out the existence of two kinds of excess electrons, ones more localized or trapped giving rise to the BGS feature and others leading to the transport properties, with respective concentrations increasing in parallel with reduction state. However, the same linear link is kept by varying the temperature from 100 to 300 K; under the hypothesis of coexistence of trapped and free states, this would imply similar thermally activated processes which keep constant the ratio $\omega_{P,B}/\Omega_{gs,B}$. Moreover, in the hypothesis of really localized state, the gap state level $\hbar\omega_{gs,B} \simeq 1000$ meV would lie much too deep to see any sizable temperature activated carrier population. As predicted by polaron theory [135, 136], all those findings favour instead a dual behavior of bulk excess electrons, which appear as deep lying states or carriers with high mobility depending on the way they are exited. The apparent discrepancy with infrared data [29] (see Fig. 5.11) on the damping $\Gamma_{P,B}$ may be related to the difficulty to

accurately fit this parameter in both measurements (HREELS and IR) [29] or the existence of a transition of behaviour on $\Gamma_{P,B}$ at a given deficiency.

5.3.2 Surface excess electrons

The determined surface carrier density $n_S/m^* \sim t_S\omega^2_{P,S}$, which is a constant whatever the chosen layer thickness t_S, amounts to a few percent of bridging oxygen coverage (inset of Fig. 5.9-b). Since oxygen heals easily those "surface" carriers (Fig. 5.9), they most probably find their origin in O_b-vac on bridging oxygen rows [2–8]. With an effective mass [11] of $m^* \simeq 10$ and assuming that two electrons contribute to n_S per surface vacancy [26], a coverage around 8 % of monolayer of bridging oxygen is obtained as it is expected for standard surface preparation techniques [2–8, 12]. But two hypothesis can be invoked to explain the existence of a subsurface enriched in electrons having a Drude-like behaviour at the origin of the sizeable relative variation of the phonon/elastic peak (Fig. 5.3): (i) either an accumulation layer due to surface defect states or (ii) the genuine transport behaviour of excess electrons due to O_b-vac.

In a classical n-type semi-conductor, the charge transfer between bulk and surface defect states can induce a space charge layer and a band-bending [163, 166] (Fig. 5.12-a). As no actual surface state exists on stoichiometric TiO_2, flat bands are expected on a perfect surface. But work function change and band-bending, mostly observed by photoemission spectroscopy [14, 52, 55, 130, 167], are known to occur at the defective surface of rutile (Fig. 5.12-b extracted from Ref. [130]). An upwards variation of band-bending ΔV_{bb} in the range of few tenths of electron-volt [14, 52, 55, 130, 167] has been found upon exposure to electronegative oxygen molecules. So surface vacancies may act as donor-like states that create a surface dipole with a positively charged top surface and a negatively charged accumulation layer in the $n-$type substrate inducing a decrease of work function as measured by the shift of the electron distribution curve in photoemission [130, 167] compared to a stoichiometric surface (Fig. 5.12). The defects would appear as a partially filled state in photoemission with a centroid around 0.8 eV below the Fermi level (Fig. 5.12-a). The induced downward band bending should extent over a typical thickness given by the so-called Debye length $L_D = \sqrt{2V_{bb}\epsilon_0\epsilon(0)/en_B}$ over which screening by bulk carriers is effective. Never really estimated in the literature, it amounts to $L_D \simeq 80$ Å for $V_{bb} = 0.4$ eV [130] [12], $\epsilon(\omega = 0) = 85$ and $n_B = 6.1\,10^{19}$ cm^{-3} at $T = 300$ K ($m^* \simeq 10$) as found herein. The associated total screening charge $Q_s \simeq n_B L_D \simeq 4.9\,10^{13}$ cm^{-2} estimated for the upper limit $\Delta V_{bb} = 0.4$ eV found in the literature [14, 52, 55, 130, 167] is smaller than the surface carrier obtained by the present HREELS analysis ($n_S \simeq 2\,10^{14}$; $m^* = 10$) but sill within the uncertainties on data and effective mass. In a same way, L_D is much larger than the thickness used herein

[11] Actually, surface and bulk effective masses should be different.

[12] This assumes that flat bands are recovered at the end of exposure *i.e.* $\Delta V_{bb} = V_{bb}(0L)$ and that the shift of the valence band edge seen in photoemission is the actual one *i.e.* $L_D \gg \lambda$, λ being the escape depth of photoelectrons. A basic exponential modelling of the depth dependence of the band position $\Delta V(z) = V_{bb}\exp(-z/L_D)$ combined with the damping of photoemission signal over λ shows that the binding energy scale is shifted by $\Delta V_{\rm XPS} = \int_0^\infty 1/\lambda \exp(-z/\lambda) V_{bb}\exp(-z/L_D) = V_{bb}L_D/(L_D+\lambda)$. The same reasoning holds true also for a more classical parabolic [163] band bending.

$t_S = 6.5 - 13$ Å to analyze data. But, once released the constraint $t_{S,\mathrm{EELS}} = t_{S,\mathrm{HREELS}}$ still with $t_{S,\mathrm{EELS}} \simeq 6 - 13$ Å, much larger value up to $t_{S,\mathrm{HREELS}} \simeq 40$ Å compatible with the order of magnitude of L_D could be obtained. But, all *ab initio* calculations [15, 22, 34, 53, 54, 152] combined with STM [15, 22, 53] and synchrotron resonant photodiffraction [52] data conclude that the O_b-vac excess charges are transferred to subsurface titaniums [13] and not to the actual bulk, ruling out the presence of the required positively charged surface for the space charge layer. Finally, the most convincing argument is the evolution of band bending with oxygen exposure (Fig. 5.12 from Ref. [130]). It follows a two steps behavior, which parallels the observed evolution of $\Omega_{gs,S}$ and $\omega_{P,S}$ (Fig. 5.9-a,b). Up to $\simeq 4 - 5$ L in the regime of healing of oxygen vacancies, band bending is nearly ineffective ($V_{bb} < 0.1$ V) while the sharp decrease of $\omega_{P,S}$ and surface carrier density is observed (Fig. 5.9-b). All these arguments discards the role of any strong accumulation layer due to vacancies, as suspected in the STM measurements of Ref. [22] and strongly favours the hypothesis that the found surface transport behaviour is linked to excess electrons provided by O_b-vac. Moreover, this conclusion validates *a posteriori* the chosen of profile for the(HR)EELS analysis.

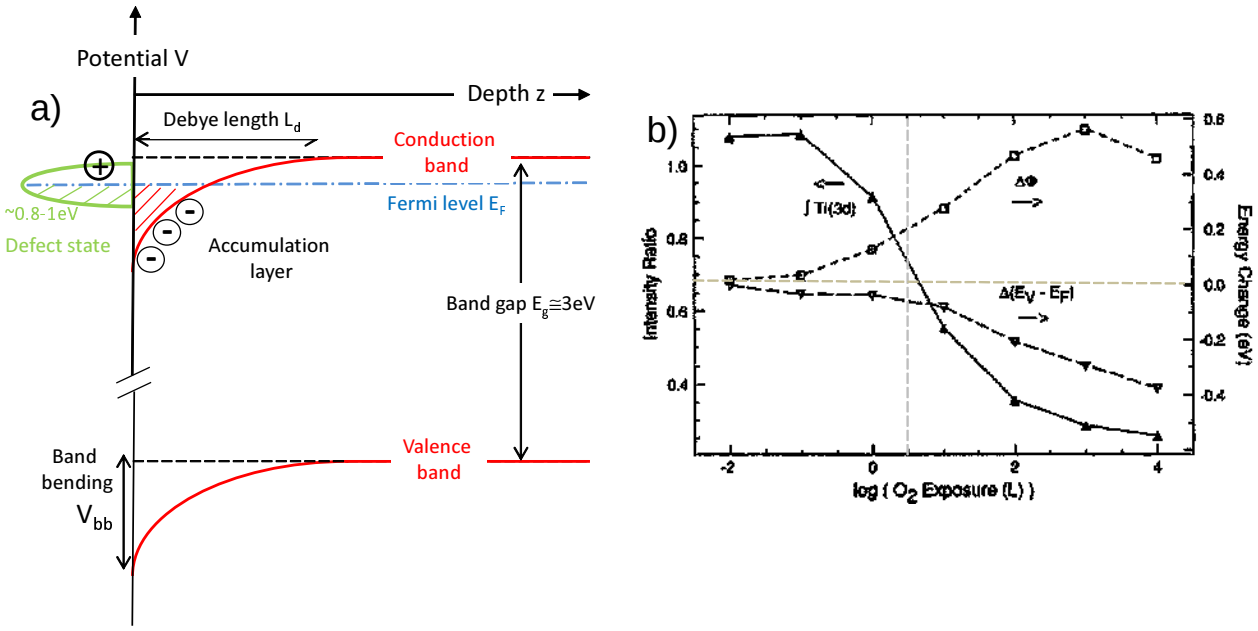

Figure 5.12: a) Schematic band diagram for a donor surface defect state inducing an accumulation layer and a downward band-bending in a n-type semiconductor. b) Relative variation with oxygen exposure of the intensity of the band gap states (filled triangle, $\int Ti(3d)$), the work function (square, $\Delta\Phi$) and the separation between Fermi level and valence band (open triangle, $\Delta(E_V - E_F)$ *i.e.* the band bending ΔV_{bb}. Quantities have been obtained by synchrotron photoemission spectroscopy ($h\nu = 47$ eV; $T = 400$ K) of the valence band of a TiO_2(110) surface annealed at 1000 K under vacuum. From Ref. [130]

[13] First and second layers mainly.

Interestingly, the oxygen healing of surface carriers (Fig. 5.9-b) presents an initial sharp decrease down to a negligible value above 1 L at 100 K and 4 L at 300 K. The lower the temperature the faster the decrease as expected from the longer residence time of the oxygen molecule at the surface. In passing, this means that at 100 K, adsorbed O_2 is mobile enough to reach a vacancy and that the charge transfer is not quenched. In parallel, the BGS oscillator strength (Fig. 5.9-a) follows a similar trend with an initial fast decrease up to a value close to the bulk one before decreasing much more slowly. Only 0.1 L is required to divide $\Omega^2_{gs,S}$ by two at 100 K. While the fast decrease may be assigned to the filling of surface vacancies [2–8, 12], the presence in the subsurface of bulk defects, such as titanium interstitials [14], accessible to charge transfer to the adsorbed oxygen molecules, may explain the slower decrease of BGS. This conclusion is fully in line with STM and UPS measurements [14, 15] which showed an excess of adsorbed oxygen in the trough between bridging oxygen rows compared to the initial O_b-vac or OH_b coverage and a much faster decrease of OH-3σ signal than that of the BGS. Those bulk defects in the surface layer contribute marginally to the surface density of carriers (Fig. 5.9) but still contribute to the BGS intensity. If their healing does not change the overall surface conductivity, it affects the band bending [130] (Fig. 5.12-b) as one would expect from a gradient of concentration of bulk donor close to the surface. There is a debate in the literature about the major contribution to the BGS seen in photoemission [12–14, 55, 58], Ti-interstitials versus surface vacancies (see Chap. 4). In our measurements, the contribution to the BGS intensity of the subsurface defects that can be healed compared to surface vacancies signal can be estimated as the crossing point of the dotted lines in Fig. 5.9-a *i.e.* $(\Omega_{gs,S,V_O}/\Omega_{gs,Ti_i})^2 \simeq 2-3$. It is important to keep in mind that this ratio does not involve only concentration effects but also transition probabilities [14] and that the probing depth is in the range of 30 Å (see Sect. 3.2.5).

As in the bulk, the excess electrons due to O_b-vac appears with a dual behaviour through their transport properties and their BGS signatures. Spreading of excess charges and delocalized distribution over several subsurface titanium atoms has been predicted by *ab initio* modellings [34, 54], seen by STM measurements of filled states [22, 53] and photodiffraction analysis [52]. But up to now, the signature of the transport by those excess electrons has never been observed although it has been suspected in the molecular dynamics simulations of Ref. [34]; the theoretically predicted apparent activation energy of "hopping" of 70 meV implies that a dynamical averaging of the localisation of the electron over several adjacent titanium atoms should happen at room temperature. Our results (Fig. 5.1) point to an apparent activation of surface carrier density of 17.5 meV between 100 and 300 K; this value is quite close to that of the bulk although the mobility of the surface electrons seems to be lower by one order of magnitude (Tab. 5.1). But the fundamental question of nature of transport, through hopping or within a conduction band, that is to say the spatial extent of the polaronic distortion (small vs large polaron) is still unsettled by the present study.
Finally, a change in the resolution function of the apparatus from Gaussian to more Lorentzian parallels exactly the decrease of surface carrier density (Fig. 5.9-c). This change of peak shape, but at constant overall FWHM, *i.e.* resolution, translates a phenomenon that escapes the present modelling; it is either the inability of the Drude function to perfectly describe the

[14] That should be similar since charges are localized on similar sites.

low-frequency transport at all exposures or the presence of frustrated low frequency vibration modes of adsorbed oxygen O_{ad} resulting from the dissociation of the molecule on vacancies or hydroxyl groups.

5.4 Conclusion

This chapter tried to answer the hot question of the behaviour of excess electrons due to stoichiometry defects in TiO_2. For the first time in a single experiment, both the transport properties and the band gap states could be simultaneously studied and quantified. To do so, the evolution of (HR)EELS spectra during oxygen exposure have been fitted within the dielectric theory to obtain the oscillator strength Ω_{gs} of the BGS and the Drude plasma frequency ω_P. Adequate results could be obtained only by using a profile of dielectric function which distinguish between excess electrons related to surface vacancies and bulk defects.

Both types of electrons show a dual behaviour depending on the way they are excited. They appear either as deep lying state when "optically" excited or as shallow donor levels for conduction. The temperature dependence of the bulk carrier density, which is in the range of a few 10^{19} cm^{-3}, set the defect and Fermi levels very close to the conduction band in agreement with previous transport measurements. But the clear correlation between Ω_{gs} and ω_P demonstrates that the same electrons are involved in both excitations. In parallel, a strong accumulation of carriers is found just beneath the surface having a concentration compatible with typical coverage in O_b-vac. Those surface carriers can be completely healed by an exposure to a few monolayers of oxygen as well as the corresponding BGS signature. This dual behaviour is associated to a similar activation energy to bulk electrons but with a lower mobility. Those results have profound implications in the (photo)catalytic properties of titania in which the transport properties of excited carriers is of paramount importance [1,2].

Finally, the present approach on rutile could be easily extended towards, not only obviously anatase for which a more delocalized behaviour is expected [22, 168], but other oxides of interest in which the mechanism of conduction is still debated *e.g.* $SrTiO_3$ [169]. Beyond a study of anisotropy effects not addressed here, it could also be improved through a better dielectric description of the polaron behaviour [135] than that developed here.

CHAPTER 6

CONCLUSION

The present work was aimed at exploring the origin, location and transport of excess charges in rutile TiO_2. The approach has combined (High Resolution) Electron Energy Loss Spectroscopy -(HR)EELS- measurements on the $TiO_2(110)$-(1×1) surface prepared in different ways and fitting of experimental data using dielectric theory. HREELS method, although scarcely used nowadays in surface science, was found to be of great relevance to pinpoint the formation of excess charges and the response of the solid medium to the presence of those charges. New experimental approaches have been proposed in the very studied field of the defective titanium dioxide.

The dielectric approach was used to model the impact of all solid-state excitations on the shaping of (HR)EELS spectra of reduced TiO_2. It was proposed to describe band gap states (BGS) by an oscillator and conductivity through a Drude term. While BGS appears as an isolated feature in the band gap, the EELS signature of the existence of charge carriers is less obvious. Contrary to other oxides, the large static dielectric function of TiO_2 leads only to a modest broadening of the quasi-elastic peak at moderate carrier density through the excitation of surface plasmons. Enhancing apparent resolution allows to glimpse their existence and their combination modes with surface phonons. In this respect, an algorithm to improve resolution was introduced. Fortunately, the carrier excitations can be tracked down not only through the imaginary part of their dielectric function but also through its real part and the resulting screening it induces. Due to its very large oscillator strength, one longitudinal phonon can be used as a indicator; since its frequency lies between Drude and BGS terms, it shifts upwards with the occurrence of plasmon excitation and downwards with the BGS oscillator strength. However, the effect of the profile of the dielectric function and EELS depth sensitivity, in particular due to the existence of surface vacancies, may complexify these conclusions.

Next, the depth sensitivity of the EELS technique was employed to gain some insights into the density profile of the excess charges and into their surface versus bulk contributions. The origin of BGS of TiO_2 was investigated by means of specific measurement strategies

and surface treatments, including: (i) surface annealing in the 400-900 K range with an hot filament, while measuring the temperature by means of the Bose-Einstein ratio of loss/gain phonons intensity; (ii) cooling down to 100 K; (iii) off-specular measurements; (iv) electron bombardment which only produces oxygen vacancies; (v) exposure to either oxygen or water vapour at different temperatures. By analysing the effects of those treatments on the BGS feature, it has been possible (i) to directly evidence BGS in conditions in which O_b-vac or Ti_{int} were the unique type of defects of the rutile surface and (ii) to observe the reactivity of these defects with either oxygen or water. Finally, a schematic profile of excess electrons through the surface region of TiO_2(110) was proposed.

The above developed dielectric theory was applied to study the excess charge property of a reduced TiO_2 surface by fitting the actual data. First of all, direct experimental evidences demonstrate the existence of "Drude-like" carriers: (i) the effect of oxygen exposure on phonon/elastic ratio; (ii) both the asymmetry of the quasi-elastic peak and its temperature-dependence; (iii) the phonon line shape. In accord with previous findings, data were better reproduced using a profile with an accumulation of charge in the first sub-surface layers. Interestingly, the results shows the existence of two kinds of charge carriers, one is due to bulk defects, the other is due to O_b-vac. Although both carriers have a similar BGS signature, they show quite different transport properties. The estimated mobility of bulk carriers is one order of magnitude higher than that of the surface carriers. Their activation energy evaluated from the data is found around a few tens of meV in good agreement with values obtained from Hall coefficient and conductivity measurements. For bulk electrons, the linear correlation between the BGS oscillator strength and the Drude frequency suggests that they behave in a dual way. The fact that the same correlation holds when the reduction state and temperature is changed from 100 to 300 K strongly support the idea. For surface electrons, transport and BGS properties are healed in parallel when exposing to oxygen suggesting that this dual behaviour also holds for them.

The main achievement of the research work presented in this manuscript is the description of the reduced titanium dioxide surface region in terms of categories which are usually exclusive of each other, oxygen vacancies and titanium interstitials, surface and bulk defects, free-carriers and bound states. Unlike often developed arguments, it is shown that these categories coexist. In the future, the original approach developed here with the EELS technique should be extended towards the important family of the reducible oxides in which defects play an paramount role [9].

CHAPTER 7

ANNEX: PUBLISHED PAPER IN REV. SCI. INST. 86 (2015) 013906

Spectral restoration in high resolution electron energy loss spectroscopy based on iterative semi-blind Lucy-Richardson algorithm applied to rutile surfaces

R. Lazzari, J. Li, J. Jupille, Review of Scientific Instruments 86 (2015) 013906

REFERENCES

[1] A. Fujishima, X. Zhang, and D. Tryk. TiO_2 photocatalysis and related surface phenomena. *Surf. Sci. Rep.*, 63:515–582, 2008.

[2] M. A. Henderson. A surface science perspective on TiO_2 photocatalysis. *Surf. Sci. Rep.*, 66:185–297, 2011.

[3] U. Diebold. The surface science of titanium dioxide. *Surf. Sci. Rep.*, 48:53, 2003.

[4] C. Lun Pang, R. Lindsay, and G. Thornton. Chemical reactions on rutile TiO_2(110). *Chem. Soc. Rev.*, 37:2328, 2008.

[5] L.-M. Liu, P. Crawford, and P. Hu. The interaction between adsorbed OH and O_2 on TiO_2 surfaces. *Prog. Surf. Sci.*, 84:155–176, 2009.

[6] Z. Dohnálek, I. Lyubinetsky, and R. Rousseau. Thermally-driven processes on rutile TiO_2(110)-(1x1): A direct view at the atomic scale. *Prog. Surf. Sci.*, 85(5-8):161–205, 2010.

[7] C. L. Pang, R. Lindsay, and G. Thornton. Structure of clean and adsorbate-covered single-crystal rutile TiO_2 surfaces. *Chem. Rev.*, 113:3887–3948, 2013.

[8] M. A. Henderson and I. Lyubinetsky. Molecular-level insights into photocatalysis from scanning probe microscopy studies on TiO_2(110). *Chem. Rev.*, 113:4428–4455, 2013.

[9] J. Jupille and G. Thornton. *Defects at oxide surfaces*. Springer, 2015.

[10] V. E. Henrich, G. Dresselhaus, and H. J. Zeiger. Observation of two-dimensional phases associated with defect states on the surface of TiO_2. *Phys. Rev. Lett.*, 36:1335–1339, 1976.

[11] N. G Petrik, Z. Zhang, Y. Du, Z. Dohnálek, I. Lyubinetsky, and G. A. Kimmel. Chemical reactivity of reduced TiO_2(110): the dominant role of surface defects in oxygen chemisorption. *J. Phys. Chem. C*, 113(28):12407–12411, 2009.

[12] C. M. Yim, C. L. Pang, and G. Thornton. Oxygen vacancy origin of the surface band-gap state of TiO_2(110). *Phys. Rev. Lett.*, 104:036806, 2010.

[13] X. Mao, X. Lang, Z. Wang, Q. Hao, B/ Wen, Z. Ren, D. Dai, C. Zhou, L M. Liu, and X. Yang. Band-gap states of TiO_2(110): major contribution from surface defects. *J. Phys. Chem. Lett.*, 4:3839–3844, 2013.

[14] S. Wendt, P. T. Sprunger, E. Lira, G. K. H. Madsen, Z. Li, J. O. Hansen, J. Matthiesen, A. Blekinge-Rasmussen, E. Laegsgaard, B. Hammer, and F. Besenbacher. The role of interstitial sites in the Ti3d defect state in the band gap of titania. *Science*, 320:1755–1759, 2008.

[15] A.C. Papageorgiou, N.S. Beglitis, C.L. Pang, G. Teobaldi, G. Cabailh, Q. Chen, A.J. Fisher, W.A. Hofer, and G. Thornton. Charge traps and their effect on the surface properties of TiO_2(110). *Proceeding of the National Academy of Science*, 107:2391–2396, 2010.

[16] E. Lira, J.Ø Hansen, P. Huo, R. Bechstein, P. Galliker, E. Lægsgaard, B. Hammer, S. Wendt, and F. Besenbacher. Dissociative and molecular oxygen chemisorption channels on reduced rutile TiO_2 (110): an STM and TPD study. *Surf. Sci.*, 604:1945–1960, 2010.

[17] E. Lira, S. Wendt, P. Huo, J. Ø Hansen, R. Streber, S. Porsgaard, Y. Wei, R. Bechstein, E. Lægsgaard, and F. Besenbacher. The importance of bulk Ti^{3+} defects in the oxygen chemistry on titania surfaces. *J. Am. Chem. Soc.*, 133:6529–6532, 2011.

[18] E. Lira, P. Huo, J. Ø Hansen, F. Rieboldt, R. Bechstein, Y. Wei, R. Streber, S. Porsgaard, Z. Li, E. Lægsgaard, and F. Besenbacher. Effects of the crystal reduction state on the interaction of oxygen with rutile TiO_2(110). *Catal. Today*, 182:25–38, 2012.

[19] Y. Du, N. A. Deskins, Z. Zhang, Z. Dohnalek, M. Dupuis, and I. Lyubinetsky. Formation of O adatom pairs and charge transfer upon O_2 dissociation on reduced TiO_2(110). *Phys. Chem. Chem. Phys.*, 12:6337–6344, 2010.

[20] P. Borghetti, Meriggio; E., G. Rousse, G. Cabailh, R. Lazzari, and J. Jupille. Photoemission fingerprints for structural identification of titanium dioxide surfaces. *J. Phys. Chem. Lett.*, 7:3223–3228, aug 2016.

[21] S. Eriksen and R. G. Egdell. Electronic excitations at oxygen deficient TiO_2(110) surfaces: a study by EELS. *Surf. Sci.*, 180:263–278, 1987.

[22] M. Setvin, C. Franchini, X. Hao, M. Schmid, A. Janotti, M. Kaltak, G. Van de Walle, G. Kresse, and U. Diebold. Direct view at excess electrons in TiO_2 rutile and anatase. *Phys. Rev. Lett.*, 113:086402, 2014.

[23] M. Li, W. Hebenstreit, U. Diebold, A. M. Tyryshkin, M. K. Bowman, G. G. Dunham, and M. A. Henderson. The influence of the bulk reduction state on the surface structure and morphology of rutile TiO_2 (110) single crystals. *J. Phys. Chem. B*, 104:4944–4950, 2000.

[24] M. Chiesa, M.C. Paganini, S. Livraghi, and E. Giamello. Charge trapping in TiO_2 polymorphs as seen by Electron Paramagnetic Resonance spectroscopy. *Phys. Chem. Chem. Phys.*, 15:9435, 2013.

[25] E. Yagi, R. R. Hasiguti, and M. Aono. Electronic conduction above 4 K of slightly reduced oxygen-deficient rutile TiO_{2-x}. *Phys. Rev. B*, 54:7945–7956, 1996.

[26] G. Mattioli, P. Alippi, F. Filippone, R. Caminiti, and A. A. Bonapasta. Deep versus shallow behavior of intrinsic defects in rutile and anatase TiO_2 polymorphs. *J. Phys. Chem. C*, 114:21694–21704, 2010.

[27] A. Janotti, C. Franchini, J. B. Varley, G. Kresse, and C. G. Van de Walle. Dual behavior of excess electrons in rutile TiO_2. *Phys. Stat. Sol. (RRL)*, 7:199–203, 2013.

[28] A. Fujimori, A. E. Bocquet, K. Morikawa, K. Kobayashi, I. T. Saithoh, Y. Tokura, I. Hasex, and M. Onoda. Electronic structure and electron-phonon interaction in transition metal oxides with d^0 configurations and lightly doped compounds. *J. Phys. Chem. Solids*, 57:1379–1384, 1996.

[29] J. F. Baumard and F. Gervais. Plasmon and polar optical phonons in reduced rutile TiO_2. *Phys. Rev. B*, 15:2316–2323, 1977.

[30] R. R. Hasiguti and E. Yagi. Electrical conductivity below 3 K of slightly reduced oxygen-deficient rutile TiO_{2-x}. *Phys. Rev. B*, 49:7251–7256, 1994.

[31] E. Iguchi, K. Yajima, T. Asahina, and Y. Kanamori. Resistivities of reduced rutile (TiO_2) from 300 K to exhaustion range. *J. Phys. Chem. Solids*, 35:597–599, 1974.

[32] E. Hendry, F. Wang, J. Shan, T. F. Heinz, and M. Bonn. Electron transport in TiO_2 probed by THz time-domain spectroscopy. *Phys. Rev. B*, 69:081101(R), 2004.

[33] N. A. Deskins and M. Dupuis. Electron transport via polaron hopping in bulk TiO_2: A density functional theory characterization. *Phys. Rev. B*, 75:195212, 2007.

[34] P. M. Kowalski, M. F. Camellone, N. N. Nair, B. Meyer, and D. Marx. Charge localization dynamics induced by oxygen vacancies on the TiO_2(110) surface. *Phys. Rev. Lett.*, 105, 2010.

[35] R. Lazzari, J. Li, and J. Jupille. Spectral restoration in reflection energy electron loss spectroscopy based on iterative semi-blind lucy-richardson algorithm applied to rutile surfaces. *Rev. Sci. Instrum.*, 86:013906, 2015.

[36] H. Lüth. *Surface and Interfaces of Solids*, volume 15 of *Surface Science*. Springer Verlag, 1992.

[37] H. Ibach. *Physics of Surfaces and Interfaces*, volume 10. Springer, 2006.

[38] http://www.lktech.com/products/lk2000.php.

[39] D. P. Woodruff and T. A. Delchar. *Modern Techniques of Surface Science*. Cambridge University Press, 1994.

[40] C.T. Campbell and S.M. Valone. Design consideration for simple gas dosers in surface science application. *J. Vac. Sci. Technol. A*, 3:408–411, 1985.

[41] J. Nowotny, M.A. Alim, T. Bak, M. A. Idris, M. Ionescu, K. Prince, M. Z. Sahdan, K. Sopian, M.A.T. Teridi, and W. Sigmund. Defect chemistry and defect engineering of TiO_2 -based semiconductors for solar energy conversion. *Chem. Soc. Rev.*, 44(23):8424–8442, 2015.

[42] H. Iddir, S. Öğüt, P. Zapol, and N. D. Browning. Diffusion mechanisms of native point defects in rutile TiO_2: *Ab initio* total-energy calculations. *Phys. Rev. B*, 75(7):073203, 2007.

[43] B. J. Morgan and G. W. Watson. Intrinsic n-type defect formation in TiO_2 : a comparison of rutile and anatase from GGA+ U calculations. *J. Phys. Chem. C*, 114:2321–2328, 2010.

[44] H.Y. Lee, S.J. Clark, and J. Robertson. Calculation of point defects in rutile TiO_2 by the screened-exchange hybrid functional. *Phys. Rev. B*, 86(7), aug 2012.

[45] P. Deák, B. Aradi, and T. Frauenheim. Oxygen deficiency in TiO_2 : Similarities and differences between the Ti self-interstitial and the O vacancy in bulk rutile and anatase. *Phys. Rev. B*, 92:045204, 2015.

[46] K.M. Pangan-Okimoto, P. Gorai, A.G. Hollister, and E.G. Seebauer. Model for oxygen interstitial injection from the rutile $TiO_2(110)$ surface into the bulk. *J. Phys. Chem. C*, 119:9955–9965, 2015.

[47] M. K. Nowotny, L. R. Sheppard, T. Bak, and J. Nowotny. Defect chemistry of titanium dioxide. application of defect engineering in processing of TiO_2 -based photocatalysts. *J. Phys. Chem. C*, 112:5275–5300, 2008.

[48] M. A. Henderson. Mechanism for the bulk-assisted reoxidation of ion sputtered TiO_2 surfaces: diffusion of oxygen to the surface or titanium to the bulk? *Surf. Sci.*, 343:L1156 – L1160, 1995.

[49] M. Li, W. Hebenstreit, L. Gross, U. Diebold, M. A. Henderson, D. R. Jennison, P. A. Schultz, and M. P. Sears. Oxygen-induced restructuring of the $TiO_2(110)$ surface: a comprehensive study. *Surf. Sci.*, 437:173–190, 1999.

[50] Z. Zhang, J. Lee, J. T. Yates, R. Bechstein, E. Lira, J. Hansen, St. Wendt, and F. Besenbacher. Unraveling the diffusion of bulk Ti interstitials in rutile $TiO_2(110)$ by monitoring their reaction with O adatoms. *J. Phys. Chem. C*, 114(7):3059–3062, 2010.

[51] J. Goniakowski and C. Noguera. Polarity in oxide nano-objects. *Chem. Rev.*, 113:4073–4105, 2013.

[52] P. Krüger, S. Bourgeois, B. Domenichini, H. Magnan, D. Chandesris, P. Le Fèvre, A. M. Flank, J. Jupille, L. Floreano, A. Cossaro, A. Verdini, and A. Morgante. Defect states at the TiO_2(110) surface probed by resonant photoelectron diffraction. *Phys. Rev. Lett.*, 100:055501, 2008.

[53] T. Minato, Y. Sainoo, Y. Kim, H. S. Kato, K. Aika, M. Kawai, J. Zhao, H. Petek, T. Huang, W. He, W. Bing, W. Zhuo, Y. Zhao, J. Yang, and J. G. Hou. The electronic structure of oxygen atom vacancy and hydroxyl impurity defects on titanium dioxide (110) surface. *J. Chem. Phys.*, 130:124502, 2009.

[54] N. A. Deskins, R. Rousseau, and M. Dupuis. Localized electronic states from surface hydroxyls and polarons in TiO_2(110). *J. Phys. Chem. C*, 113:14583–14586, 2009.

[55] K. Mitsuhara, H. Okumura, A. Visikovskiy, M. Takizawa, and Y. Kido. The source of the Ti 3d defect state in the band gap of rutile titania (110) surfaces. *J. Chem. Phys.*, 136:124707, 2012.

[56] M. L. Knotek and P. J. Feibelman. Ion desorption by core-hole Auger decay. *Phys. Rev. Lett.*, 40:964–967, Apr 1978.

[57] J. Lee, Z. Zhang, and J. T. Yates. Electron-stimulated positive-ion desorption caused by charge transfer from adsorbate to substrate: oxygen adsorbed on TiO_2(110). *Phys. Rev. B*, 79(8):081408, Feb 2009.

[58] K. Onda, B. Li, and H. Petek. Two-photon photoemission spectroscopy of TiO_2(110) surfaces modified by defects and O_2 or H_2O adsorbates. *Phys. Rev. B*, 70:0455415, 2004.

[59] C. L. Pang, O. Bikondoa, D. S. Humphrey, A. C. Papageorgiou, G. Cabailh, R. Ithnin, Q. Chen, C. A. Muryn, H. Onishi, and G. Thornton. Tailored TiO_2(110) surfaces and their reactivity. *Nanotechnology*, 17:5397–5405, 2006.

[60] A. A. Lucas and M. Sunjić. Fast-electron spectroscopy of collective excitations in solids. *Prog. Surf. Sci.*, 2:75–137, 1972.

[61] H. Ibach and D. L. Mills. *Electron Energy Loss Spectroscopy and Surface Vibrations*. Academic Press, New York, 1982.

[62] M. Rocca. Low-energy EELS investigation of surface electronic excitations on metal. *Surf. Sci. Rep.*, 22(1-2):1–72, 1995.

[63] P. A. Thiry, M. Liehr, J.-J. Pireaux, and R. Caudano. Electron interaction mechanisms in high resolution electron energy loss spectroscopy. *Phys. Scripta*, 35:368–379, 1987.

[64] H. Ibach. Optical surface phonons in zinc oxide detected by slow-electron spectroscopy. *Phys. Rev. Lett.*, 24:1416–1418, 1970.

[65] L.L. Kesmodel. New high resolution electron spectrometer for surface vibrational analysis. *J. Vac. Sci. Technol. A*, 1:1456–1460, 1983.

[66] H. Ibach. *Electron Energy Loss Spectrometers: The technology of high performance.* Springer-Verlag, 1991.

[67] D. Roy and D. Trembaly. Design of electron spectrometers. *Rep. Prog. Phys.*, 53:1621–1674, 1990.

[68] S. Andersson and M. Persson. Inelastic electron scattering from surface vibrational modes of adsorbate-covered Cu(100). *Phys. Rev. B*, 24(6):3659, 1981.

[69] C. E. Kuyatt and J.A. Simpson. Electron monochromator design. *Rev. Sci. Instrum.*, 38(1):103–111, 1967.

[70] D. Roy and J.-D. Carette. Optimum deflection angle for cylindrical and spherical electrostatic spectrometer. *Appl. Phys. Lett.*, 16(11):413–416, 1970.

[71] D. Roy, A. Delage, and J.-D Carette. Description and performance of a high resolution electron spectrometer. *Journal of Physics E: Scientific Instruments,*, (8):109–114, 1975.

[72] M. Liehr, P.A. Thiry, J.-J. Pireaux, and R. Caudano. *Phys. Rev. B*, 33:5682, 1986.

[73] R.E. Palmer and P. J. Rous. Resonances in electron scattering by molecules on surfaces. *Rev. Mod. Phys.*, 64(2):383, 1992.

[74] C. Mazzara. *Hydroxylation par adsorption dissociative de l'eau, des surfaces de silicium,silice et silice modifiée par le sodium.* PhD thesis, Université Rennes 1, France, 1998.

[75] J. W. Gadzuk. Shape resonances, overtones, and electron energy loss spectroscopy of gas phase and physisorbed diatomic molecules. *J. Chem. Phys.*, 79(8):3982–3987, 1983.

[76] A. A. Lucas and M. Sunjić. Fast-electron spectroscopy of surface excitations. *Phys. Rev. Lett.*, 26:229–232, 1971.

[77] E. Evans and D. L. Mills. Theory of inelastic scattering of slow electrons by long-wavelength surface optical phonons. *Phys. Rev. B*, 5:4126–4139, 1972.

[78] E. Evans and D. L. Mills. Theory of inelastic scattering of slow electrons by long-wavelength surface of optical phonons: multiphonon processes. *Phys. Rev. B*, 7:853–868, 1973.

[79] D. L. Mills. The scattering of low energy electrons by electric field fluctuations near crystal surfaces. *Surf. Sci.*, 48:59–79, 1975.

[80] A. A. Lucas and J. P. Vigneron. Theory of electron energy loss spectroscopy from surfaces of anisotropic materials. *Solid. Stat. Comm.*, 49:327–330, 1984.

[81] Ph. Lambin, J. P. Vigneron, and A. A. Lucas. Electron-energy-loss spectroscopy of multilayered materials: theoretical aspects and study of interface optical phonons in semiconductor superlattices. *Phys; Rev. B*, 32(12):8203–8215, 1985.

[82] J. Geiger. Elektronen und festkörper. *Vieweg, Braunschweig*, 1968.

[83] Ph. Lambin, A. A. Lucas, and J. P. Vigneron. On the role of the image force in the electron energy loss spectrum of a dielectric target. *Surf. Sci.*, 182:567–575, 1987.

[84] W.L. Schaich. Calculation of EELS at a doped semiconductor surface. *Surf. Sci.*, 122(1):175 – 189, 1982.

[85] S. Y. Tong. Theory of low-energy electron diffraction. *Prog. Surf. Sci.*, 7(1):1–48, 1975.

[86] S. Y. Tong, C. H. Li, and D. L. Mills. Inelastic scattering of electrons from adsorbate vibrations: Large-angle deflections. *Phys. Rev. Lett.*, 44(6):407, 1980.

[87] C. H. Li, S. Y. Tong, and D. L. Mills. Large-angle inelastic electron scattering from adsorbate vibrations: Basic theory. *Phys. Rev. B*, 21(8):3057, 1980.

[88] S. Y. Tong, C. H. Li, and A. R. Lubinsky. Dynamical calculations of angle-resolved ultraviolet photoemission from c (2× 2) O and S on Ni(001). *Phys. Rev. Lett.*, 39(8):498, 1977.

[89] G. Rocker, J. A. Schaefer, and W. Göpel. Localized and delocalized vibrations on TiO_2(110) studied by high-resolution electron-energy-loss spectroscopy. *Phys. Rev. B*, 30:3704–3708, Oct 1984.

[90] P. A. Cox, R. G. Edgell, S. Eriksen, and W. R. Flavell. The high resolution electron energy loss spectrum of TiO_2(110). *J. Electron. Spec. and Rel. Phenom.*, 39:117–126, 1986.

[91] L.L. Kesmodel, J.A. Gates, and Y.W. Chung. Observation of surface optical phonons on TiO_2(100). *Phys. Rev. B*, 23:489–492, 1981.

[92] M. A. Henderson. An HREELS and TPD study of water on TiO_2(110): the extent of molecular versus dissociative adsorption. *Surf. Sci.*, 355:151–166, 1996.

[93] M. A. Henderson, W. S. Epling, C. L. Perkins, C. H. F. Peden, and U. Diebold. Interaction of molecular oxygen with the vacuum-annealed TiO_2(110) surface: molecular and dissociative channels. *J. Phys. Chem. B*, 103:5328–5337, 1999.

[94] M. A. Henderson, W. S. Epling, C. H. F. Peden, and C. L. Perkins. Insights into photoexcited electron scavenging processes on TiO_2 obtained from studies of the reaction of O_2 with oh groups adsorbed at electronic defects on TiO_2 (110). *J. Phys. Chem. B*, 107:534–545, 2003.

[95] M. A. Henderson, M. Shen, Z.-T. Wang, and I. Lyubinetsky. Characterization of the active surface species responsible for UV-induced desorption of O_2 from the rutile TiO_2 (110) surface. *J. Phys. Chem. C*, 117:5774–5784, 2013.

[96] H. Noei, L. Jin, H. Qiu, M. Xu, Y. Gao, J. Zhao, M. Kauer, C. Wöll, M. Muhler, and Y. Wang. Vibrational spectroscopic studies on pure and metal-covered metal oxide surfaces. *Phys. Status Solidi B*, 250:1204–1221, 2013.

[97] H. Qiu, B. Meyer, Y. Wang, and C. Wöll. Ionization energies of shallow donor states in ZnO created by reversible formation and depletion of h interstitials. *Phys. Rev. Lett.*, 101:236401, 2008.

[98] P. A. Cox, W. R. Flavell, A. A. Williams, and R. G. Egdell. Application of Fourier transform techniques to deconvolution of HREELS spectra. *Surf. Sci.*, 152-153:784–790, 1985.

[99] Y. Goldstein, A. Many, and I. Wagner. EELS studies of quantized accumulation layers on ZnO surfaces. *Surf. Sci.*, 98:599–612, 1980.

[100] A. Many, I. Wagner, A. Rosenthal, J. I. Gersten, and Y. Goldstein. Plasmas on quantized accumulation layers on ZnO surfaces. *Phys. Rev. Lett.*, 46:1648–1651, 1981.

[101] Y. Wang, B. Meyer, X. Yin, M. Kunat, D. Langenberg, F. Traeger, A. Birkner, and Ch. Wöll. Hydrogen induced metallicity on the ZnO $(10\overline{1}0)$ surface. *Phys. Rev. Lett.*, 95:266104, 2005.

[102] R. Matz and H. Lüth. Conduction-band surface and plasmons in the electron-energy-loss spectrum of GaAs(110). *Phys. Rev. Lett.*, 46:500–504, 1981.

[103] B. N. J. Persson and J. E. Demuth. Inelastic scattering of slow electrons from Si(111) surfaces. *Phys. Rev. B*, 30:5968–5986, 1984.

[104] J.A. Stroscio and W. Ho. Long-range quasielastic and scattering of low-energy electrons by conduction-band and surface plasmons and on Si(111)(7x7). *Phys. Rev. Lett.*, 54:1573–1577, 1985.

[105] J. A. Stroscio and W. Ho. Quasielastic electron scattering as a probe of the silicon surface space-charge region. *Phys. Rev. B*, 36:9736–9745, 1987.

[106] A. Ritz and Lüth. Experimental evidence and for surface and quenching and of the surface and plasmon on InSb(110). *Phys. Rev. Lett.*, 52:1242–1246, 1984.

[107] T. Inaoka and D. M. Newns. Theoretical analyses of EELS from an n-type InSb surface. *Surf. Sci.*, 186:290–308, 1987.

[108] Y. Chen, J. C. Hermanson, and G. J. Lapeyre. Coupled plasmon and phonon in the accumulation layer of InAs(110) cleaved surfaces. *Phys. Rev. B*, 39:12682–12687, 1989.

[109] M. Noguchi, K. Hirakawa, and T. Ikoma. In situ determination of electronic properties of clean GaAs(100) surfaces by high-resolution electron energy loss spectroscopy. *Surf. Sci.*, 271:260–276, 1992.

[110] V. M. Polaakov, A. Elbe, J. Wu, G. J. Lapeyre, and J. A. Schaefer. Silicon spreading in δ-doped GaAs(100) : a high-resolution electron-energy-loss-spectroscopy study. *Phys. Rev. B*, 54:2010–2018, 1996.

[111] F. Gervais and J. F. Baumard. LO-phonon plasmon coupling in non-stoichiometric rutile TiO_2. *Solid State Commun.*, 21:861–865, 1977.

[112] Ph. Lambin, L. Henrard, P. Thiry, C. Silien, and J. P. Vigneron. The dielectric theory of hreels, a short survey. *J. Electron Spectrosc. Relat. Phenom.*, 129(23):281–292, 2003. Proceedings of the WBW22 Workshop, dedicated to Prof. A.A. Lucas on his retirement.

[113] P.A. Thiry, M. Liehr, J.J. Pireaux, and R. Caudano. Infrared optical constants of insulators determined by high-resolution electron-energy-loss spectroscopy. *Phys. Rev. B*, 29:4824, 1984.

[114] D. Schöche, T. Hofmann, R. Korlacki, T.E. Tiwald, and M. Schubert. Infrared dielectric anisotropy and phonon modes of rutile TiO_2. *J. Appl. Phys.*, 113:164102, 2013.

[115] E. D. Palik. *Handbook of Optical Constants of Solids*, volume 1-3. Academic Press, 1985.

[116] C. Lee, P. Ghosez, and X. Gonze. Lattice dynamics and dielectric properties of incipient ferroelectric TiO_2 rutile. *Phys. Rev. B*, 50:13379–13387, 1994.

[117] F. Gervais and B. Piriou. Temperature dependence of transverse and longitudinal optic modes in TiO_2 (rutile). *Phys. Rev. B*, 10:1642–1654, 1974.

[118] F Gervais. Optical conductivity of oxides. *Materials Science And Engineering R-Reports*, 39:29–92, 2002.

[119] D. M. Eagles. Polar modes of lattice vibration and polaron coupling constants in rutile (TiO_2). *J. Phys. Chem. Solids*, 25:1243–1251, 1964.

[120] J. G. Traylor, H. G. Smith, R. M. Nicklow, and M. K. Wilkinson. Lattice dynamics of rutile. *Phys. Rev. B*, 3:3457–3472, 1971.

[121] P.D. Mitev, K. Hermansson, B. Montanari, and K. Refson. Soft modes in strained and unstrained rutile TiO_2. *Phys. Rev. B*, 81:134303, 2010.

[122] M. Dou and C. Persson. Comparative study of rutile and anatase SnO_2 and TiO_2: Band-edge structures, dielectric functions, and polaron effects. *J. Appl. Phys.*, 113:083703, 2013.

[123] R.J. Betsch, H.L Park, and W.B. White. Raman spectra of stoichiometric and defect rutile. *Mater. Res. Bull.*, 26:613–622, 1991.

[124] J. Pascual, J. Camassel, and H. Mathieu. Fine structure of the intrinsic absorption edge to TiO_2. *Phys. Rev. B*, 18:5606–1614, 1978.

[125] L. Chiodo, J. M. García-Lastra, A. Iacomino, S. Ossicini, J/ Zhao, H. Petek, and A. Rubio. Self-energy and excitonic effects in the electronic and optical properties of TiO_2 crystalline phases. *Phys. Rev. B*, 82:045207, 2010.

[126] J. Leng, J. Opsala, H. Chua, M. Senkoa, and D.E. Aspnes. Analytic representations of the dielectric functions of materials for device and structural modeling. *Thin Solid Films*, 313-314:132–136, 1998.

[127] A.B. Djurisic, Y. Chan, and E.H. Li. Progress in the room-temperature optical functions of semiconductors. *Materials Science And Engineering R-Reports*, 38:237–293, 2002.

[128] N. W. Aschcroft and N. D. Mermin. *Physique des solides*. EDP Sciences, 2002.

[129] G.A. Samara and P.S. Peercy. Pressure and temperature dependence of the static dielectric constants and Raman spectra of TiO_2 (rutile). *Phys. Rev. B*, 7:1131–1148, 1973.

[130] R.L. Kurtz, R. Stockbauer, T.E. Madey, E. Román, and J.L. de Segovia. Synchrotron radiation studies of H_2O adsorption on TiO_2. *Surf. Sci*, 218:178–200, 1989.

[131] W. S. Epling, C. H. F. Peden, M. A. Henderson, and U. Diebold. Evidence for oxygen adatoms on TiO_2(110) resulting from O_2 dissociation at vacancy sites. *Surf. Sci.*, 412-413:333–343, 1998.

[132] V.N. Bogomolov and D.N. Mirlin. Optical absorption by polarons in rutile TiO_2 single crystals. *Phys. Stat. Sol*, 27:443–453, 1968.

[133] V. M. Khomenko, K. Langer, H. Rager, and A. Fett. Electronic absorption by Ti^{3+} ions and electron delocalization in synthetic blue rutile. *Phys. Chem. Miner.*, 25(5):338–346, 1998.

[134] J.T. Devreese and A.S. Alexandrov. Fröhlich polaron and bipolaron: recent developments. *Reports on Progress in Physics*, 72:066501, 2009.

[135] A. S. Alexandrox and J.T. Devreese. *Advances in polaron physics*. Spinger, 2010.

[136] D. Emin. Optical properties of large and small polarons and bipolarons. *Phys. Rev. B*, 48:13691–13702, 1993.

[137] T He. Optical absorption of free small polarons at high temperatures. *Phys. Rev. B*, 51:16689–16694, 1995.

[138] E. Hendry, M. Koeberg, J. Pijpers, and M. Bonn. Reduction of carrier mobility in semiconductors caused by charge-charge interactions. *Phys. Rev. B*, 75:233202, 2007.

[139] F. Herklotz, E.V. Lavrov, and J. Weber. Infrared absorption of the hydrogen donor in rutile TiO_2. *Phys. Rev. B*, 83:235202, 2011.

[140] Ph. Lambin, J. P. Vigneron, and A. A Lucas. Computation of the surface electron-energy-loss spectrum and in specular geometry for an arbitrary plane-stratified medium. *Computer Physics Communications*, 60:351–364, 1990.

[141] J. D. Jackson. *Classical Electrodynamics*. Wiley & Sons, New York, 1975.

[142] T. Bak, J. Nowotny, M. Rekas, and C.C. Sorrell. Defect chemistry and semiconducting properties of titanium dioxide: I. Intrinsic electronic equilibrium. *J. Phys. Chem. Solids*, 64:1043–1056, 2003.

[143] J. I. Gersten. Theory of surface plasmarons. *Surf. Sci.*, 92:579–592, 1980.

[144] S. Takata, Y. Miura, and Y. Matsumoto. Evidence for the intrinsic nature of band-gap states electrochemically observed on atomically flat TiO_2(110) surfaces. *Phys. Chem. Chem. Phys.*, 16:24784–24789, 2014.

[145] P. Krüger, J Jupille, S Bourgeois, B Domenichini, A Verdini, L Floreano, and A Morgante. Intrinsic nature of the excess electron distribution at the TiO_2(110) surface. *Phys. Rev. Lett.*, 108:126803, 2012.

[146] M. A. Henderson. A surface perspective on self-diffusion in rutile TiO_2. *Surf. Sci.*, 419(2):174–187, 1999.

[147] S. Wendt, R. Bechstein, S. Porsgaard, E. Lira, J. . Hansen, P. Huo, Z. Li, B. Hammer, and F. Besenbacher. Comment on oxygen vacancy origin of the surface band-gap state of TiO_2(110). *Phys. Rev. Lett.*, 104, 2010.

[148] L.E. Hollander and P. L. Castro. Anisotropic conduction in nonstoichiometric rutile TiO_2. *Phys. Rev.*, 119:1882–1885, 1960.

[149] J. H. Becker and W. R. Hosler. Multiple-band conduction in n-type rutile TiO_2. *Phys. Rev.*, 137:A1872–A1877, 1965.

[150] C. Di Valentin, G. Pacchioni, and A. Selloni. Electronic structure of defect states in hydroxylated and reduced rutile TiO_2 (110) surfaces. *Phys. Rev. Lett.*, 97(16):166803, 2006.

[151] E. Finazzi, C. Di Valentin, and G. Pacchioni. Nature of Ti interstitials in reduced bulk anatase and rutile TiO_2. *J. Phys. Chem. C*, 113:3382–3385, 2009.

[152] N.A. Deskins, R. Rousseau, and M. Dupuis. Defining the role of excess electrons in the surface chemistry of TiO_2. *J. Phys. Chem. C*, 114:5891–5897, 2010.

[153] A. Janotti, J. B; Varley, P. Rinke, N. Umezawa, G. Kresse, and C. G. Van de Walle. Hybrid functional studies of the oxygen vacancy in TiO_2. *Phys. Rev. B*, 81:085212, 2010.

[154] P. Deák, B Aradi, and T/ Frauenheim. Polaronic effects in TiO_2 calculated by the HSE06 hybrid functional: dopant passivation by carrier self-trapping. *Phys. Rev. B*, 83:155207, 2011.

[155] Peter Deák, Bálint Aradi, and Thomas Frauenheim. Quantitative theory of the oxygen vacancy and carrier self-trapping in bulk TiO_2. *Phys. Rev. B*, 86(19):195206, Nov 2012.

[156] C. Spreafico and J. VandeVondele. The nature of excess electrons in anatase and rutile from hybrid DFT and RPA. *Phys. Chem. Chem. Phys.*, 16:26144–26152, 2014.

[157] L. D. Landau. Über die bewegung der elektronen in kristalgitte. *Phys. Z. Sowjetunion*, 3:644–645, 1933.

[158] T. Holstein. Studies of polaron motion: Part II. the small polaron. *Annal of Physics*, 8:343–389, 1959.

[159] H. Fröhlich. Electrons in lattice fields. *Advances in Physics*, 3:325–361, 1954.

[160] C. Noguera. *Physics and Chemistry at Oxide Surfaces*. Cambridge University Press, Cambridge, 1995.

[161] G. A. Acket and J. Volger. On the electron mobility and the donor centres in reduced and Li doped rutile TiO_2. *Physica*, 32:1680–1692, 1966.

[162] T. Bak, J. Nowotny, and M. K. Nowotny. Defect disorder and of titanium and dioxide. *J. Phys. Chem. B*, 110:21560–21567, 2006.

[163] H. Mathieu. *Physique des semiconducteurs et des composants lectroniques*. Masson, 1990.

[164] A. K. See, M. Thayer, and R. A. Bartynski. Angle-resolved inverse-photoemission study of the nearly perfect tio_2(110) surface. *Phys. Rev. B*, 47:13722–13729, May 1993.

[165] L. Friedman. Hall effect in the polaron-band regime. *Phys. Rev. B.*, 131:2445–2456, 1963.

[166] Z. Zhang and J. T. Yates. Band bending in semiconductors: chemical and physical consequences at surfaces and interfaces. *Chem. Rev.*, 112(10):5520–5551, Oct 2012.

[167] T. Okazawa, M. Kohyama, and Y. Kido. Electronic properties of au nano-particles supported on stoichiometric and reduced TiO_2(110) substrates. *Surf. Sci.*, 600:4430–4437, 2006.

[168] S. Moser, L. Moreschini, J. Jaćimović, O. S. Barišić, H. Berger, A. Magrez, Y. J. Chang, K. S. Kim, A. Bostwick, E. Rotenberg, L. Forró, and M. Grioni. Tunable polaronic conduction in anatase TiO_2. *Phys. Rev. Lett.*, 110:196403, 2013.

[169] X. Hao, Z. Wang, M. Schmid, U. Diebold, and C. Franchini. Coexistence of trapped and free excess electrons in $SrTiO_3$. *Phys. Rev. B*, 91:085204, 2015.